# Photophysics and Photochemistry of Conjugated Polymer Nanoparticles

Scott N. Clafton

*A thesis submitted in total fulfilment of the requirements for the degree of Doctor of Philosophy*


November, 2014

Department of Chemistry
School of Chemistry and Physics
The University of Adelaide

# Declaration

This work contains no material which has been accepted for the award of any other degree or diploma in any university or other tertiary institution and, to the best of my knowledge and belief contains no material previously published or written by another person, except where due reference has been made in the text.

I give consent to this copy of my thesis when deposited in the University Library, being made available for loan and photocopying, subject to the provisions of the Copyright Act 1968.

The author acknowledges that copyright of published works within this thesis (as listed below) resides with the copyright holder(s) of these works.

I also give permission for the digital version of my thesis to be made available on the web, via the University's digital research repository, the Library catalogue, the Australian Digital Theses Program (ADTP) and also through search engines, unless permission has been granted by the University to restrict access for a period of time.

_____

Scott N. Clafton

# Abstract

Nanoparticles prepared by the reprecipitation of conjugated polymers are an exciting development in the field of biological imaging and fluorescence sensing. The colloidal stability of these hydrophobic polymers in aqueous suspension was found to originate from the surface charge density of ~15 mC/m$^2$, which is in part attributed to negatively charged functional groups produced by polymer oxidation.

The suitability of these nanoparticles in traditional conjugated polymer applications, such as polymer photovoltaics, was also investigated using femtosecond fluorescence upconversion and transient absorption spectroscopies. Polarisation resolved studies of energy transfer in highly compact nanoparticles and extended polymer conformations showed the nanoparticles exclusively undergo intermolecular energy transfer. These observations were supported by energy transfer simulations on polymer structures obtained from coarse-grained molecular dynamics simulations.

Next, the recombination of polarons in composite rr-P3HT/PCBM nanoparticles, dominated by geminate recombination below 10 wt% PCBM, was demonstrated using a one dimensional diffusion model. This model also yielded the P3HT domain size of ~5 nm, which confirms these nanoparticles can serve as a model system for probing charge generation and recombination processes in device-like environments.

Finally, the power dependent exciton decay in highly ordered nanowires yielded an exciton diffusion length of 11 ± 3 nm, which is toward the upper limit of diffusion lengths reported for annealed P3HT films. This data indicates the gentle solution based crystallisation of nanowires is a promising route for enhancing the performance of bulk heterojunction devices.

# Acknowledgements

I would firstly like to extend my sincere gratitude to my supervisor Dr Tak Kee for allowing me to undertake my PhD studies in his group. His guidance, expertise and persistence have been crucial to my development. Although, in retrospect I wish I had followed some of his advice immediately and with greater enthusiasm to make this an even greater educational experience.

Dr David Beattie, my secondary supervisor, and his group at the Ian Wark Institute of the University of South Australia were extremely valuable, especially during the early studies of these nanoparticles. In particular, Dr Agnieszka Mierczynska-Vasilev and Dr Robert Acres for the AFM and XPS work, respectively.

Dr David Huang has been a great help with modelling and computational studies relating to this work. Thanks must also go to the members of his group, Ming Chiu, Kyra Schwarz and Patrick Tapping for their collective work on modelling exciton migration in MEH-PPV.

My fellow labmates past and present, Alex Gentleman, Mandy Leung, Taka Harada *et al.*, are all fantastic scientists and regardless of whether research is part of my future I look forward to learning more from you guys.

I am hugely thankful for the opportunity to visit the research group of Professor David Vanden Bout at the University of Texas at Austin supported by the D R Stranks Travelling Fellowship and the Research Abroad Scholarship. It was an incredible experience and I wholeheartedly encourage any graduate students reading this thesis to strongly consider undertaking research in an overseas laboratory. Also, it was here I learnt the value of having a postdoc like Dr Zhongjian Hu in the lab, who was able teach me so much in such a short period of time.

Finally and most importantly, I would like to thank my parents, Steve and Christine, my brother Andrew and my wonderful fiancée Rebecca for their encouragement and support throughout this ordeal. Your patience and understanding, especially during the final months of my studies, will not be forgotten.

# List of Publications

Publications based on work presented in this thesis:

**Chemical Defects in the Highly Fluorescent Conjugated Polymer Dots**

Scott N. Clafton, David A. Beattie, Agnieszka Mierczynska-Vasilev, Robert G. Acres, Alan C. Morgan and Tak W. Kee, *Langmuir* **2010**, *26*, 17785-17789.

**Femtosecond Dynamics of Excitons and Hole-Polarons in Composite P3HT/PCBM Nanoparticles**

Scott N. Clafton, David M. Huang, William R. Massey and Tak W. Kee, *Journal of Physical Chemistry B* **2013**, *117*, 4626-4633

**Femtosecond Fluorescence Upconversion and Molecular Dynamics Simulations of Energy Transfer in MEH-PPV Nanoparticles**

Scott N. Clafton, Patrick Tapping, Ming Chiu, Kyra Schwarz, David M. Huang, and Tak W. Kee, *In Preparation*

Other publications:

**Aggregation and Host-Guest Interactions in Dansyl Substituted Poly(acrylate)s in the Presence of β-Cyclodextrin and a β-Cyclodextrin Dimer in Aqueous Solution: A UV-Visible, Fluorescence, 1H NMR and Rheological Study**

Jie Wang, Duc-Truc Pham, Tak W. Kee, Scott N. Clafton, Xuhong Guo*, Philip Clements, Stephen F. Lincoln*, Robert K. Prud'homme, and Christopher J. Easton, *Macromolecules* **2011**, *44*, 9782–9791.

# Table of Contents

# Abbreviations

| | |
|---|---|
| BBO | β-barium borate |
| BEH-PPV | poly[2,5-(2′-ethylhexyloxy)]-1,4-phenylenevinylene |
| CCD | Charge-coupled Device |
| DLS | Dynamic Light Scattering |
| EET | Excitation Energy Transfer |
| FT-IR | Fourier Transform Infrared |
| GVD | Group Velocity Dispersion |
| LEGS | Local Exciton Ground State |
| MEH-PPV | poly[2-methoxy-5-(2-ethylhexyloxy)-1,4-phenylene vinylene] |
| P3HT | poly(3-hexylthiophene-2,5-diyl) |
| PCBM | phenyl-$C_{61}$-butyric acid methyl ester |
| PDHF | poly(9,9-dihexylfluoreneyl-2,7-diyl) |
| PDOF | poly(9,9-dioctylfluoreneyl-2,7-diyl) |
| PFBT | poly[(9,9-dioctylfluorenyl-2,7-diyl)-co-(1,4-benzo-(2,1’,3)-thiadiazole)] |
| PFPV | poly[{9,9-dioctyl-2,7-divinylenefluorenylene}-*alt*-*co*-{2-metoxy-5-(2-ethylhexyloxy)-1,4-phenylene}] |
| PLED | Polymer Light Emitting Diode |
| PMANa | poly(sodium methacrylate) |
| PPE | poly(2,5-di(3',7'-dimethyloctyl)phenylene-1,4-ethynylene) |
| PPV | poly(phenylene vinylene) |
| PSBTBT | poly[(4,4'-bis(2-ethylhexyl)dithieno[3,2-b:2',3'-dsilole)-2,6-diyl-*alt*-(2,1,3-benzothiadiazole)-4,7-diyl] |
| PSS | poly(styrene sulphonate) |
| PTFE | polytetrafluoroethylene |
| rr | regioregular |
| rra | regiorandom |
| TFP | Thin Film Polarisor |
| THF | tetrahydrofuran |
| TOPAS | Travelling-Wave Optical Parametric Amplifier of Superfluorescence |
| VRS | Vibrationally Relaxed State |
| WLG | White Light Generation |

# List of Figures

# List of Tables

# 1 Introduction

## 1.1 Conjugated Polymers

The discovery and development of conjugated polymers by Shirakawa, MacDiarmid and Heeger [1,2] for which they were awarded the Nobel Prize in Chemistry, have resulted in a new generation of photovoltaic and electroluminescent devices. These materials, often called 'conductive polymers', are suited to such applications as the alternating single and double bond structures offer both optical activity and electrical conductivity. Since the initial discovery of polyacetylene, many new classes of conjugated polymers have been synthesised for optimal performance in their intended application. Early examples of polymer photovoltaics [3] and polymer light emitting diodes (PLEDs) [4] were reported in the 1990s using poly *para*-phenylene vinylene (PPV) polymers. More recently, polythiophenes and polyfluorenes have become popular alternatives due to their superior performance. The general chemical structures of these well-known polymer classes are shown in Figure 1.1.

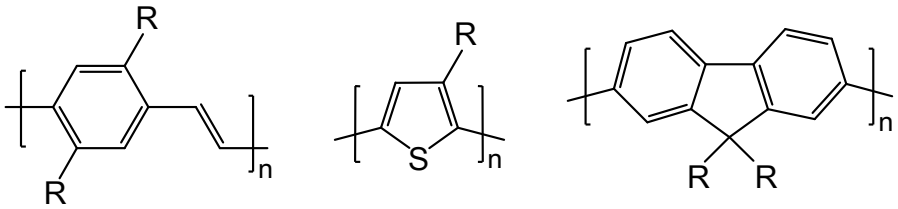


**Figure 1.1:** General chemical structures of PPV (left), polythiophene (centre) and polyfluorene (right)

The impressive optical and electronic properties of conjugated polymers are a result of the conjugated π–system. The π–electrons are not delocalised along the entirety of the polymer backbone, but rather are divided into many relatively small segments called 'chromophores' by conjugation defects, each containing several monomer units [5,6]. The nature of these defects is specific to the class of polymer. Worm-like polymers, such as polythiophenes, contain torsional defects where the dihedral angle between adjacent monomers cause gradual deviation from planarity over several monomer units [7]. Conversely, PPVs contain tetrahedral chemical defects from incomplete synthetic steps resulting in rigid segments punctuated by kinks allowed by the high flexibility of consecutive saturated carbon bonds [5,8]. Regardless of the polymer, these defects are randomly positioned throughout the polymer producing a distribution of chromophore lengths, and therefore energies. This distribution of chromophore lengths, is highly sensitive to the chemical environment of the polymer [9]. Therefore, the selection of side chain becomes important as it has the ability to alter the solubility of the polymer and the extent of inter/intra-chain interactions [10,11]. Such properties are crucial for the performance of conjugated polymer based devices [12]. Furthermore, the nature of the heteroatom present in some classes of conjugated polymers allows for subtle manipulation of the electronic properties for the desired application [13,14]. For example, substituting the sulphur atom of a regioregular polythiophene with selenium

reduces the band-gap by around 0.3 eV, increasing the light harvesting capability of these polymers in polymer photovoltaic cells [15].

## 1.2 Optical Processes

The absorption of light with appropriate energy by a chromophore promotes an electron from the highest occupied molecular orbital (HOMO) to the lowest unoccupied molecular orbital (LUMO) producing a molecular excited state, called an exciton. The exciton includes both the excited electron and the positively charged hole that remains in the state occupied by the electron before excitation. The oppositely charged electron and hole are bound by their electrostatic attraction with a typical binding energy (i.e. the difference in energy between the bound electron-hole pair and the separated charges) on the order of 0.1 eV in organic semiconductors. In conjugated polymers this $\pi$-$\pi^*$ transition is often referred to as the band-gap as the distribution of chromophore energies creates electronic band structures, where the HOMO and LUMO correspond to the valence and conduction bands, respectively. This absorption step ($A$) and the processes that follow are shown in Figure 1.2.

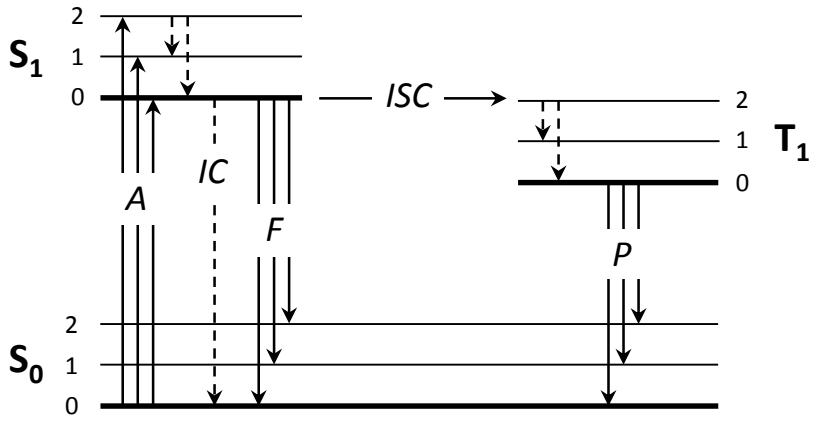


**Figure 1.2:** Jablonski diagram illustrating fundamental photophysical processes. The three lowest vibrational levels (0, 1 and 2) of each electronic state are also shown.

Depending on the energy of the photon being absorbed it is possible to promote the electron to a higher excited state. Generally, electrons in this higher excited state relax very rapidly and non-radiatively back to the first excited state ($S_1$) by internal conversion. Here it is assumed the ground state of the molecule is a singlet state where there is no net spin, which is often the case. Alternatively, the first excited state may also be populated directly by absorption of lower energy photons. These vibronic transitions originate from thermally populated vibrational levels of the ground electronic state and promote electrons to various vibrational levels of the first excited state. The intensities of these vibronic transitions depend on the Franck-Condon overlap and the Born-Oppenheimer approximation. The Born-Oppenheimer approximation assumes that due to the substantially smaller mass of an electron relative to the nuclei of the molecule, electronic transitions occur instantaneously with respect to the position of the nuclei. As a result, the electronic transitions and vibrational motions of a molecule are treated separately; an effect that can also be extended to rotational and translational motions due to their increasing timescales. In other words, for a vibronic transition to occur the Born-Oppenheimer approximation requires the nuclear geometry of the final

state must be unchanged from the initial state. Therefore, the transitions are limited to those involving vibrational states in the upper electronic state that can access the same molecular geometry as the lower state. The probability of a transition also depends on the overlap of the wavefunctions for each vibrational state, which describe the probability of finding the molecule in any given geometry. These wavefunctions are generally at a maximum at the extremes of vibrational motions as molecules will occupy these geometries for longer periods of time and are therefore more likely to exist when light is incident on the molecule. These considerations that describe the intensity of vibronic transitions yield the Franck-Condon principle.

Within $S_1$ electrons typically undergo vibrational relaxation to the lowest vibrational level. From this lowest vibrational level there are several relaxation pathways through which the electron can return to the ground electronic state ($S_0$) including internal conversion ($IC$), fluorescence ($F$) and intersystem crossing ($ISC$). There may be other non-radiative decay pathways, such as solvent quenching or exciton annihilation, depending on the nature of the sample and excitation conditions. All these relaxation processes that originate from the lowest vibrational level of $S_1$ are in competition with each other. The rates for each process will determine the proportion of molecules that relax by that pathway, which is conveniently expressed by the quantum yield. The quantum yield of fluorescence ($\phi_F$) is particularly important for energy transfer. It is expressed as

$$\phi_F = \frac{k_F}{\sum_i k_i} \tag{1.1}$$

where $k_F$ is the rate of fluorescence and $k_i$ is the rate of each relaxation process that originates from $S_1$. The rate of fluorescence decay and the fluorescence quantum yield

are important factors for the efficiency of energy transfer. In the case of intersystem crossing the electron transitions to an excited triplet state, in which there are two unpaired electrons with a non-zero total spin, may then undergo phosphorescence ($P$) to return directly to $S_0$. Alternatively, another intersystem crossing step will return the electron to higher vibrational levels of $S_0$, where it can relax by internal conversion. Both fluorescent and phosphorescent transitions originate from the lowest vibrational level of their respective electronic states and return to any of the vibrational levels of $S_0$ with sufficient Franck-Condon overlap, resulting in emission spectra with vibronic structure.

## 1.3 Energy and Charge Transfer

Further to these fundamental photophysical processes, excitation energy transfer (EET) is another important non-radiative process that occurs in conjugated polymers. It involves the transfer of energy from an excited state donor chromophore to a ground state acceptor chromophore of comparable energy, resulting in deactivation of the donor and excitation of the acceptor. The donor transfers energy to the acceptor from the ground vibrational state of $S_1$, or 'vibrationally relaxed state' (VRS), in accordance with the Born-Oppenheimer approximation and the conservation of energy. This event produces an acceptor in an excited vibrational state, called the local exciton ground state (LEGS), which undergoes rapid vibrational relaxation to the lowest vibrational level generating a new VRS that can serve as the donor for any subsequent energy transfer steps. The relaxation from LEGS to VRS is accompanied by localisation of the

exciton; this process is shown in Figure 1.3. There is no reabsorption of radiative emission or transfer of charge as this process is purely a transfer of energy.

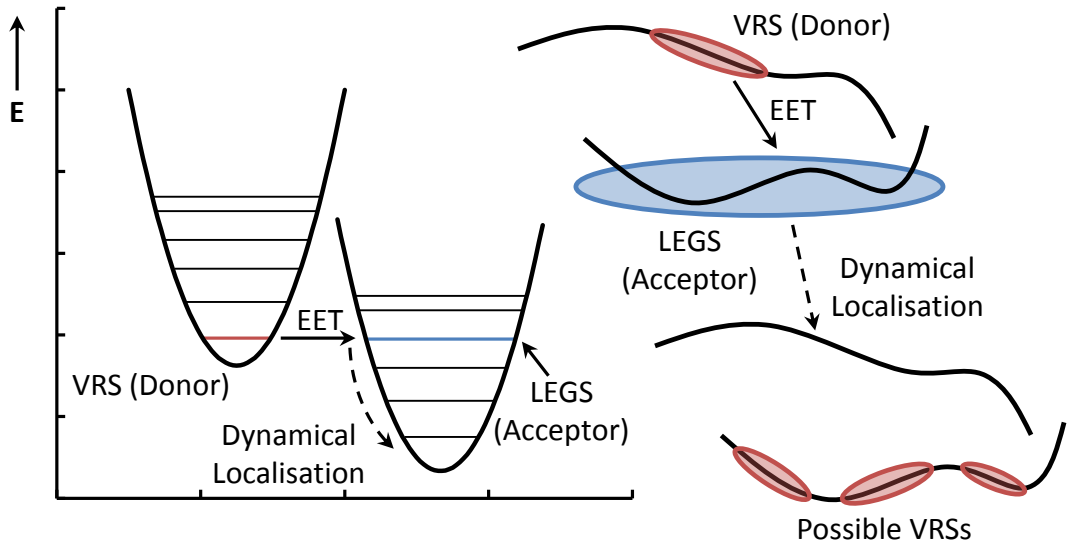


**Figure 1.3:** Energy transfer from the VRS to a LEGS followed by dynamic localisation to form a new VRS. Adapted from Ref [16].

In many applications of EET the donor and acceptor chromophores are chemically different [17]. However, energy transfer also occurs between molecules of the same chemical species or, in the case of conjugated polymers, different chromophores of the same molecule, where it is termed homotransfer. EET encompasses both the Dexter and Förster mechanisms. Dexter energy transfer concerns short range (< 1 nm) energy transfer where the excited electron of the donor is transferred to the LUMO of the acceptor. Simultaneously, an electron from the HOMO of the acceptor is transferred to the HOMO of the donor to complete the exchange, as shown in Figure 1.4. In this process there is no net transfer of charge. For electron exchange to occur there must be some overlap between the donor and acceptor wavefunctions, which decreases exponentially as the separation of donor and acceptor increases.

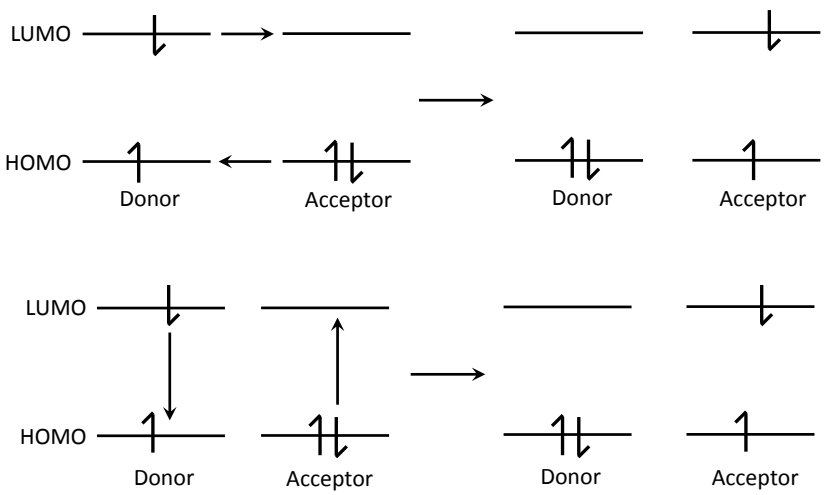


**Figure 1.4:** Dexter (top) and Förster (bottom) mechanisms of energy transfer.

Conversely, the range of Förster resonance energy transfer is much greater (~10 nm) because overlap of electronic wavefunctions is not necessary. Instead, the oscillating dipole of the donor induces an oscillation in the dipole of the acceptor. In this way, the energy transfer event causes relaxation of the donor and excitation of the acceptor, as shown in Figure 1.4. Unlike the Dexter energy transfer mechanism, this dipole-dipole interaction is subject to selection rules and therefore only occurs between pairs of singlet or triplet states. Förster energy transfer is the dominant mechanism of energy transfer for singlet excitons in conjugated polymers and is crucial to the performance of optoelectronic devices.

Several factors govern the rate of Förster energy transfer ($k_{ET}$) between donor and acceptor chromophores including the separation distance ($r$), their relative orientation ($\kappa$) and the spectral overlap between the normalised fluorescence of the donor ($F_D$) and the molar absorptivity of the acceptor ($\varepsilon_A$) as a function of wavelength ($\lambda$) according to

$$k_{ET} = \frac{\phi_D \kappa^2}{\tau_D r^6}\left(\frac{9000\ln(10)}{128\,\pi^5\,N\,n^4}\right)\int_0^\infty F_D(\lambda)\,\varepsilon_A(\lambda)\lambda^4 d\lambda. \qquad (1.2)$$

Here, $n$ is the refractive index of the medium, $N$ is Avogadro's number, and $\tau_D$ and $\phi_D$ are the fluorescence lifetime and fluorescence quantum yield of the donor in the absence of the acceptor, respectively [18]. Due to the strong dependence on the donor-acceptor distance, Forster energy transfer is limited to around 10 nm. The orientation factor ($\kappa$) depends on the angles, shown in Figure 1.5, made by donor ($\theta_D$) and acceptor ($\theta_A$) transition dipole with the line joining them, and the angle between the planes in which the donor and acceptor transition dipoles lie ($\phi$) according to

$$\kappa^2 = (\sin\theta_D \sin\theta_A \cos\phi - 2\ \cos\theta_D \cos\theta_A)^2. \qquad (1.3)$$

The maximum value of $\kappa$ is achieved when the donor and acceptor dipoles are collinear, while any donor-acceptor pair arranged orthogonally will produce the minimum value of zero. This equation describes the point-dipole approximation, which is acceptable when considering small molecules or chromophores; however, excitons in conjugated polymers can be delocalised over several nanometers. Therefore, it is necessary to employ the line-dipole approximation where the transition dipole moment is divided into sub-segments corresponding to each monomer unit of the chromophore [7,19].

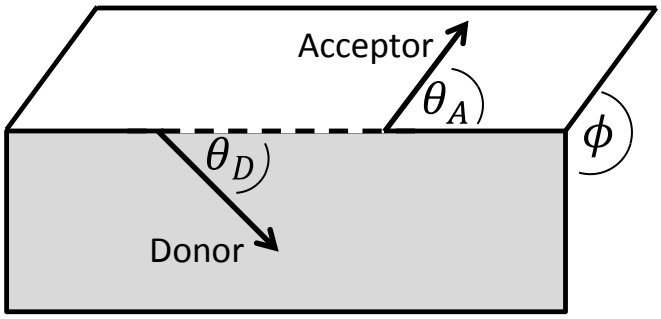


**Figure 1.5:** The angle of the donor ($\boldsymbol{\theta_D}$) and acceptor ($\boldsymbol{\theta_A}$) transition dipole moments with the line connecting them (dashed) and between the planes in which the dipole moments lie ($\boldsymbol{\phi}$). Adapted from Ref. [17].

Energy transfer is greatly enhanced by aggregation of the polymer; however, there are also important changes to the electronic structure of the polymer associated with aggregation that must be considered [20,21]. There are two extremes of aggregate behaviour, H-aggregates, produced through face-to-face stacking of chromophores, and J-aggregates, which are a result of end-to-end stacking of the chromophores, as shown in Figure 1.6. For the simplest case of an aggregate containing only two chromophores, splitting of the excited state occurs for both types, corresponding to the parallel and anti-parallel alignment of the dipole moments [22]. The parallel arrangement enhances the overall dipole moment and therefore strengthens the transition, while the transition for the anti-parallel case is significantly weaker. For multichromophoric aggregates, this results in the formation of electronic bands containing states corresponding to all the possible dipole alignment combinations [20]. These changes to the observed electronic transition energies result in blue and red shifts for H- and J-aggregates, respectively. However, there are other influences on the energy of these transitions, such as solvatochromism and changes in the distribution of chromophore lengths, which are more significant. Therefore, it is not advisable to rely on spectral shifts alone to assign the presence of H- or J-aggregates. In fact, aggregates of conjugated polymers do not

follow either description, but rather exhibit components of each [23]. Therefore, a more robust indicator of aggregate behaviour as proposed by Spano [24], using the ratio of transition intensities for the two lowest energy vibronic transitions, is necessary. For H-aggregates the ratio of these transitions ($A_{0-0}/A_{0-1}$) decreases upon aggregation due to the excitonic coupling between chromophores. Excitonic coupling induces a vibrational excitation in chromophores in close proximity to the vibronically excited chromophore, which is the vibronic analogy of a polaron, hence they are often referred to as excitonic polarons. As a result, coupling occurs between vibronically excited excitons in different upper vibrational states of the allowed aggregate transitions causing a redistribution of oscillator strength and the change in vibronic transition intensities. This relationship between the type of aggregate and relative transition intensities is used later in Chapter 6 to determine the degree of order in polymer nanostructures.

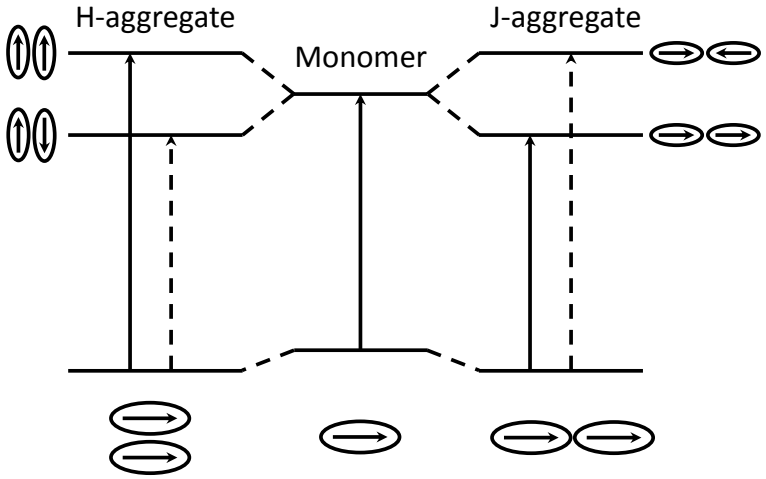


**Figure 1.6:** Electronic states of H-aggregates (left) and J-aggregates (right). Solid and dashed lines indicate allowed and forbidden transitions, respectively. The molecular alignments that consitute each aggregate type are also shown. Adapted from Ref [20].

Aggregation is also well-known to promote the photogeneration of localised charges on polymer segments called polarons [25-27]. A polaron is an unbalanced charge

localised on a polymer segment and the induced polarisation in the electron distribution of surrounding segments that contributes to the stabilisation of the charge. For some conjugated polymer structures interchanging double and single bonds of the conjugated backbone will result in an unchanged electronic structure; these are degenerate ground state polymers. The alternative, non-degenerate ground state polymers, have two distinct electronic structures of differing energy. The polyfluorenes, polythiophenes and PPVs used in this work are all examples of non-degenerate ground state polymers. The energy difference between the lower energy aromatic and higher energy quinoid ground state structures is necessary for the generation of polarons in these polymers. The chemical structures of these aromatic and quinoid forms of polythiophene are shown in Figure 1.7. Positive or 'hole' polarons form oxidatively, while negative polarons correspond to an excess electron. Photogeneration of either type of polaron creates two new electronic states within the optical band-gap. Of the newly available transitions involving these states only two ($P_1$ and $P_2$) are allowed by symmetry rules; these are shown for the hole-polaron in Figure 1.7.

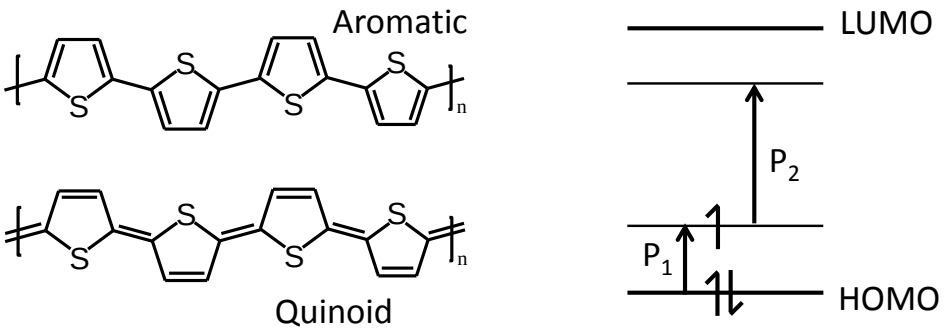


**Figure 1.7:** The chemical structures of the aromatic and quinoid forms of polythiophene (left) and the allowed optical transitions of a photogenerated hole-polaron (right).

As polarons can be produced by photoexcitations, they affect the excitonic properties of the polymer, most importantly, the fluorescence quantum yield through exciton-

charge annihilation [28,29]. The factors controlling the proportion of photoexcitations that generate polarons are not well understood; however, interchain interactions are thought to be crucial. This view is supported by several studies investigating the polaron formation in film and solution samples [30-32]. The relatively short separation between polymer chains in films allows polarons to delocalise over adjacent chains inhibiting their recombination. This is enhanced through addition of an electron accepting material. The greater electron affinity of the acceptor aids the separation of charges with the positive polaron remaining in the electron donor and the negative polaron being transferred to the acceptor. This phenomenon is the operating principle of organic photovoltaics and will be discussed further in the next section.

## 1.4 Polymer Photovoltaics

Polymer bulk heterojunction devices, first demonstrated by Heeger *et al.* [3], have been the subject of huge investment by academic and commercial institutions. These devices provide an alternative to existing silicon-based photovoltaic cells. Polymer photovoltaics utilise a combination of donor, with low electron affinity (p-type), and acceptor semiconductors with high electron affinity (n-type) to produce a *p-n* junction. Typically, conjugated polymers and substituted fullerenes are used as the donor and acceptor, respectively. The difference in electron affinity of these two materials produces an offset in the LUMO energy levels that drives charge transfer, shown in Figure 1.8. This offset must be greater than the binding energy of the exciton for dissociation to be an energetically favourable process.

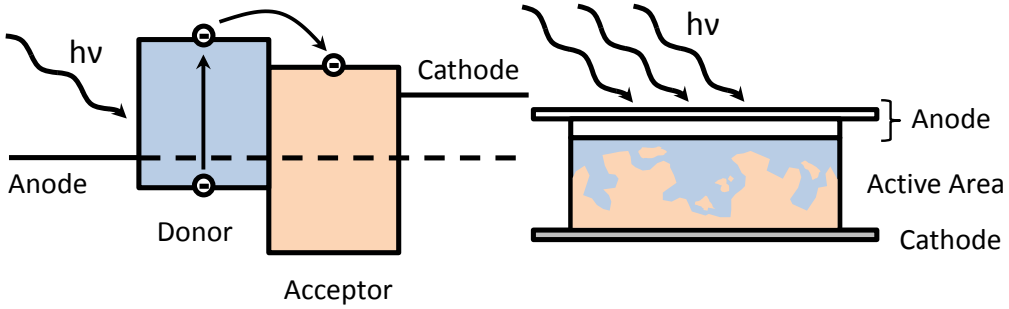


**Figure 1.8:** Energy level diagram (left) and architecture (right) of a bulk heterojuction organic photovoltaic device.

In a device, light is absorbed by the conjugated polymer generating an exciton that migrates through the conjugated polymer layer via energy transfer. As the exciton must reach the donor-acceptor interface to undergo charge separation, the range of exciton diffusion or migration is an important property of the donor material. This is quantified by the exciton diffusion length ($L_{ex}$), which is related to the diffusion coefficient ($D$) according to

$$L_{ex} = \sqrt{D\tau_r},$$

where the exciton lifetime exciton ($\tau_r$) is the time required for the exciton to regenerate the neutral ground state. This equation assumes the exciton diffusion occurs in only one dimension and is typically limited to tens of nanometres in conjugated polymers. Much longer diffusion lengths from 1 µm to 300 µm have reported for other photovoltaic technologies including perovskites [33] and traditional silicon [34]. Therefore, maximising this parameter in polymer photovoltaics is critical to their potential for widespread use. If the exciton reaches the electron acceptor interface a charge transfer state is formed where the electron resides in the acceptor layer and the hole remains in the conjugated polymer. At this point the two charges are still bound by coulombic attraction and may undergo geminate recombination. However, if they possess the

required energy, they can successfully separate into free charges and travel to the electrodes for charge collection. At any time within the active layer, separated charges may encounter an opposing charge with which to recombine. This is called bimolecular recombination. Both geminate and bimolecular recombination prevent charges from reaching the electrodes and are therefore undesirable loss pathways.

Nanostructure and device morphology have been identified as two areas that can mitigate the losses that result from geminate and bimolecular recombination and the short exciton diffusion lengths exhibited by conjugated polymers. Originally, organic photovoltaics were bilayer devices where the donor and acceptor are deposited individually, one on top of the other [35,36]. The thickness of the conjugated polymer layer in these devices must be comparable to the exciton diffusion length, as any excitons generated further from the interface will not undergo charge separation before relaxation occurs. Furthermore, such thin films are not capable of absorbing all the available solar radiation within the polymer absorption spectrum resulting in reduced overall efficiencies [37]. This limitation has been addressed through the use of bulk heterojunction device structures. The efficiency of a bulk heterojunction is less sensitive to the thickness of the polymer layer, allowing the thickness of these layers to exceed 100 nm and maximise light absorption [38]. The interpenetrating donor and acceptor layers of these devices are also favoured as it provides a much larger interfacial surface area than the bilayer design. Therefore, the average distance between excitation and the interface is much shorter in the bulk heterojunction, increasing the yield of free charges. Further improvements are afforded by thermal annealing of the blend films, which induces crystallisation and phase separation of the donor and acceptor materials [39].

Thermal annealing also permits the reorganisation of the polymer chains, which crystallise during cooling, dramatically increasing charge mobility [40]. Unfortunately, crystallisation of the polymer layer is hindered by the presence of the electron acceptor, preventing long range order [41,42]. This limitation has been addressed by preparing high aspect-ratio polythiophene nanowires prior to film casting. These nanowires are produced by a bottom-up, self-assembly process rather than more conventional top-down approaches, such as nanoimprint lithography [43]. The technique requires the dissolution of the polymer at elevated temperatures followed by gentle cooling, which induces crystallisation [44]. This self-assembly approach yields highly ordered polymer domains and allows great control over the device morphology. More details regarding the preparation of these nanowires can be found in the introduction of Chapter 6. So far, the efficiency of nanowire devices is slightly below thermally annealed blend films [45,46]. This discrepancy can potentially be addressed through improved orientation of the nanowires, which are typically parallel to the electrodes when cast in films [47].

Similarly, devices incorporating polymer nanoparticles have been prepared, albeit with very low efficiencies [48,49]. The maximum efficiency of 0.55% was reported by Andersen *et al.* [50], for nanoparticles of a low band-gap polymer PSBTBT. Typically, aqueous suspensions of these nanoparticles are produced by the mini-emulsion technique, which requires the combination of polymer solution in an organic solvent with a solution of surfactant molecules under agitation. The organic solvent is then removed by gentle heating while stirring continues to produce the ~50 nm diameter particles [51,52]. The poor performance is thought to stem from the disruption of charge transport between neighbouring particles caused by the presence of the surfactant layer [53,54]. So far, there has been little investigation into the use of polymer nanoparticles prepared by surfactant-free reprecipitation in photovoltaic

devices. One study by Darwis *et al.* [55], has shown this approach can achieve similar performance to devices containing nanoparticles prepared by mini-emulsion. The results of the nanoparticle studies presented in this thesis are also relevant to areas beyond these device studies, which are briefly reviewed in the following section.

## 1.5 Conjugated Polymer Nanoparticles

Preparation of conjugated polymer nanoparticles by reprecipitation was first reported by Wu *et al.* [56], with a vision of their development as fluorescence probes for biological imaging [57-62]. They offer high brightness in a surfactant-free particle with a smaller radius than most other varieties of fluorescent nanoparticles and greater photostability than CdSe quantum dots [63]. The photostability and fluorescence quantum yield of conjugated polymer nanoparticles are enhanced by encapsulation in a silica shell that also provides a handle for biofunctionalization [56]. Additionally, the conjugated polymers are thought to have very low cyto- and phototoxicity giving them an inherent advantage over many varieties of quantum dots when used in live biological systems [64]. The first example of live cell imaging using nanoparticles prepared using this method showed the successful uptake of the nanoparticles through endocytosis by macrophage cells [65]. Subsequent studies have extended the cellular imaging capabilities by employing single particle tracking for elucidating cellular mechanisms or biofunctionalization of the nanoparticle exterior for binding specificity [62,66]. Surface modification using biocompatible polymers, such as PSS and a combination of PSS with PMANa, further stabilised the nanoparticle suspension as indicated by the change in zeta-potential from –35 mV to –55 mV for the bare and PSS/PMANa coated nanoparticles, respectively. This study by Jin *et al.* [62], also functionalised PFBT

nanoparticles with streptavidin, which were successfully bound to the biotinylated antibodies on the surface of target MCF-7 breast cancer cells. Nanoparticles prepared from low band-gap conjugated polymers have been used to thermally ablate cancer cells [67]. Exciting the low band-gap polymer causes heating of the surrounding environment through vibrational relaxation, which is capable of destroying nearby colorectal cancer cells.

Early in their development, the potential of small molecule doped conjugated polymer nanoparticles for fluorescence based molecular sensing was realised. These sensors are typically prepared by adding the hydrophobic stimuli responsive small molecule to the precursor polymer solution. When this solution is rapidly exposed to a larger volume of water, the additive is encapsulated by the polymer as the interaction between the polymer and additive is preferable to its exposure to water. To date, fluorescence sensors for measuring pH [68], temperature [69], and the concentration of molecular oxygen [64] and metal ions [70,71] have been prepared. In particular, mercury ion sensors prepared by doping PFBT nanoparticles with rhodamine B spirolactam dyes boast a detection limit of 0.7 ppb, which are up to ten times more sensitive than other reported fluorescence-based mercury ion sensors in aqueous media [72]. The specificity arises from the reaction of the non-fluorescent rhodamine B spirolactam derivative with $Hg^{2+}$ ions producing another rhodamine B derivative that is highly fluorescent and has an absorption spectrum that overlaps well with the PFBT emission allowing FRET to occur efficiently. Furthermore, such high sensitivities are a result of amplified quenching, a process that exploits the energy transfer capability of conjugated polymers to funnel the excitation energy from several chromophores to a single small molecule quencher. In this way, the presence of few quenchers can dramatically attenuate the fluorescence from the sensor. Similarly, the specificities of

the other small molecule sensors mentioned previously are well-known. The molecular oxygen sensor described by Wu *et al.* [64], exploits the high intersystem crossing yield of platinum (II) centred octaethylporphyrin. Once the triplet state is formed it undergoes triplet-triplet annihilation with ground state $O_2$, which quenches the phosphorescence of the porphyrin. Temperature sensing was achieved using rhodamine B, which exhibits a linear relationship between the decrease in emission intensity and the increase in temperature when incorporated into PFBT nanoparticles. The pH sensor synthesised by Chan *et al.* [68], used another common fluorescent dye, fluorescein isothiocyanate, which shows pH dependent emission intensity. These dye molecules were covalently linked to the thiol– or amide–functionalised nanoparticles of the conjugated polymer PPE, which possesses strong spectral overlap with fluorescein. Additionally, as the emission of PPE, which is not strongly pH dependent, was used as an internal reference. These sensors are all ratiometric and sensitive across physiologically relevant ranges with excellent reversibility, which make them appropriate for *in vivo* studies; however, as mentioned earlier the additives must be adequately hydrophobic to be trapped within the polymer nanoparticle during preparation, which limits the range of possible analytes.

More recently, the viability of nanoparticle structures in conventional conjugated polymer applications has been investigated [73-79]. Enhancement of the fluorescence quantum yield in films of polyfluorene nanoparticles, to 0.68 from between 0.23 and 0.44 for films of varying thickness, demonstrated that these nanostructures may offer improved performance in polymer light emitting diodes [80]. The increase in fluorescence quantum yield was greatest for smaller nanoparticles with diameters shorter than 30 nm and was thought to be caused the reduction of interchain interactions that result from the isolation of single nanoparticles compared to bulk films. Conjugated

polymer nanoparticles have also been used to investigate the dependence of energy and charge transfer on polymer nanostructure in bulk heterojunction devices. They provide a convenient model system that exhibits bulk-like properties without the heterogeneity of films or devices [81-84]. Hu *et al.*, prepared nanoparticles of P3HT doped with PCBM to demonstrate the influence of PCBM concentration on the morphology within P3HT domains using single molecule spectroscopy [77,78]. These studies identified two distinct emitting states in these nanoparticles corresponding to π-stacked P3HT crystals with spacings of 3.8 Å and 4.5 Å, the relative abundance of which is dependent on the concentration of PCBM. Crystals with the shorter spacing are more prevalent at higher PCBM concentrations as the presence of the electron acceptor increases the tilt of the hexyl side chain preventing their interdigitation with those of neighbouring segments. Further studies showed the charge storage capability of capacitors containing these composite nanoparticles may be useful for photocontrolled memory devices and photoresponsive organic field effect transistors [85]. In such devices, the active elements can be as small as a single nanoparticle. Another example of this photoswitching effect was reported by Davis *et al.* [86], who demonstrated FRET-based fluorescence quenching of MEH-PPV nanoparticles by doping with a diarylethene derivative. This dopant undergoes photoinduced cyclisation when exposed to UV irradiation causing a change in the absorption spectrum that overlaps with the emission of the polymer and quenches the fluorescence; and effect that is reversed by irradiation with visible light.

## 1.6 Summary

Photophysical processes, including energy and charge transfer, of the conjugated polymers used in this work have been extensively studied since their photovoltaic capability was demonstrated over 20 years ago. More recent developments in polymer photovoltaics have focussed on the design of polymer nanostructure to overcome the limited exciton diffusion lengths. Therefore, it is necessary to consider the influence of polymer aggregation on these important processes for identification of optimal device structure and morphology. In this work, the viability of polymer nanoparticles and nanowires in these applications will be assessed through the probing of their physical and optical properties. Additionally, these results have implications for fluorescence imaging and sensing applications, which will also be considered.

# 2 Experimental Details

## 2.1 Materials

The conjugated polymers poly(9,9-dihexylfluoreneyl-2,7-diyl) (PDHF, MW = 103 kDa), poly(9,9-dioctylfluoreneyl-2,7-diyl) (PDOF, MW = 49 kDa), poly[{9,9-dioctyl-2,7-divinylenefluorenylene}-*alt-co*-{2-methoxy-5-(2-ethylhexyloxy)-1,4-phenylene}] (PFPV, MW = 111 kDa), and poly[2-methoxy-5-(2-ethylhexyloxy)-1,4-phenylene vinylene], (MEH-PPV, 680 kDa) were purchased from American Dye Source, Inc. Regioregular poly(3-hexylthiophene) (rr-P3HT, 94% regioregularity, 50 kDa) and regiorandom poly(3-hexylthiophene) (rra-P3HT, 15 kDa) were purchased from Rieke Metals Inc. and [6,6]-phenyl-$C_{61}$ butyric acid methyl ester (PCBM) was purchased from Nano C. Dichloromethane and methanol were purchased from Merck. These materials were used without further purification. Tetrahydrofuran (THF) was purchased from Ajax Finechem or Scharlau and distilled before use to remove butylated hydroxytoluene when necessary. Water used in all experiments was purified using a 10 MΩ Millipore MilliQ Reagent Water System fitted with a 0.45 μm filter.

## 2.2 Preparation of Nanoparticles and Nanowires

*Nanoparticles*

Aqueous suspensions of conjugated polymer nanoparticles were prepared using a well-known reprecipitation method [56]. The conjugated polymer was dissolved in THF at a typical concentration of 0.2 mg/mL overnight under nitrogen or with the aid of sonication and then diluted to a concentration of 20 ppm. This diluted polymer solution (2 mL) was added to water (8 mL) under vigorous stirring. Stirring continued for approximately one minute after mixing. Remaining THF was removed from the mixture under reduced pressure and the entirely aqueous suspension of conjugated polymer nanoparticles was filtered using a 0.7 μm glass fibre filter followed by a 0.2 μm PTFE filter that had been wetted with methanol. After filtering, any remaining methanol was evaporated under reduced pressure and the suspension was concentrated to a level appropriate for the desired experiment. Typically these samples had peak optical densities of 0.15 and 0.6 for steady-state and time-resolved optical spectroscopic measurements, respectively.

*Nanowires*

Nanowires were prepared from 1 mg/mL solutions of rr-P3HT in anisole following the previously reported whisker method [44,87]. The mixture was heated to ~80°C in a water bath and maintained at this temperature until the polymer had fully dissolved. The heat source was then removed and the solution was allowed to cool at a rate of approximately 20°C per hour. Portions of this nanowire suspension were then diluted by a factor of 15 yielding samples suitable for spectroscopic measurements. All samples were used within a week of preparation.

## 2.3 Optical and Physical Characterisation of Nanoparticles

*Atomic Force Microscopy (AFM)*

Atomic force microscopy images and size distributions as presented in Chapter 3 were collected in collaboration with Dr Agnieszka Mierczynska-Vasilev and Dr David Beattie at the Ian Wark Institute of the University of South Australia. Nanoparticle height measurements were performed on hydrated samples in a fluid cell with a Nanoscope III (Digital Instruments) atomic force microscope equipped with thin silicon nitride ($Si_3N_4$) cantilevers (V-shaped cantilever configuration) with a typical spring constant of 0.2 $Nm^{-1}$ and a resonance frequency of approximately 9 Hz. The cantilever and tip were cleaned with ethanol, rinsed with MilliQ water and dried under high purity nitrogen before use. Silicon wafer coated with titania (Philips Research Laboratories), used as the substrate, was cleaned in piranha solution followed by ultrapure water. The wafer was then immersed in a pH 4 solution, which provided a positively charged surface for adsorption of the negatively charged nanoparticles. A piezoelectric tube scanner capable of scanning 10×10 $\mu m^2$ in the plane of the substrate and 2.5 μm in height was used to translate the sample during scans.

A freshly cleaned substrate was attached to a magnetic stainless steel disk with conductive carbon tape. An O-ring was then placed on top of the substrate and the liquid cell was lowered onto the O-ring forming a seal. The nanoparticle sample was then injected into the liquid cell and allowed 15 minutes to deposit on the substrate before images were acquired. After collection, images for all samples were processed with the same second order flattening process, permitting direct comparison of samples.

*Dynamic Light Scattering (DLS) and Zeta Potential*

Dynamic light scattering particle size and zeta potential distributions were acquired using a ZetaSizer Nano S (Malvern Instruments). Size measurements were performed on dilute samples (~2 ppm), while zeta potential samples were 40 ppm with NaCl added to achieve a 1 mM concentration at pH 7. All measurements were taken at 25°C. The dependence of zeta potential on pH was investigated by altering the pH of the nanoparticle suspension with either dilute HCl or NaOH until the desired level was achieved as indicated by a pH meter.

*Fourier Transform Infrared Spectroscopy (FT-IR)*

Fourier transform infrared spectra were acquired using either a Perkin-Elmer Spectrum BX FT-IR system or a Nicolet Magna IR 750 spectrometer. Films of each sample were cast from 1 mg/mL solutions of either polymer or nanoparticles in dichloromethane directly onto a NaCl plate or ZnSe crystal, respectively.

*Steady-State Optical Spectroscopy*

Steady-state absorption spectra were collected using a Cary 300 Bio UV-vis (Varian) or a Cary 5000 UV-vis-NIR (Varian) spectrophotometer. Fluorescence spectra were collected using a Cary Eclipse fluorescence spectrophotometer where parameters, such as the excitation wavelengths, were optimised according to the spectral properties of the conjugated polymer being examined. Rhodamine 6G in water was used as the standard for fluorescence quantum yield measurements.

*X-ray Photoelectron Spectroscopy (XPS)*

Briefly, XPS is a surface sensitive technique for determining the chemical environments of a specific element in a sample. It requires an X-ray source of precisely

known energy to excite inner core electrons of an atom beyond the continuum limit producing photoelectrons. The kinetic energy ($KE$) of the ejected electrons is measured by the detector and is then used to calculate the binding energy ($BE$) of the electron by

$$KE = h\nu - BE - \phi, \qquad (2.1)$$

where $h\nu$ is the energy of the source and $\phi$ is the work function of the spectrometer. Different binding energies indicate the oxidation states of atoms. For organic samples, the oxidation state of carbon identifies what functional groups are present as atoms with reduced electron density exhibit higher binding energies.

Here, XPS experiments were performed in collaboration with Dr Robert Acres and Dr David Beattie at the Ian Wark Institute of the University of South Australia using a Kratos Axis Ultra DLD spectrometer with a 130 W monochromatic Al Kα (1486.6 eV) X-ray source and 700 × 300 μm$^2$ spot size. The sampling depth of this source is limited to a few nanometres. High resolution C 1s spectra were collected at pressures below 5x10$^{-9}$ Torr with a step size of 0.1 eV, a dwell time of 390 ms and averaged over three repeat scans per sample. For all samples, data were collected with the detector oriented normal to the surface of the substrate. Powdered polymer samples were mounted directly onto the sample holder with conductive copper tape. Aqueous nanoparticle dispersions were drop cast onto a freshly cleaned piece of silicon wafer, dried in a desiccator for several hours and then mounted onto the sample holder with conductive copper tape. Charge neutralisation was used during data acquisition; consequently samples showed no signs of degradation caused by exposure to the X-ray beam. To complement XPS results, concentrated nanoparticle samples were lyophilised, additionally dried in a 50°C oven and subjected to combustion analysis using a Carlo

Erba Elemental Analyser EA 1108 by the Campbell Microanalytical Laboratory at the University of Otago, New Zealand to determine the elemental composition.

## 2.4 Femtosecond Lasers for Time-Resolved Optical Spectroscopy

Lasers were first demonstrated in the 1960s and have since become indispensable research tools [88]. Of particular interest here are pulsed lasers that are used to study the kinetics of chemical changes on femtosecond timescales. The following section is an extended introduction to the processes required for operation of the pulsed lasers used in this work.

All lasers require a gain medium between a highly reflective mirror (high reflector) and another partially transmissive mirror (output coupler), which allows a small portion of the laser radiation to escape the cavity. The cavity length is defined by the distance between these two mirrors and will only support specific wavelengths with regular intervals. These wavelengths are the cavity modes of the laser and must coincide with the gain bandwidth to be amplified in the cavity. For most lasers the gain bandwidth is very narrow and therefore few modes are supported; however, some gain media possess large gain bandwidths and can therefore support thousands of modes. When multiple cavity modes are in phase and interfere with each other a train of light pulses is produced, as shown in Figure 2.1. To ensure all modes are in phase, either active or passive mode locking is used.

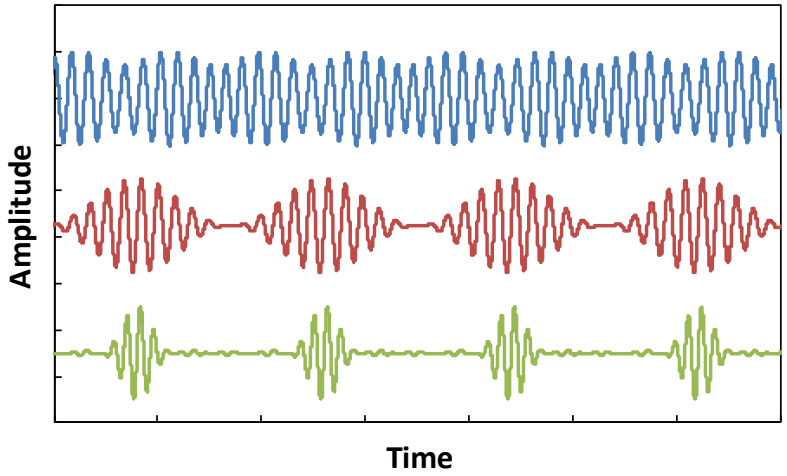


**Figure 2.1:** Pulses (or lack thereof) produced from interference of 3 modes out of phase (blue), 3 modes in phase (red) and 10 modes in phase (green).

Passive mode locking requires a saturable absorber within the laser cavity. As the name suggests this optical element absorbs light of low intensity and becomes transparent when exposed to higher intensities. In this way, lower intensity light, including the pulse edges, is absorbed and only the central most intense section of the pulse is transmitted. This approach is often preferred over active mode locking when generating femtosecond pulses, as it also reduces pulse duration. Passively mode locked systems depend on the nonlinear optical properties of the saturable absorber, which can have response times shorter than 300 fs.

Kerr lens mode locking, shown in Figure 2.2, is an alternative form of passive mode locking commonly used in Ti:sapphire lasers, which relies on the intensity dependent refractive index of a nonlinear medium. When the beam passes through this medium, the outer edge of the beam where the intensity is much lower experiences an almost unchanged refractive index, while the more intense centre portion of the beam is focussed by an increased refractive index. This change in refractive index ($\Delta n$) at a given intensity ($I$) is described by

$$\Delta n = n_2 I \tag{2.2}$$

where $n_2$ is the nonlinear refractive index [89]. Therefore, an aperture can be placed in the cavity after the nonlinear medium such that only the high intensity portion of the pulses are allowed to resonate in the cavity and any light of low intensity is lost. Similarly, the high peak power of pulses can be selected over the continuous wave operation of the laser, where the peak power is low. As the Kerr effect is a nonlinear optical process, the response of the nonlinear medium is much faster than a traditional saturable absorber, which allows the generation of even shorter pulses.

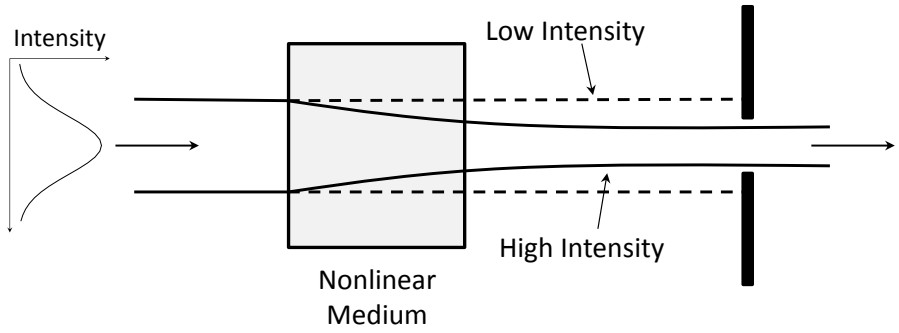


**Figure 2.2:** Focussing of a beam by the Kerr effect in Kerr lens mode locking arrangement. The initial intensity profile of the beam before entering the nonlinear medium is also shown.

Active mode locking requires an acousto-optic modulator (AOM), which contains a piece of quartz and a piezoelectric crystal. An oscillating voltage is applied to the piezoelectric crystal causing it to vibrate thereby inducing an acoustic wave in the quartz. This alters the refractive index of the quartz causing light to be diffracted and subsequently lost from the cavity. The frequency of the oscillating voltage is synchronised with the repetition rate of pulses to ensure they are retained in the cavity. Typically this frequency is calculated from the cavity length, which defines the repetition rate. A more precise alternative is to constantly measure the repetition rate and modify the frequency accordingly. This is called regenerative mode locking and is

the method used in these experiments. Unlike passive mode locking, active mode locking does not significantly shorten the pulse duration on femtosecond timescales. The speed of the acoustic wave moving through the quartz limits the AOM's response to several nanoseconds.

Once pulsing is established it is necessary to minimise the pulse duration. For this, the number of modes resonating in the cavity is important. Figure 2.1 shows that a greater number of modes will produce shorter pulses; in some cases these pulse durations are on the order of a few femtoseconds. Several types of lasers are capable of producing femtosecond pulses. Currently the most popular is the Ti:sapphire laser, which boasts the broadest tuning range of any femtosecond laser and very large gain bandwidths capable of producing pulses as short as 5.5 fs [90]. The gain bandwidth ($\Delta\lambda$) can be used to calculate the pulse duration ($\Delta t$) according to

$$\Delta t \geq 0.441 \frac{{\lambda_0}^2}{\Delta\lambda\, c} \tag{2.3}$$

where $c$ is the speed of light and $\lambda_0$ is the central wavelength of the laser transition. For ultrafast laser pulses both the temporal and spectral profile are Gaussian, therefore the time-bandwidth product is 0.441. This equality is reached when the shortest pulse duration is achieved; this is the transform-limited pulse duration.

Ideally, pulses should be very close to this limit as longer pulse durations indicate group velocity dispersion (GVD) or 'chirp'. This phenomenon is introduced by the wavelength-dependent refractive indices of optics in the laser cavity, including the Ti:sapphire rod itself, causing the velocity of different wavelength components to vary. Normal or positive GVD is the case where shorter wavelengths are delayed relative to longer wavelengths. Conversely, anomalous or negative GVD occurs when the shorter

wavelengths are advanced relative to the longer wavelengths. While it is essentially unavoidable, it can be negated by applying the opposing GVD to yield the transform-limited pulse. Occasionally, GVD is beneficial and introduced intentionally (e.g. amplification of ultrashort pulses).

Ultrashort pulses are desired for their high pulse energies. The typical output of a Ti:sapphire laser oscillator is ~1 W at a repetition rate of 80 MHz, therefore the pulse energy is on the order of nanojoules. While this pulse energy is quite low, it is sufficient for fluorescence upconversion experiments, as described in section 2.5. However, more demanding spectroscopies necessitate amplification of the oscillator output to generate millijoule pulse energies though such high pulse energies can damage optical components during amplification. To prevent this, the pulses are stretched to give a duration of hundreds or even thousands of picoseconds, amplified and then compressed to return the pulse duration to the femtosecond regime. Stretching and compression of pulses is achieved by introducing GVD using wavelength dispersive optics such as a pair of prisms or diffraction gratings, shown in Figure 2.3. Once the wavelength components of the pulse have been spatially separated they are directed through paths of varying lengths thereby extending or reducing the pulse duration.

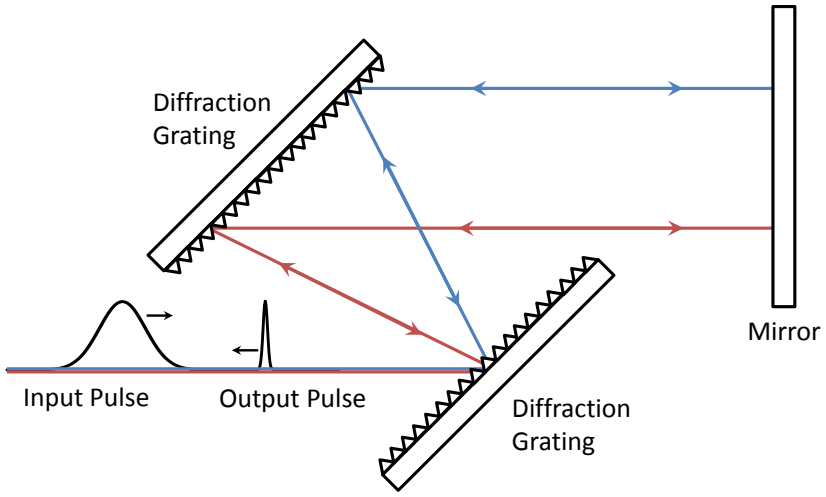


**Figure 2.3:** Introduction of negative GVD using two diffraction gratings. Typically negative GVD is introduced by the compressor. Adapted from Ref. [91].

One of the stretched seed pulses is selected for amplification by a Pockels cell and enters the regenerative amplifier cavity, shown in Figure 2.4. The particular seed pulse is selected because its arrival at the Ti:sapphire rod in the amplifier coincides with the pulse from the pump laser. The seed pulse is trapped in the cavity by a second Pockels cell as multiple passes through the rod are required for maximum amplification. The amplified pulses are then ejected from the cavity through a thin film polariser (TFP) and enter the compressor. The GVD introduced by the stretcher is reversed in the compressor using another diffraction grating by changing which wavelength components take the longer path. After passing through the compressor the pulse is returned close to the transform limit and maximum peak power.

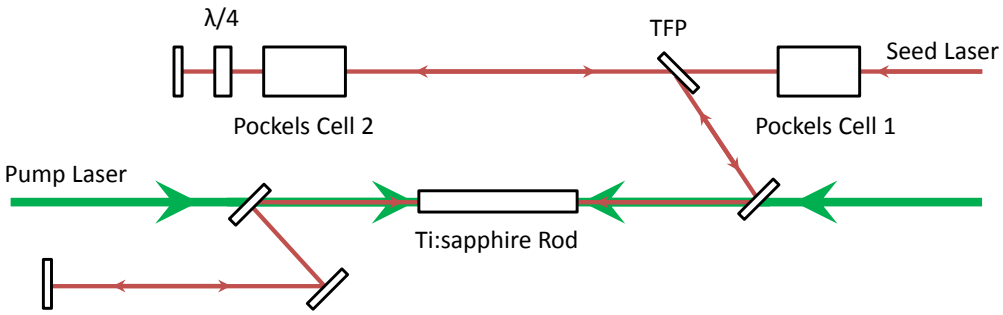


**Figure 2.4:** Regenerative amplifier cavity with pump (green) and seed (red) paths

Next, it is necessary to convert some of this amplified output to a visible wavelength suitable for excitation of the sample. Two popular methods for this are sum frequency generation and optical parametric amplification. Both methods are based on inherently inefficient nonlinear processes and therefore require the high peak power of amplified pulses to achieve any appreciable wavelength conversion.

Sum frequency generation produces a higher frequency photon ($\omega_3$) from two lower frequency photons ($\omega_1$ and $\omega_2$) in accordance with conservation of energy.

$$\omega_3 = \omega_1 + \omega_2 \tag{2.4}$$

When the two lower energy photons have the same frequency this is called second harmonic generation. To produce sum frequency photons a material with non-zero second order polarisation susceptibility ($\chi_2$) is required. The polarisation ($P$) in such a material induced by the electric field ($E$) of the incident light is described by

$$P = \epsilon_0(\chi_1 E + \chi_2 E^2 + \chi_3 E^3 + \cdots), \tag{2.5}$$

where $\epsilon_0$ is the electric permittivity and $\chi_n$ is the $n$-th order susceptibility tensor. Further to second order polarisability, the material must also be birefringent to allow the phase matching condition to be satisfied. The phase matching condition stems from conservation of momentum, where the incident vectors ($k_1$ and $k_2$) must be equal to the

sum frequency vector ($k_3$). This is conveniently expressed by the phase mismatch ($\Delta k$), which must be close to zero to allow significant sum frequency generation.

$$\Delta k = k_3 - k_2 - k_1 \tag{2.6}$$

Isotropic materials will always have a non-zero phase mismatch due to the frequency dependent refractive index. However, birefringent materials can produce a phase mismatch small enough for efficient sum frequency generation. This is possible because birefringent materials possess unique refractive indices for polarisations perpendicular and parallel to the crystal axis, often referred to as ordinary ($n_o$) and extraordinary ($n_e$), respectively.

Although there are various types of phase matching, only type I and type II in a negative uniaxial crystal, such as β-barium borate (BBO), are of interest here. For type I phase matching, the fundamental beams both have ordinary polarisation resulting in sum frequency light with extraordinary polarisation, while the two fundamental beams of the type II case have different polarisations. The sum frequency generated at different points throughout the crystal will only interact constructively when the refractive index of this sum frequency matches the refractive index of the fundamental beams. In practice, the phase matching condition is satisfied by rotating the optical axis of the crystal by $\theta_m$ relative to the polarisation of the incident light according to,

$$\frac{1}{n_e^2(\theta_m)} = \frac{\cos^2\theta_m}{n_o^2} + \frac{\sin^2\theta_m}{n_e^2}. \tag{2.7}$$

Only a limited range of wavelengths are available using sum frequency generation from a single laser source. Optical parametric amplification extends the range of accessible wavelengths from the ultraviolet to the infrared. This amplification occurs by mixing pump ($\omega_3$) and seed ($\omega_1$) beams in a nonlinear crystal. The seed depletes the pump in

favour of generating signal photons, which are of the same frequency as the seed. Idler photons ($\omega_2$) equal to the number of signal photons are also generated in this process to fulfil the conservation of energy. Like sum frequency generation, momentum is conserved using a BBO crystal set to the appropriate phase matching angle.

In our system, the amplifier output enters the optical parametric amplifier (Light Conversion, TOPAS-C) where it is divided into the main pump and preamplified pump beams using a beam splitter (BS). A small portion of the preamplified pump is then separated for white light generation (WLG) in a sapphire plate. The white light is used as the seed for the first amplification stage where it is noncollinearly combined with the preamplified pump in a type II BBO crystal generating the preamplified signal. A dispersive plate temporally separates the wavelength components of the white light prior to amplification. Therefore the desired wavelength from within the white light continuum is selected by altering the path length of the white light pulse relative to the preamplified pump pulse.

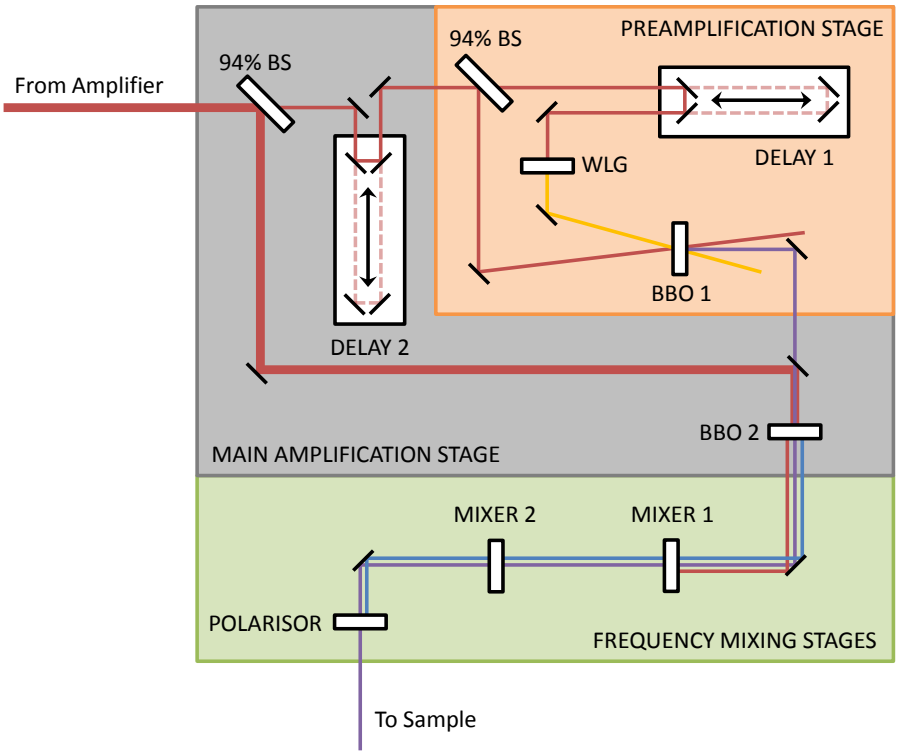


**Figure 2.5:** Optical layout of the TOPAS-C. The pump (red) and white light (yellow) are used to generate the signal (purple) and idler (blue).

The preamplified signal is then collinearly overlapped with the main pump in a type II BBO crystal generating the signal and idler with different polarisations. The timing of the main pump and the preamplified signal is optimised by delaying the entire preamplification stage relative to the main pump beam. Once the signal and idler are generated they enter the first of two mixing stages where the second harmonics of the signal or idler, and the sum frequencies of the signal or idler and the pump can be produced. These resulting wavelengths can then be frequency doubled in the second mixing stage to extend the range accessible wavelengths into the ultraviolet. Finally, the desired wavelength is isolated from the residual pump and other contaminants by polarised bandpass optics.

## 2.5 Fluorescence Upconversion

Fluorescence upconversion is an optically gated technique that offers one of the highest temporal resolutions for fluorescence spectroscopy. Other techniques such as time-correlated single photo counting are limited by the speed of processing electronics. Fluorescence upconversion relies on the sum frequency signal generated from the sample fluorescence and the gate pulse in a birefringent material with a non-zero second order polarisation susceptibility. The phase matching conditions required for sum frequency generation have been described in the previous section. The intensity of the sum frequency signal ($I_s$) at some delay time ($\tau$), is given by the convolution integral of the sample fluorescence ($I_f$) and the gate pulse ($I_g$) according to

$$I_s(\tau) = \int_{-\infty}^{+\infty} I_f(t)\, I_g(t-\tau) dt. \qquad (2.8)$$

By progressively delaying the arrival time of the gate pulse at the crystal, the fluorescence decay profile is constructed. In our experiment the delay is introduced by a retroreflector that travels along a motorised stage thereby lengthening the path of the gate pulse. Therefore the response of this detector can be relatively slow as the measured sum frequency intensity is defined by the position of the retroreflector.

Further to time-resolved data, fluorescence upconversion is routinely used to measure polarisation dependent processes. In such experiments, the sample is excited by linearly polarised light preferentially exciting molecules with a parallel transition dipole moment. After some delay, light can be emitted as fluorescence, which is also polarised but not necessarily parallel to the excitation. Any depolarisation is caused by rotational or torsional motions of the molecule in the excited state. Alternatively, it may

also occur if the absorption and emission dipole moments of the molecule are not parallel or as a result of energy transfer between molecules with different orientations. Monitoring the depolarisation allows direct measurement of the process that causes it.

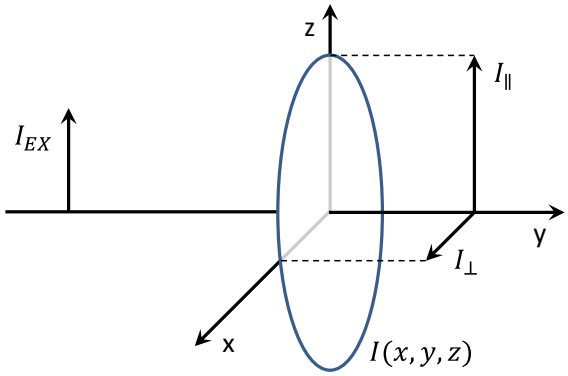


**Figure 2.6:** Anisotropic emission of a fluorophore oriented along the z-axis.

The overall polarisation of the sample is quantified by the emission anisotropy, which can be explained considering a single fluorophore aligned along the z-axis. The total fluorescent emission from the fluorophore is given by the sum of intensity components along three mutually orthogonal axes, as shown in Figure 2.6. For a molecule with a dipole moment oriented along the z-axis the intensity components $I_x$ and $I_y$ are equal. Therefore, these intensity components are described as either parallel ($I_{\parallel}$) or perpendicular ($I_{\perp}$) to the polarisation of excitation light ($I_{EX}$). The anisotropy ($r$) is then calculated by

$$r = \frac{I_{\parallel} - I_{\perp}}{I_{\parallel} + 2I_{\perp}}. \tag{2.9}$$

Alternatively, these parallel and perpendicular components can be expressed using polar coordinates. Figure 2.7 shows a single fluorophore with an emission dipole oriented at angles $\theta$ relative to the z-axis and $\phi$ relative to the x-axis. The projection of

this emission dipole moment on the z-axis and x-axis gives the parallel and perpendicular components, respectively.

$$I_{\parallel} \propto \cos^2\theta \tag{2.10}$$

$$I_{\perp} \propto \sin^2\theta \sin^2\phi = \frac{1}{2}\sin^2\theta \tag{2.11}$$

For a sample with an isotropic dipole distribution excited by light with polarisation parallel to the z-axis, the probability of excitation depends only on $\theta$. Therefore, the expression for the perpendicular intensity component is simplified by taking the average value of $\sin^2\phi$ given the sample is symmetrically distributed around the z-axis.

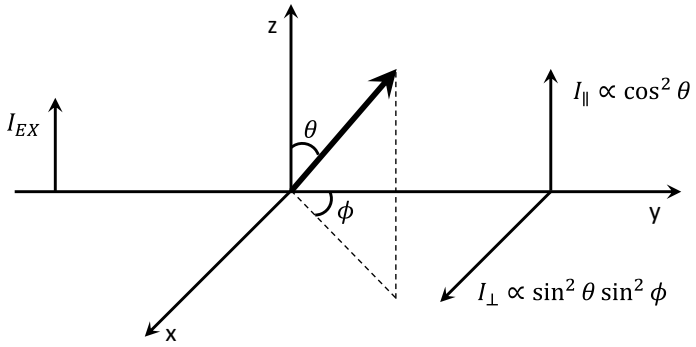


**Figure 2.7:** Polar coordinate representation of the emission anisotropy

The angular dependence of anisotropy is then derived from these polarisation components, Eq. (2.10) and (2.11), the trigonometric identity $\sin^2\theta + \cos^2\theta = 1$ and the anisotropy equation, Eq. (2.9). Additionally, the dependence of excitation on $\theta$ must be considered. This photoselection of fluorophores in an isotropic sample limits the maximum possible anisotropy value to 0.4, including this scaling factor yields the following equation

$$r = \frac{3\cos^2\theta - 1}{5}. \qquad (2.12)$$

This form of the equation shows the dependence of anisotropy on the average angular displacement between excitation and emission polarisations. According to this equation the anisotropy can take any value from 0.4 when the polarisation is unchanged, to -0.2 when the polarisation is rotated by 90°. While measuring the anisotropy can be informative, it is often necessary to measure the fluorescence decay free from any contributions from molecular motions or energy transfer. This is achieved in our experiments by setting the gate polarisation at 54.7° relative to the excitation polarisation, where the anisotropy is equal to zero. Under this condition the measured fluorescence intensity is proportional to the total intensity.

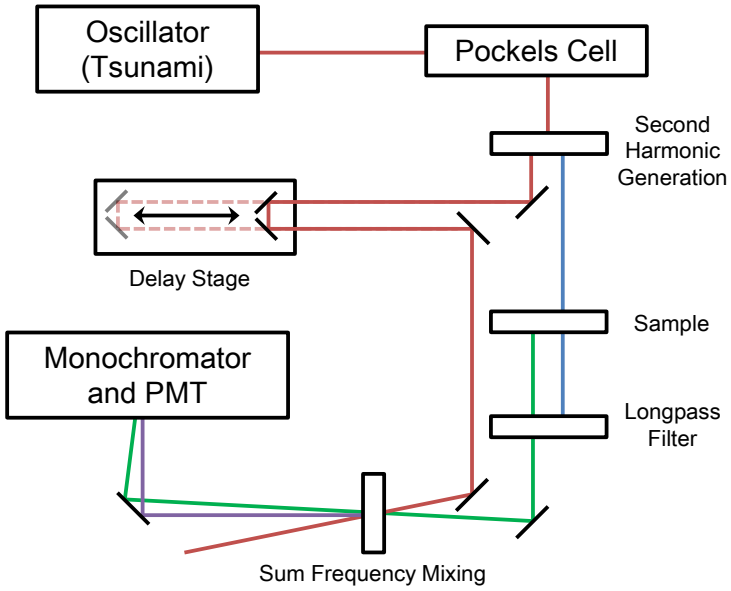


**Figure 2.8:** Diagram of fluorescence upconversion system. The gate, excitation and fluorescence beam paths are indicated by red, blue and green lines, respectively.

The key components of our fluorescence upconversion system are shown in Figure 2.8. Here, the laser source was a Ti:sapphire oscillator (Spectra Physics, Tsunami) that produced 100 fs pulses at 800 nm with a bandwidth of 14 nm. The initial 80 MHz

repetition rate was reduced to 40 MHz with a Pockels cell. The beam then passed through a 0.5 mm thick BBO crystal (Eksma Optics) to generate the second harmonic, which was then separated from the residual fundamental with a longpass filter producing the excitation and gate beams, respectively.

Both beams then entered the upconversion spectrometer (Ultrafast Systems, Halcyone) and passed through polarisers to ensure linearity. The polarisation of the excitation beam was then rotated with a half wave plate to achieve polarisations parallel, perpendicular and 54.7° relative to the gate depending on the experiment being performed. The excitation beam with pulse energy of 125 pJ was focussed onto the sample with a beam diameter of 230 μm producing fluorescence that was isolated from the excitation light with a longpass filter. Meanwhile, the gate beam was passed through the variable delay stage to provide time resolved data. The fluorescence emission and gate beams were focussed onto a type I BBO crystal to generate the sum frequency upconversion signal. Finally, the signal wavelength was selected using a double scanning monochromator, with a spectral bandwidth of 1 nm and collected with a photomultiplier tube.

## 2.6 Transient Absorption Spectroscopy

Transient absorption is another time-resolved spectroscopy technique routinely applied in order to study energy and charge transfer in conjugated polymers. While transient absorption requires more sophisticated instrumentation than fluorescence upconversion, it is capable of examining excited state species beyond the singlet

exciton. Furthermore, it can be applied to chemical systems that exhibit zero or low fluorescence intensities.

To better understand transient absorption, it is informative to first describe the basic principles of absorption spectroscopy. The absorbance ($A$) of a chemical species in solution is proportional to the molar absorptivity ($\varepsilon$), concentration ($c$), and path length ($l$) of the cell in which it is contained. In practice, absorbance is calculated from the ratio of light intensities in the presence ($I$) and absence ($I_0$) of the absorbing species; called the sample and reference intensities, respectively.

$$A = \varepsilon c l = -\log_{10}\left(\frac{I}{I_0}\right) \tag{2.13}$$

This is also the basis of transient absorption; a pump probe spectroscopy technique where the pump pulse promotes the sample to an excited state and the relatively low intensity probe measures the absorbance of the sample after some delay. The pump is modulated such that the arrival of every second probe pulse at the sample coincides with the arrival of a pump pulse. This allows measurement of the absorbance with the pump pulse ($A_{pump\ on}$) and the absorbance without the pump pulse ($A_{pump\ off}$), the difference of which is the transient absorption signal ($\Delta A$).

$$\Delta A = A_{pump\ on} - A_{pump\ off} \tag{2.14}$$

Use of a white light continuum probe, rather than a single wavelength, allows the measurement of the transient absorption spectrum at progressive delay times. White light is generated in the same way as described for the optical parametric amplifier; however, by substituting sapphire crystals of different thicknesses transient absorption spectra spanning the visible and near infrared can be measured.

After excitation by the pump pulse, the probe induces up to three different electronic transitions in the sample, as shown in Figure 2.9. It is important that the probe intensity is weak compared with the pump intensity to ensure the excited state population is not significantly altered by the probe. When the energy of the probe is resonant with the same transition as the pump, the ground state bleach is observed. In this case, the reduction of the ground state population in the presence of the pump causes a decrease in absorbance and a negative transient absorption signal is measured. This signal represents the entire excited state population of the sample. If instead the energy of the probe is resonant with the transition from the first excited state to a higher excited state, photoinduced absorption occurs. The probe is only absorbed when the first excited state is populated; therefore the transient absorption signal is positive.

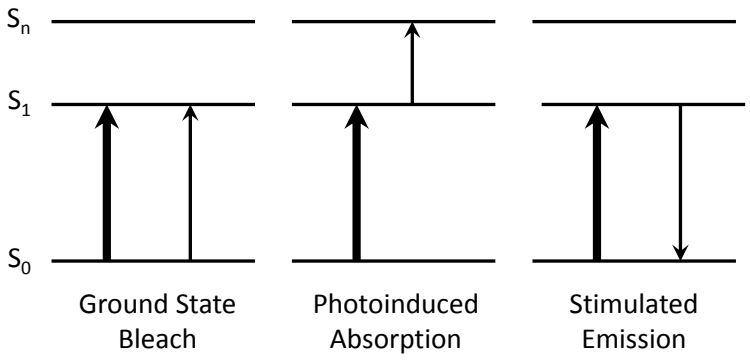


**Figure 2.9:** Possible transitions sampled by the probe pulse in a typical transient absorption experiment. The pump and probe pulses are indicated by the thick and thin lines, respectively.

Stimulated emission is the third transition that can be induced by the probe. This process involves a probe photon returning an excited state molecule to the ground state emitting an additional photon of equal energy. The probe and emitted photons are identical and therefore share the same direction of propagation. Both photons will be measured by the detector producing a negative transient absorption signal, as there is no stimulated emission and therefore fewer photons detected when the pump is absent.

Generally, stimulated emission mirrors the fluorescence profile and therefore provides the same information as fluorescence upconversion with greater practical convenience in appropriate samples when using a broadband probe. Additionally, the broadband probe allows the possibility of sampling all of these transitions concurrently.

In our experiment, shown in Figure 2.10, the ~220 mW of the oscillator (Spectra Physics, Tsunami) output was used as the seed laser for the Ti:sapphire regenerative amplifier (Spectra Physics, Spitfire Pro XP). The amplifier was pumped with an intracavity doubled, Q-switched, diode pumped Nd:YLF laser (Spectra Physics, Empower) producing 100 ns pulses with a repetition rate of 1 kHz at 527 nm split into two legs of approximately equal intensity. Ultimately, amplified pulses centred at 800 nm were 100 fs in duration with a repetition rate of 1 kHz. A portion of this output was used to generate the 500 nm pump beam using a travelling wave optical parametric amplifier (Light Conversion, TOPAS-C).

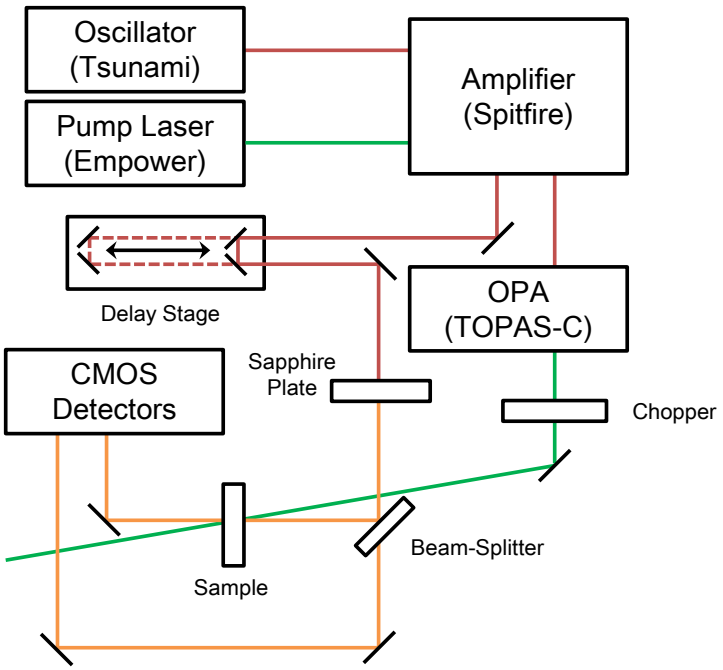


**Figure 2.10:** Diagram of transient absorption system.

Inside the transient absorption spectrometer (Ultrafast Systems, Helios) the pump beam was mechanically chopped at 500 Hz and focussed onto the sample with pulse energy of 50 nJ and beam diameter of 890 µm. Another smaller portion of the regenerative amplifier output was passed through a variable delay stage and then used to generate a white light continuum in a 2 mm sapphire plate for visible probe experiments. For near-infrared probe experiments a 13 mm sapphire plate was used.

Next, a variable beam splitter was used to divide the continuum into sample and reference beams, with the former focussed onto the sample with beam diameters of 275 and 145 µm for the visible and near-infrared probes, respectively. The pump-probe spot size ratio was kept above 3:1 in all experiments to ensure that the probe was sampling only within the excitation volume. The sample and reference beams were then directed into complementary CCD detectors for visible light or metal oxide semiconductor array detectors for near-infrared experiments.

## 2.7 Three-Pulse Transient Absorption Spectroscopy

The transient absorption experiment can be modified to accommodate a third pulse arriving at the sample shortly after the initial pump pulse, which allows examination of higher excited state lifetimes, charge separation and molecular motions not available from the traditional pump probe experiment. The function of this additional pulse is then selected by tuning its wavelength to the photoinduced absorption or stimulated emission bands in the transient absorption spectrum. Selecting a wavelength that corresponds to photoinduced absorption will repump or 'push' some of the first excited state population to a higher excited state. Recovery of the first excited state population is then monitored by the probe to determine the lifetime of the higher excited state. Photoinduced absorption of this push pulse by polarons or charge transfer states is also possible; in the latter case an increased production of free charge carriers in polymer photovoltaic devices has been demonstrated [92]. Alternatively, the wavelength of the additional pulse can be tuned to induce stimulated emission causing the population of the first excited state to be 'dumped' back to the ground state. This arrangement allows the measurement of structural changes within the ground state, such as the torsional relaxation of P3HT in dilute solutions [93].

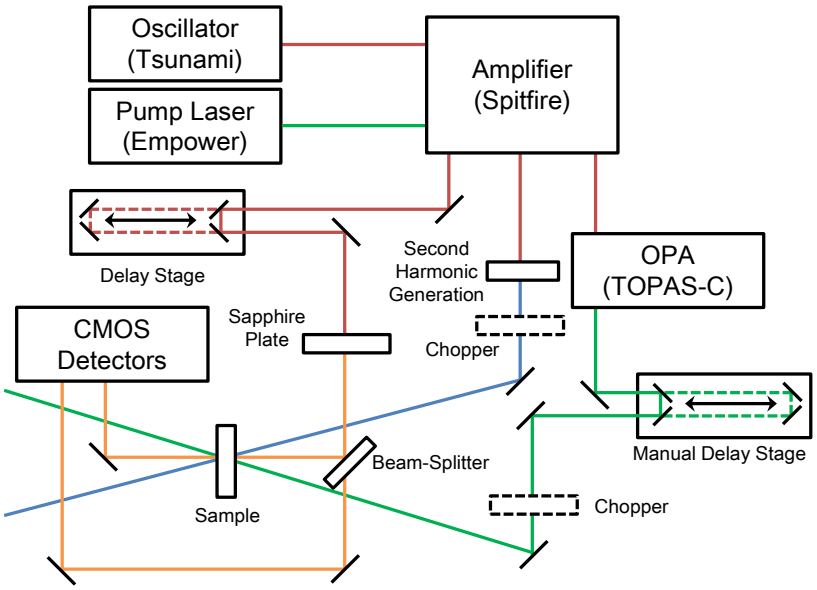


**Figure 2.11:** Diagram of three-pulse transient absorption system.

The pump-probe transient absorption system described in the previous section was modified to three-pulse setup shown in Figure 2.11. A small portion of the fundamental amplifier output was frequency doubled by a BBO crystal generating the 400 nm pump beam at a repetition rate of 1 kHz and pulse energy of 1.8 µJ was focussed to a spot diameter of 830 µm at the sample. For experiments monitoring the pump-probe signal the pump beam was then mechanically chopped at 500 Hz. The optical parametric amplifier output served as the push pulse. The push wavelength was selected as either 900 nm or 1200 nm and directed through a manual delay stage to control the pump-push delay. The push beam was focussed onto the sample with a spot diameter of 560 µm giving roughly 7:4:1 spot size ratio and 2 µJ pulse energy. The specifications of the probe light can be found in the previous section.

## 2.8 Summary

This chapter has described the operational details of laser equipment for generation of femtosecond pulses, which are a crucial component of ultrafast laser spectroscopy. These ultrafast spectroscopic techniques were used for measuring the energy and charge transfer behaviour of conjugated polymers presented in Chapters 4, 5 and 6. The competition between energy transfer and fluorescent emission allows measurement of the energy transfer rate in MEH-PPV solutions and nanoparticles by femtosecond fluorescence upconversion. This data is presented in Chapter 4. Femtosecond transient absorption was used in Chapter 5 to examine the generation and recombination charged species in composite P3HT/PCBM nanoparticles that were not observable in fluorescence-based experiments. Transient absorption was also used in Chapter 6 as the fluorescence quantum yield for P3HT nanoparticles is too low to be satisfactorily measured using fluorescence upconversion. Other spectroscopic methods, such as XPS and FT-IR, have also been briefly discussed. These techniques are crucial for the characterisation of conjugated polymer nanoparticles reported in the following chapter.

# 3 Colloidal Stability of Conjugated Polymer Nanoparticles

## 3.1 Introduction

In recent years, conjugated polymer nanoparticles have been developed as fluorescence imaging probes [58-62], ratiometric sensors [64,68-70] and most recently photothermal cancer therapy agents [67]. Such applications exploit the photostability, high fluorescence brightness and small particle diameters of these nanoparticles suspended in aqueous media without any surfactants or stabilising molecules. Despite their hydrophobic nature, aggregation of these nanoparticles is not observed for several weeks. Until now, there has been little investigation into how conjugated polymers can form nanoparticle suspensions with such long-term stability.

Aggregation of hydrophobic materials, such as these nanoparticles, in aqueous media is a thermodynamically favourable process driven by van der Waals forces [94]. Therefore, to prevent aggregation the colloid must be stabilised by opposing these attractive forces. The two primary methods used for this are electrostatic and steric

stabilisation. Electrostatic stabilisation is achieved through a tightly bound layer of charge on the particle surface, which in turn attracts ions of opposite charge forming another more diffuse layer. Together, these charged layers form the electric double layer. The characteristic thickness of the double layer ($r_D$), equal to the inverse of the Debye-Hückel parameter ($\kappa$), is dependent on the ionic strength ($I$) and temperature ($T$) of the suspension according to,

$$r_D = \frac{1}{\kappa} = \left(\frac{\varepsilon RT}{4\pi F^2 I}\right)^{1/2} \tag{3.1}$$

where $F$ is the Faraday constant, $\varepsilon$ is the relative permittivity of the medium and $R$ is the ideal gas constant [95]. If the thickness of the double layer is greater than the range of the van der Waals interaction the electrostatic repulsion between the similarly charged surfaces will sufficiently stabilise the suspension.

The other common method for preventing aggregation, steric stabilisation, requires high molecular weight amphiphilic polymers where the hydrophobic section is adsorbed to the particle surface while the hydrophilic portion interacts with the dispersant [96]. The conformation of the adsorbed polymer extends to distances comparable or greater to the van der Waals attraction and experiences steric repulsion between particles with the same coating. Polyvinyl alcohol (PVA) and polymethacrylic acid (PMAA) are typically used for the hydrophilic section of these stabilising polymers [97].

Conjugated polymers are considerably more hydrophobic than PVA and PMAA and are therefore not likely to extend to such distances beyond the surface of the particle [98]. Indeed, previous studies using AFM [56] and dynamic light scattering [99] have shown these nanoparticles prepared by reprecipitation are compact and roughly spherical as would be expected for hydrophobic polymer chains being rapidly

transferred from a good solvent (THF) into water, a poor solvent. The subsequent collapse of polymer into compact nanoparticle conformations occurs to minimise unfavourable hydrophobic-water interactions.

Aqueous suspensions of conjugated polymer nanoparticles have also been prepared by mini-emulsion and self-assembly methods [100-102]. Although these methods produce particle diameters comparable to those prepared by reprecipitation, both require additional means of stabilisation. Mini-emulsion requires dissolving the conjugated polymer in a good solvent that is immiscible with water. The mini-emulsion is created by combining this solution with water containing amphiphilic polymers or surfactants and mixing vigorously, usually by sonication. The initial solvent is then removed yielding the surfactant stabilised conjugated polymer suspension.

The self-assembly approach involves the synthesis of ionisable conjugated polymer analogues, which are combined in solution with small molecules of opposite charge to form supramolecular assemblies [103]. These water solubilising functional groups are generally attached to alkyl side chains of the predominantly hydrophobic polymers leading to amphiphilicity and stability in aqueous suspensions [104,105]. Both alternate methods require additional considerations and have a clear source of colloidal stability; however, this is not the case for nanoparticles prepared by reprecipitation.

In this chapter, the source of colloidal stability for nanoparticles prepared by reprecipitation is explored. Atomic force microscopy and zeta potential measurements were used to quantify the surface charge density. The source of this surface charge was then investigated by XPS, FT-IR and elemental analysis to determine the chemical composition of the polymer before and after nanoparticle formation. The results

presented herein indicate negatively charged defects are present on the nanoparticle surface and contribute to the colloidal stabilisation.

## 3.2 Basic Characterisation

The particle height distributions and example *in situ* AFM images of conjugated polymer nanoparticles prepared by reprecipitation are shown in Figure 3.1. Liquid samples were used to determine particle sizes representative of hydrated nanoparticles in suspension. The particle diameter measured in the lateral dimension of these images is larger than the particle heights. This is partially due to the superior resolution of AFM in the height dimension, although it also suggests the particles are somewhat flattened when deposited on the substrate. From the height distributions, the average particle diameters are smaller than 10 nm, which shows good agreement with published data. This study by Wu *et al.* [56], also concluded that nanoparticles of this size may only contain one tightly-packed polymer chain per nanoparticle.

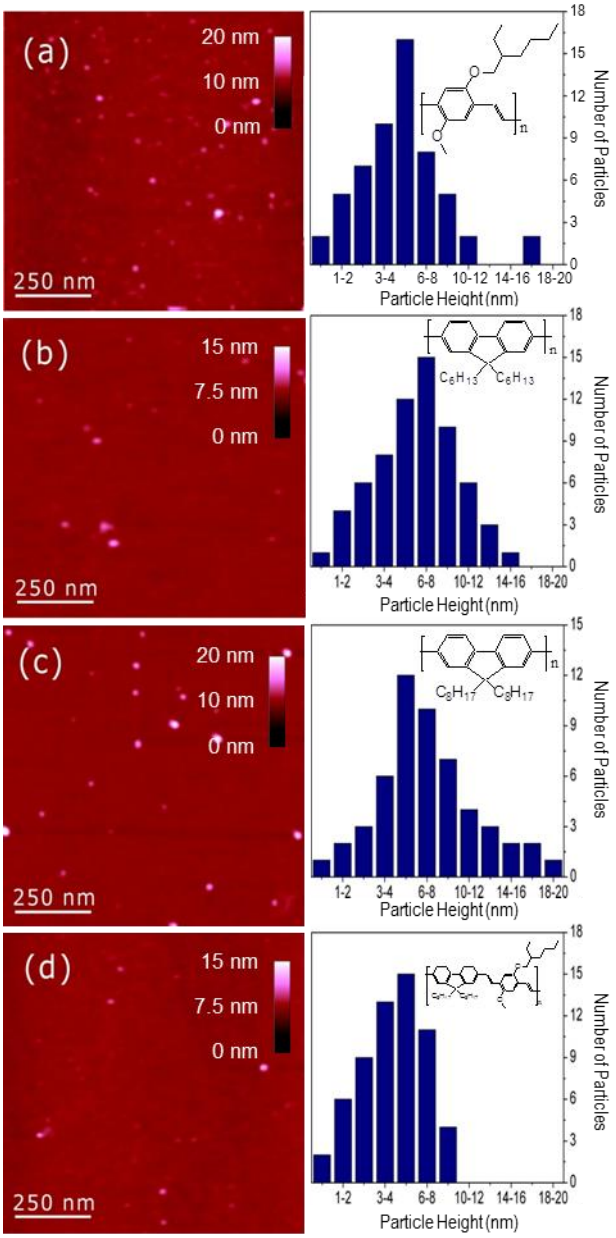


**Figure 3.1:** AFM images of in situ conjugated polymer nanoparticles (left) and particle height distributions (right) for the conjugated polymers (a) MEH-PPV, (b) PDHF, (c) PDOF and (d) PFPV. The insets show the chemical structures of each polymer.

The steady-state absorption and fluorescence spectra for polymer solutions in THF and aqueous nanoparticle suspensions, shown in Figure 3.2, exhibit differences that have also been reported previously [56,65]. Briefly, nanoparticle absorption and fluorescence spectra are blue and red shifted, respectively, relative to the corresponding

polymer spectra. The change in the absorption spectrum has been explained by the shortening of chromophores upon nanoparticle formation [56]; however, it could also be explained by the change of dispersant. To distinguish between the effects of dispersant and polymer conformation, films of polymer and nanoparticle samples were prepared. It is important to note that AFM images from Figure 3.1 indicated the nanoparticle structure was retained when prepared as a film.

Figure 3.3 shows the absorption and fluorescence spectra of the nanoparticle film are both red shifted relative to the polymer. Lower energy absorption is consistent with an increase in the average chromophore length for the nanoparticle sample. Such behaviour is known to occur for conjugated polymers, including PDOF, that form semicrystalline aggregates in films [106,107]. Similarly, single molecule investigations of MEH-PPV have shown the formation of ordered aggregate structures [108]. This change in chromophore length also causes the red shift of the fluorescence spectra. All polymers exhibited the same behaviour with the exception of PDOF, where the fluorescence spectrum of the nanoparticles coincided with that of the polymer film. These spectra both resemble the semicrystalline β-phase emission indicating both samples are highly ordered [76].

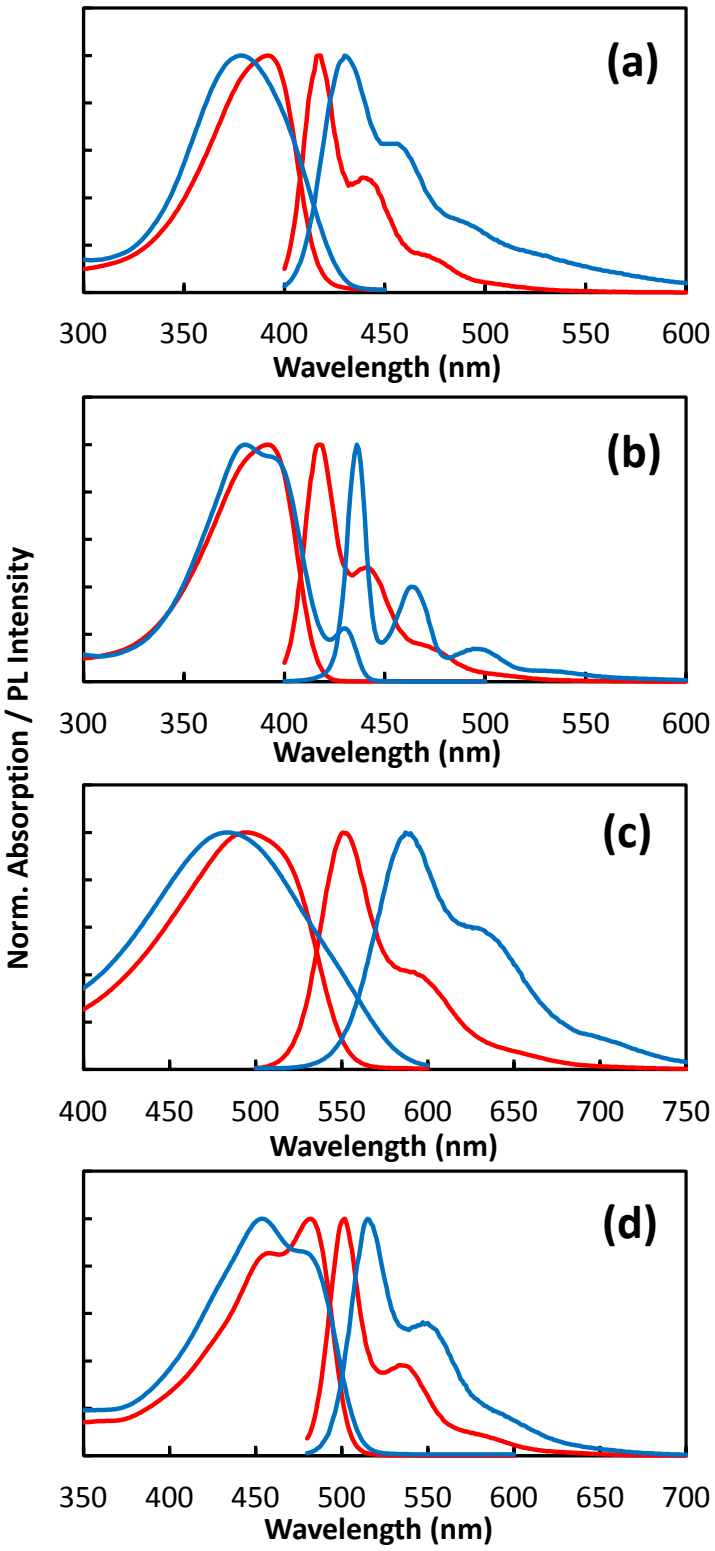


**Figure 3.2:** Normalised absorption and fluorescence spectra of the polymer solution in THF (red) and aqueous nanoparticle suspensions (blue) for (a) PDHF, (b) PDOF, (c) MEH-PPV and (d) PFPV.

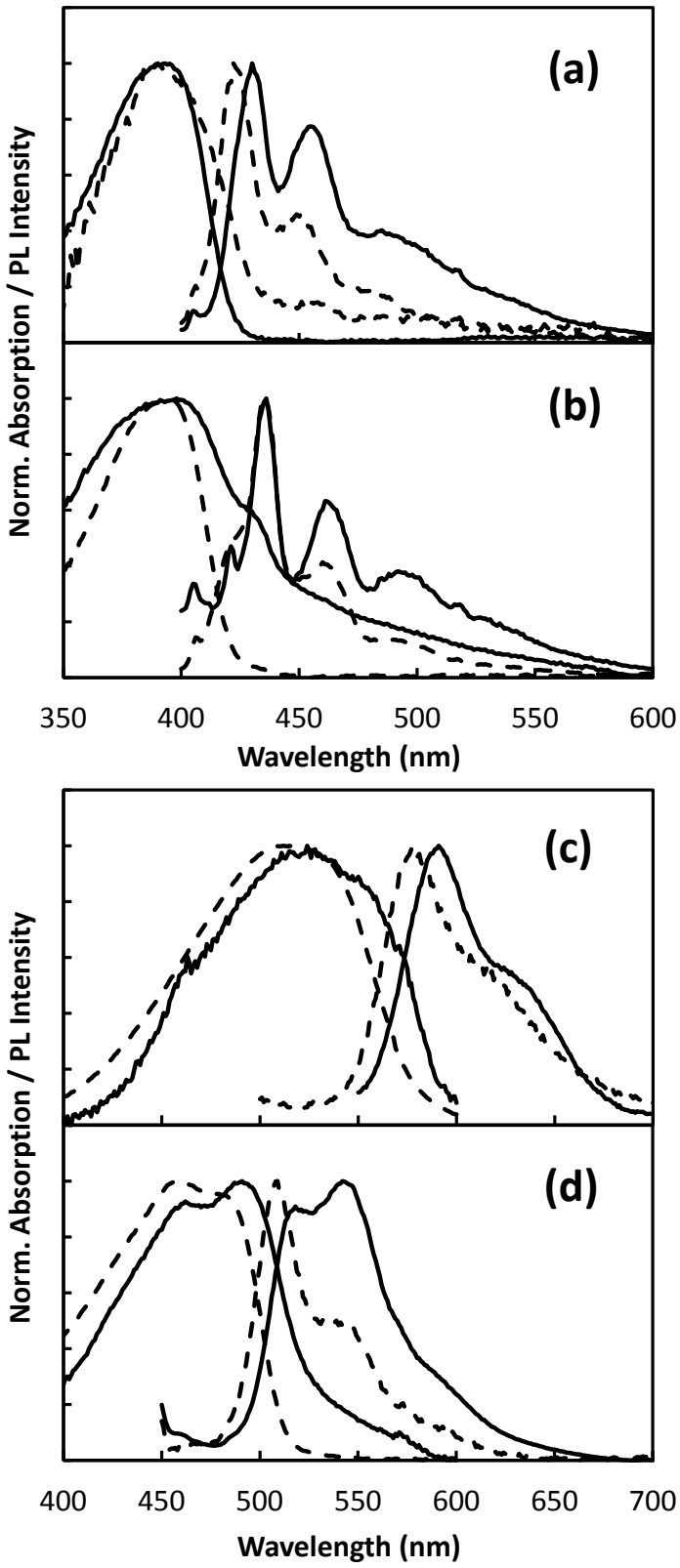


**Figure 3.3:** Normalised absorption and fluorescence spectra of the polymer (dashed) and nanoparticle (solid) films for (a) PDHF, (b) PDOF, (c) MEH-PPV and (d) PFPV.

These nanoparticles show long term colloidal stability with visible aggregation only occurring after several weeks despite the notably hydrophobic chemical structures and the lack of additional surfactants or other stabilising molecules. As discussed earlier, suspensions of hydrophobic materials in water are often stabilised by repulsion between the similarly charged surfaces of suspended particles. The electric potential of the particle surface relative to the bulk of the dispersant, called the zeta potential, is one way of quantifying this surface charge. The zeta potential distribution of MEH-PPV nanoparticles at pH 7, shown in Figure 3.4, has an average of –36.8 mV and width of 6.8 mV. The average of zeta potentials of PFPV, PDOF and PDHF nanoparticles also measured at pH 7 were -36.9 mV, -43.3 mV and -44.0 mV, respectively.

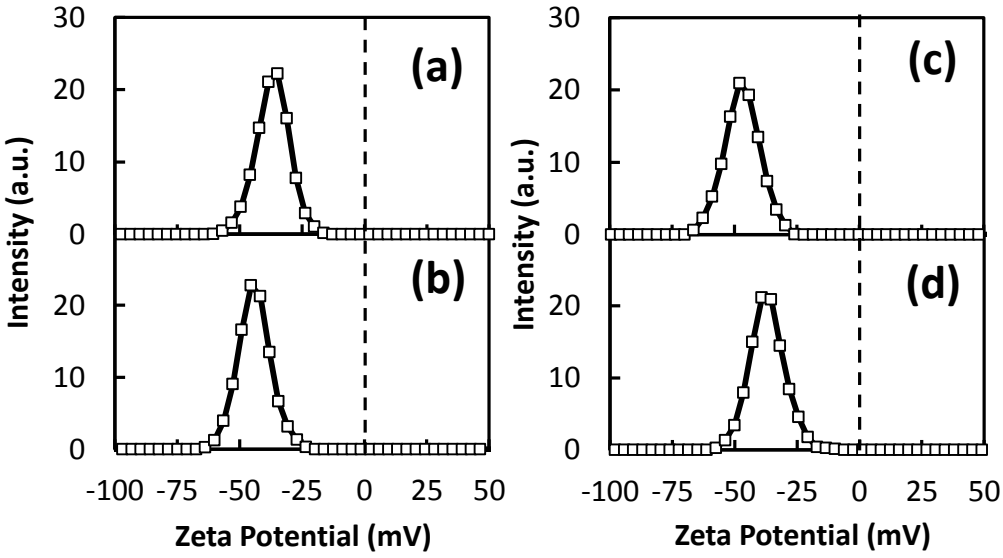


**Figure 3.4:** Zeta potential distributions of (a) MEH-PPV, (b) PDHF, (c) PDOF and (d) PFPV nanoparticles at pH 7 with a NaCl concentration of 5 mM.

The surface charge density ($\sigma_0$) is a commonly used indicator of colloidal stability. It is calculated from the zeta potential ($\psi_0$) and the radius of the particle ($a$) according to

$$\sigma_0 = \frac{\varepsilon\psi_0}{a}(1 + \kappa a), \tag{3.2}$$

where $\varepsilon$ is the permittivity of the medium ($6.95\times10^{-10}$ C/Vm, for water) and $\kappa$ is the Debye-Hückel parameter calculated using Eq. (3.1) [109]. Zeta potential measurements were taken at a NaCl concentration of 5 mM and particle radii were determined by the centres of the particle height distributions in Figure 3.1 with values ranging from 2 to 3 nm. The surface charge densities for each polymer nanoparticle variety are listed in Table 3.1. The surface charge density of MEH-PPV nanoparticles is 14.3 mC/m$^2$, which is comparable to reported stabilities of polyelectrolyte-coated polymeric nanoparticles and citrate stabilised gold nanoparticles [110,111].

**Table 3.1:** Surface charge densities for conjugated polymer nanoparticles.

| **Polymer** | **$\sigma_0$ (mC/m$^2$)** |
|---|---|
| MEH-PPV | 14.4 ± 1.4 |
| PDHF | 15.2 ± 1.2 |
| PDOF | 15.0 ± 1.2 |
| PFPV | 17.0 ± 1.7 |

For organic materials, charge is often introduced through ionisable functional groups. Adjusting the pH of the dispersant will result in protonation or deprotonation depending on the nature of functional groups present. The pH at which the charge of these groups is neutralised, known as the isoelectric point, assists in the identification of these functional groups. The zeta potential of the nanoparticles was measured for a range of pH levels from neutral pH 7 to pH 3 in an attempt to determine the isoelectric point. Nanoparticles began to form visible aggregates below pH 4, although the negative surface charge remained as high as 15 mV in magnitude at pH 3. Therefore, a surface charge density on the order of 6.5 mC/m$^2$ is sufficient to stabilise the nanoparticles. Additionally, as it was not possible to determine the isoelectric point, the

source of the surface charge remains unclear and will be explored in the following section.

## 3.3 Presence of Surface Defects

In order to rationalise the presence of surface charge the chemical composition of the polymer before and after nanoparticle preparation was studied. The FT-IR spectra of all polymer and nanoparticle samples are shown in Figure 3.5. The polymer spectra are dominated by aliphatic and aromatic C–H stretches at 2800-3100 $cm^{-1}$ and the methylene scissoring mode at 1460 $cm^{-1}$. For MEH-PPV and PFPV, additional peaks are observed below 1300 $cm^{-1}$ corresponding to C–O stretches. It should be noted that the PFPV spectrum has a sharp absorption at 1648 $cm^{-1}$ indicating the quality of this polymer is no longer pristine. The nanoparticle spectra each show three additional peaks in the carbonyl region of the spectrum at 1730, 1670 and 1600 $cm^{-1}$, which are assigned to aliphatic C=O, aromatic C=O and C=O induced aromatic stretches, respectively [112,113]. These data clearly show there are oxidative changes to the chemical structure of the polymer during the nanoparticle preparation.

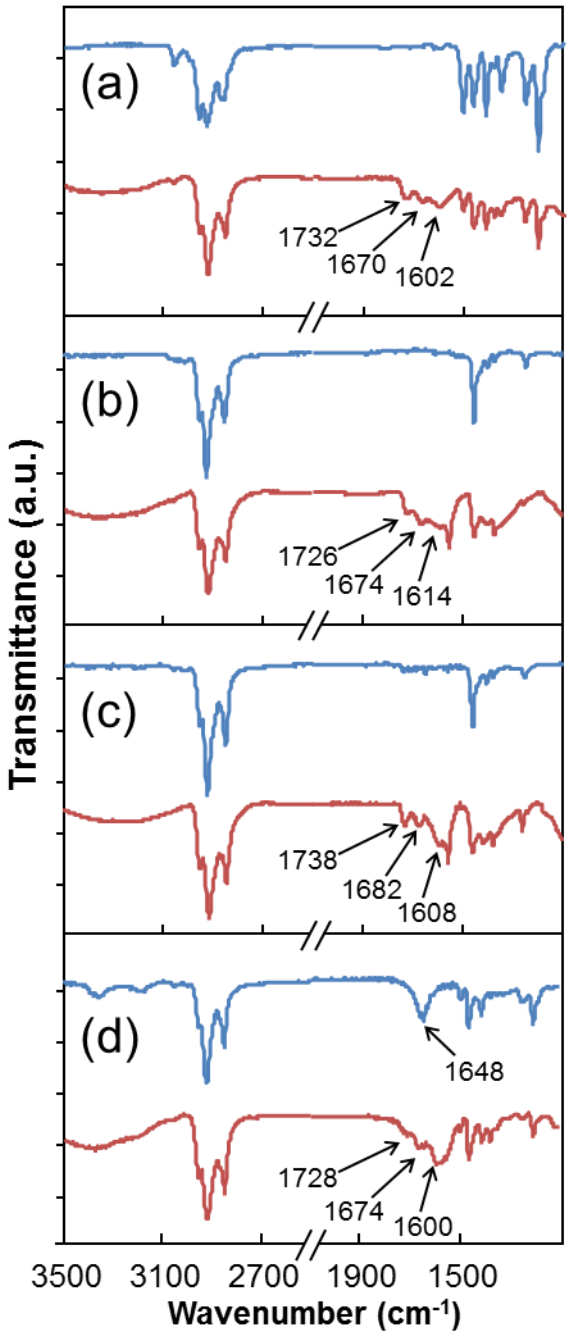


**Figure 3.5:** FT-IR spectra of conjugated polymers (a) MEH-PPV, (b) PDHF , (c) PDOF and (d) PFPV films of pristine polymer (blue) and polymer nanoparticles (red).

To further examine these oxidative changes carbon 1s XPS data were collected for polymer and nanoparticle films, as shown in Figure 3.6. All spectra were fitted with a weighted Gaussian (70%) Lorentzian (30%) function using CasaXPS 2.3 software. The major aliphatic/aromatic C 1s peak was used as the internal calibration standard and

assigned to a binding energy of 285.0 eV. When components of the spectra were not clearly resolved, the width of the component was fixed to the same width as the most well-defined component. The best fit parameters are listed in Table 3.2.

The MEH-PPV and PFPV polymer spectra were fitted with two components, $C_1$ at 285.0 eV and $C_2$ at 286.2 eV, corresponding to the carbon atoms of hydrocarbon and ester groups, respectively. The MEH-PPV spectrum shows components and peak positions in good agreement with published data [112,114]. Polyfluorene data indicate only the hydrocarbon component is present, which is consistent with the chemical structure of the pristine polymers. The MEH-PPV nanoparticle spectrum shows two additional components not observed for the polymer at 287.9 eV ($C_3$) and 289.4 eV ($C_4$). As these components have higher binding energies they indicate higher oxidation states of carbon and are therefore assigned to C=O and O=C–O groups, respectively. The difference in binding energy of ~1.4 eV shows good agreement with the expected shift for each additional C–O bond [115]. The other difference between the MEH-PPV polymer and nanoparticle spectra is the reversal in amplitudes for the two lowest energy components. The PFPV nanoparticle spectrum shows the $C_4$ component at 288.7 eV; however, the $C_3$ component is notably absent. Finally, the nanoparticle spectra of PDHF and PDOF show similar changes from their corresponding polymer data. The three new components present in the polyfluorene nanoparticle spectra at 286.0 eV, 287.3 eV and ~289.0 eV are assigned to the same functional groups observed in MEH-PPV nanoparticles. The XPS and FT-IR data presented here show good agreement and give strong evidence of oxidation during the preparation of nanoparticles, including the possibility of carboxylate functional groups that contribute to the negative surface charge.

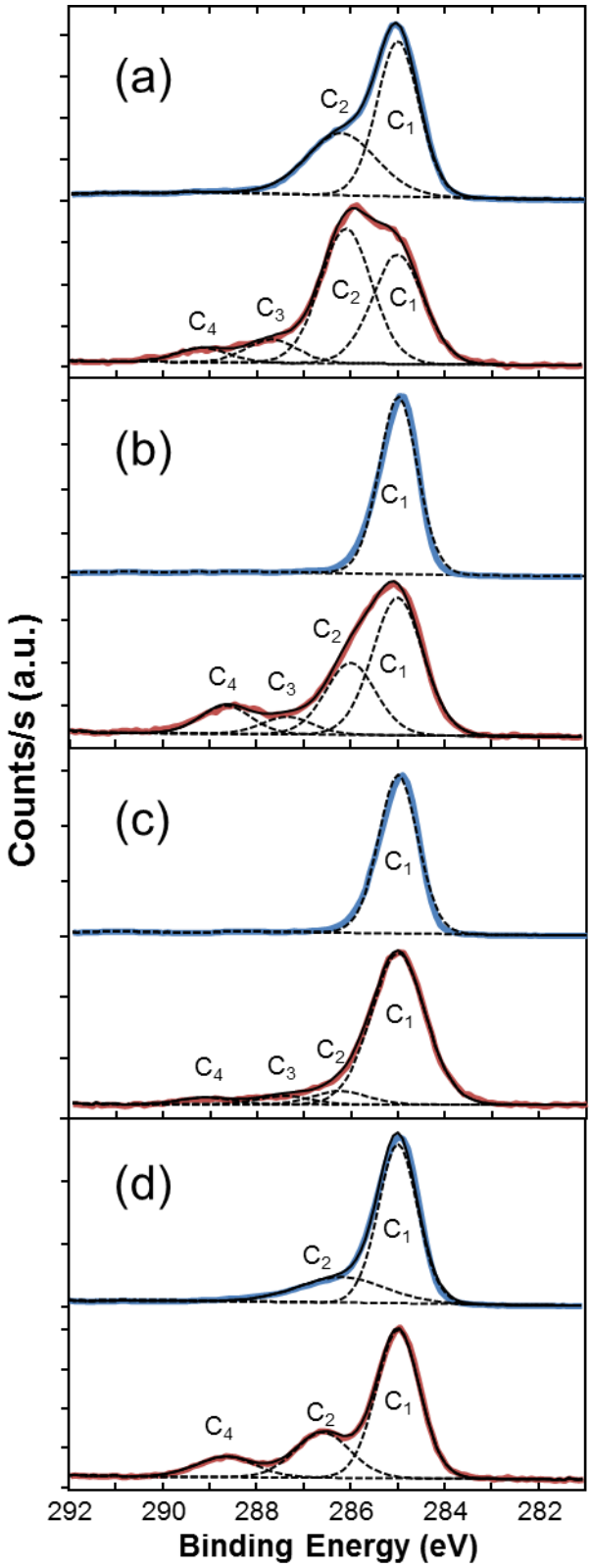


**Figure 3.6:** C 1s XPS spectra and fitted components of (a) MEH-PPV, (b) PDHF, (c) PDOF and (d) PFPV films of pristine polymer (blue) and films of nanoparticles (red).

**Table 3.2:** XPS fitting parameters for pristine polymer and nanoparticle samples as determined using CasaXPS.

| **Polymer** | **$C_1$** pos/fwhm/%area | **$C_2$** pos/fwhm/%area | **$C_3$** pos/fwhm/%area | **$C_4$** pos/fwhm/%area |
|---|---|---|---|---|
| MEH-PPV | 285.0/1.0/60 | 286.2/1.7/40 | | |
| PDHF | 285.0/0.9/100 | | | |
| PDOF | 285.0/1.0/100 | | | |
| PFPV | 285.0/1.0/73 | 286.2/2.2/26 | | |
| **Nanoparticle** | **$C_1$** pos/fwhm/%area | **$C_2$** pos/fwhm/%area | **$C_3$** pos/fwhm/%area | **$C_4$** pos/fwhm/%area |
| MEH-PPV | 285.0/1.2/31 | 286.1/1.4/56 | 287.9/1.4/8 | 289.4/1.4/5 |
| PDHF | 285.0/1.3/54 | 286.0/1.3/28 | 287.3/1.3/7 | 288.7/1.3/11 |
| PDOF | 285.0/1.3/83 | 286.2/1.3/8 | 287.4/1.3/5 | 289.1/1.3/4 |
| PFPV | 285.0/1.1/63 | 286.6/1.4/25 | | 288.7/1.5/12 |

Elemental analysis was used to validate the XPS data and quantify the oxygen content of polymer and nanoparticle samples more accurately; these data are shown in Table 3.3. The measured composition of the polymers closely reflects the calculated composition based on the monomer structure of the polymers. Comparing the relative area of $C_2$ with elemental analysis data for the MEH-PPV polymer sample shows extremely high oxygen concentrations for the XPS data. Oxygen is known to shift the binding energy of secondary carbon atoms by ~0.4 eV [115], which could partially account for the increased area. Even disregarding this component and considering only $C_3$ and $C_4$ of the nanoparticle samples, the oxygen content by XPS is equal or greater than the oxygen content determined by elemental analysis for all polymers. This result combined with the surface sensitive nature of XPS suggests the oxygen concentration is

elevated at the particle surface. Previous studies have shown polymer chains collapse in water such that hydrophilic groups are arranged on the surface of the particle while hydrophobic sections are restricted to the core [116,117].

**Table 3.3:** Elemental composition of pristine conjugated polymer and nanoparticle samples in mole%. Expected mole% calculated from the monomer structures are shown in parentheses.

| **Polymer** | **C** | **H** | **N** | **O** |
|---|---|---|---|---|
| MEH-PPV | 38.91 (39.53) | 56.46 (55.81) | | 4.69 (4.65) |
| PDHF | 43.32 (43.86) | 56.68 (56.14) | | 0.01 (0.00) |
| PDOF | 42.05 (42.03) | 58.03 (57.97) | | –0.08 (0.00) |
| PFPV | 40.37 (41.38) | 57.05 (56.90) | | 2.58 (1.72) |
| **Nanoparticles** | **C** | **H** | **N** | **O** |
| MEH-PPV | 34.28 | 52.68 | 0.39 | 12.64 |
| PDHF | 37.30 | 48.84 | 0.41 | 13.45 |
| PDOF | 38.48 | 54.45 | 0.22 | 6.84 |
| PFPV | 35.79 | 51.96 | 0.36 | 11.88 |

The possibilities of photo-oxidation and oxidation by organic peroxides formed in THF have been considered. Nanoparticle samples were exposed to ambient light for several hours and showed less than 1% decrease in absorption. Gentle heating and the lack of peroxide inhibitor is known to produce organic peroxides in THF within several hours [118]. Solutions of each polymer in THF monitored by FT-IR spectroscopy showed no increased absorption in the carbonyl region over such periods. Therefore, there is little, if any, oxidation of the polymer through these processes.

Many studies have investigated physisorption of hydroxide anions to the surface of hydrophobic aggregates in water as an alternative form of stabilisation [119-123]; however, these findings are somewhat controversial [124,125]. These studies report zeta potential measurements similar in magnitude to those measured for conjugated polymer nanoparticles, also without any stabilising molecules. Therefore, oxidation of the polymer chain during nanoparticle preparation may not be the only source of colloidal stabilisation, but rather a contributing factor.

## 3.4 Conclusions

This chapter has shown conjugated polymer nanoparticles possess a negative surface charge on the order of 15 $mC/m^2$ capable of preventing their aggregation for several weeks or longer. XPS and FT-IR data clearly shows oxidation of the polymer during nanoparticle preparation introducing carbonyl and even carboxylate functional groups that produce negative surface charge. The oxygen content as a result of oxidation was found to be 7-13% by elemental analysis. Photo-oxidation and oxidation by peroxides known to form in THF were also considered but showed no evidence of chemically modifying the polymer structure. Other effects, such as the adsorption of hydroxide ions to the particle surface, might also contribute to the stabilisation of these nanoparticles.

# 4 Excitation Energy Transfer in Conjugated Polymer Nanoparticles

## 4.1 Introduction

Conjugated polymers have proven to be impressive materials for organic photovoltaics [126-128] and electroluminescent applications [129,130]. One crucial area of investigation is the polymer morphology and its effect on the energy transport processes in these devices [131-134]. One study by Huyal *et al.* [80], demonstrated increased fluorescence quantum yields in polyfluorene nanoparticle films compared to polymer films cast from THF. From the dependence of the fluorescence profile on nanoparticle size, it was concluded that smaller nanoparticles have a more compact internal structure. However, by solely relying on spectral shifts in steady-state optical spectra of solvated samples at room temperature, it is difficult to elucidate detailed information regarding the polymer conformation. Instead, several studies over the past decade have combined different forms of ultrafast spectroscopy and Monte Carlo simulations of energy transfer to yield representative polymer structures [7,8,19,135-137].

This approach was first demonstrated by Grage *et al.*, for solutions [7], and later, films [135] of phenyl-substituted polythiophenes. In these studies, the anisotropy decay measured by transient absorption was used to monitor the evolution of energy transfer. The polymer structure in solution was simulated by a series of vectors each representing two adjacent monomer units of the polymer chain. The direction of each vector was defined by a Gaussian distribution of angles relative to the preceding vector. Energy transfer simulations following the Förster mechanism were performed using the distance and relative orientation between vectors from the simulated polymer structures. The polymer conformation was controlled by the width of the Gaussian distribution, called the disorder parameter, obtained from fitting the experimental anisotropy decay with the simulated data. In this way, representative polymer structures can be generated from ultrafast spectroscopic data.

From this first study, the substituted polythiophene was found to adopt worm-like conformations in solution with the excitation energy transferred through an average of six chromophores before becoming trapped. The polymer conformation was found to be similar in films [135], while another study concerning solution samples of MEH-PPV with partially broken conjugation showed greater disorder and shorter average separation between chromophores than the substituted polythiophenes [8]. Further developments were made by Westenhoff *et al.*, including the introduction of the line-dipole approximation [19] and torsional potentials [136] between adjacent monomers. The common thread of these studies is the simplicity of the polymer model allowing simulation of chains comparable in length to those used in experiments.

In this chapter, the energy transfer behaviour of the conjugated polymer in extended and nanoparticle conformations is examined. The polymer, MEH-PPV, was used as a

model polymer for the following experiments, although it is expected that nanoparticles of other conjugated polymers prepared by reprecipitation would display analogous energy transfer behaviour. Time-resolved isotropic emission transients were collected by femtosecond fluorescence upconversion to monitor the excited state populations for subsets of chromophores. The rate of energy transfer was then measured directly from the fluorescence anisotropy decay. Anisotropy data were simulated independently using a coarse-grained MEH-PPV model and a Monte Carlo energy transfer algorithm to provide polymer structures consistent with the experimental data for each sample.

## 4.2 Time-Resolved Fluorescence Data

The changes in absorption and fluorescence spectra of MEH-PPV upon nanoparticle formation have been described in Chapter 3.2. Briefly, the absorption maximum of the nanoparticle film was red-shifted by 10 nm and the fluorescence maximum was red-shifted by 35 nm. These shifts were attributed to the lengthening of chromophores associated with the preformed nanoparticle structure prior to film casting. Solution based samples were used for the following time-resolved fluorescence experiments, therefore it is more informative to consider the spectral differences between solutions of MEH-PPV in THF and aqueous suspensions of MEH-PPV nanoparticles, which are shown in Figure 4.1. The absorption spectrum of the polymer solution in THF is blue-shifted by 20 nm compared to the polymer film and the absorption maximum of the nanoparticle suspension occurs a further 15 nm higher in energy. Polymer solutions in THF are reasonably well-solvated, although not to the same extent as many aromatic solvents. Nevertheless, these polymer chains exhibit a relatively small degree of interchain interaction compared to the film and nanoparticle samples. This is also

demonstrated by the fluorescence spectra of the nanoparticle film and suspension, which are red-shifted by around 40 nm compared to the 550-nm peak of the polymer solution. The red-shifts of the film and nanoparticle spectra are clear indications of aggregate formation and the presence of interchain excitons.

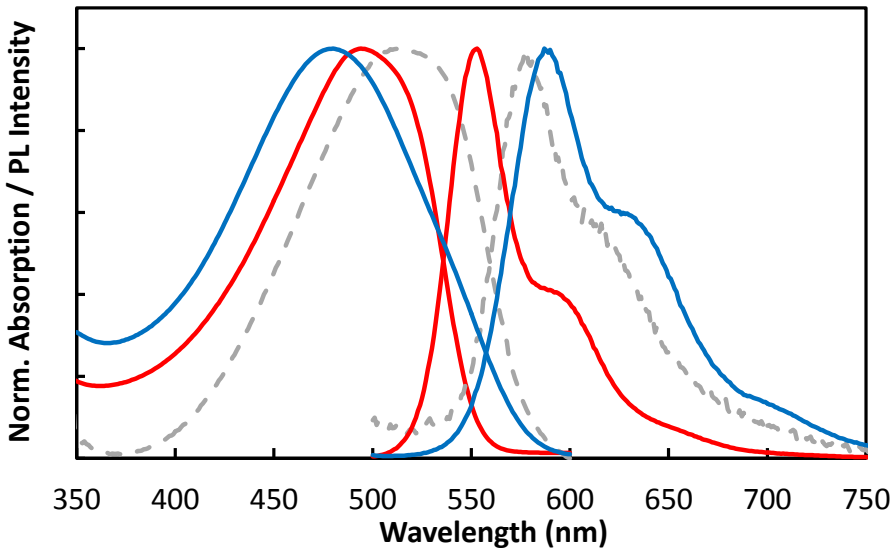


**Figure 4.1:** Absorption and photoluminescence spectra of MEH-PPV in aqueous suspension (blue) and dissolved in THF (red). Polymer film spectra are also shown (grey) for comparison.

The influence of polymer conformation on the optical properties of MEH-PPV was further investigated through femtosecond fluorescence upconversion experiments. Isotropic fluorescence decay data were collected for MEH-PPV in THF at several emission wavelengths, a selection of these is shown in Figure 4.2. Each fluorescence decay transient was fit with the sum of exponential terms using the fewest terms that adequately described the data; the best fit parameters for the MEH-PPV in THF data shown here are listed in Table 4.1. The fluorescence intensity at 500 nm, 520 nm and 670 nm is proportional to the populations of high, medium and low energy chromophores, respectively.

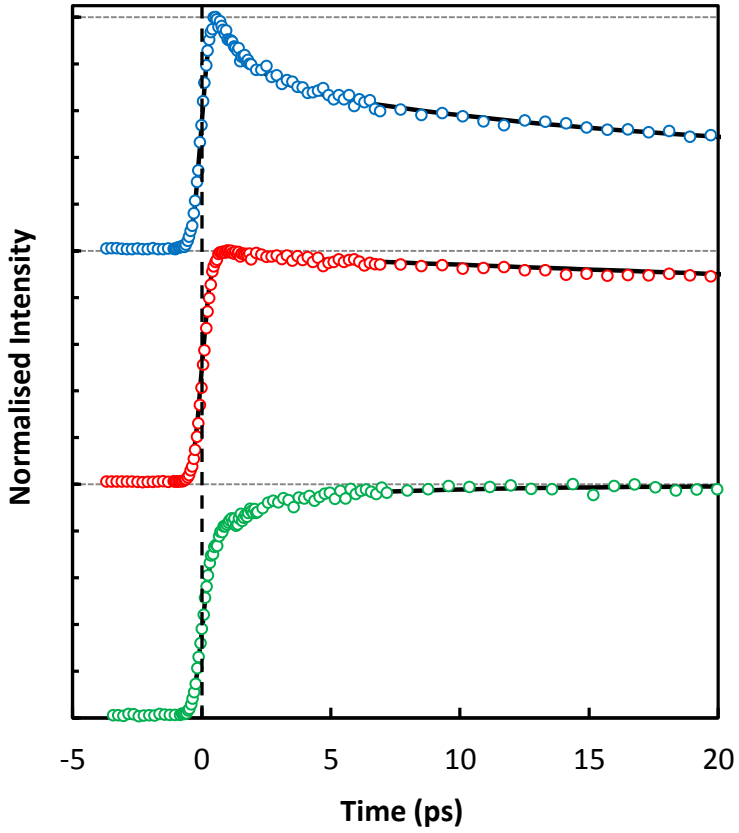


**Figure 4.2:** Isotropic time-resolved fluorescence decay of MEH-PPV in THF at emission wavelengths: 500 nm (top), 520 nm (middle) and 670 nm (bottom).

The initial decay of the high energy chromophore population was rapid with a time constant of ~1 ps ($\tau_1$), followed by another slightly slower 12 ps decay component ($\tau_2$). After the first 50 ps the population decays according to the fluorescence lifetime, or exciton recombination, of MEH-PPV ($\tau_3$), which is approximately 200 ps in THF [9]. Intermediate energy chromophores do not exhibit any deviation from the fluorescence lifetime even at times shortly after excitation and can therefore be described by a single decay constant. The population of the lowest energy chromophore subset grows in the first 5 ps with a time constant comparable to the initial decay component ($\tau_1$) observed for the high energy chromophores. A subsequent growth component ($\tau_2$), slower than the first, is also present in the 670 nm decay. These initial growth components can be difficult to determine accurately due to the rise associated with the instrument response

function. For the data presented here, the instrument response function was included in the iterative reconvolution fitting algorithm used by the Surface Xplorer software from Ultrafast Systems. The width of the instrument response function was similar at all emission wavelengths, which suggests the time constants for these growth components are not significantly influenced by the instrument response parameter.

**Table 4.1:** Fitted parameters for isotropic emission of MEH-PPV in THF. The errors in $\boldsymbol{\tau_2}$ and $\boldsymbol{\tau_3}$ are less than 25%, while the errors in $\boldsymbol{\tau_1}$ are up to 1 ps as this time constant is close to the instrument response function.

| **Wavelength (nm)** | $\mathbf{a_1}$ | $\boldsymbol{\tau_1}$ **(ps)** | $\mathbf{a_2}$ | $\boldsymbol{\tau_2}$ **(ps)** | $\mathbf{a_3}$ | $\boldsymbol{\tau_3}$ **(ps)** |
|---|---|---|---|---|---|---|
| 500 | 0.36 | 1.2 | 0.24 | 12 | 0.40 | 206 |
| 520 | - | - | - | - | 1.00 | 240 |
| 670 | -0.14 | 1.5 | -0.16 | 27 | 0.7 | 240 |

Energy transfer is well known to occur on the same time scales as these two components [138-140]. Additionally, the decay at 500 nm and simultaneous growth at 670 nm is consistent with energy transfer from high to low energy chromophores. This behaviour can be alternatively considered as a time-dependent red shift in the fluorescence spectrum, showing the excitation energy decreases on short timescales. However, torsional and solvent relaxations also manifest as a shift in emission energy [141,142]. To confirm the assignment of energy transfer to these decay components, polarisation dependent experiments were performed, which will be discussed shortly.

The MEH-PPV nanoparticle fluorescence decays are shown in Figure 4.3, with a comparison of polymer and nanoparticle samples in the top panel. The nanoparticle decay is much faster than that of the polymer, which is reflected by the decrease in

fluorescence quantum yield from ~0.27 for the polymer in THF [9], to 0.03 measured here for aqueous suspensions of nanoparticles [82]. One earlier report has shown a slight increase in fluorescence lifetime of films relative to a good solvent environment [143,144]. The comparison of fluorescence spectra made earlier shows the similarities of film and nanoparticle samples, this shows the position of the emission spectrum is more strongly dependent on the interchain spacing rather than the solvent and therefore the shorter fluorescence lifetime must be caused by the solvent (i.e. the presence of water) and not aggregation of polymer chains.

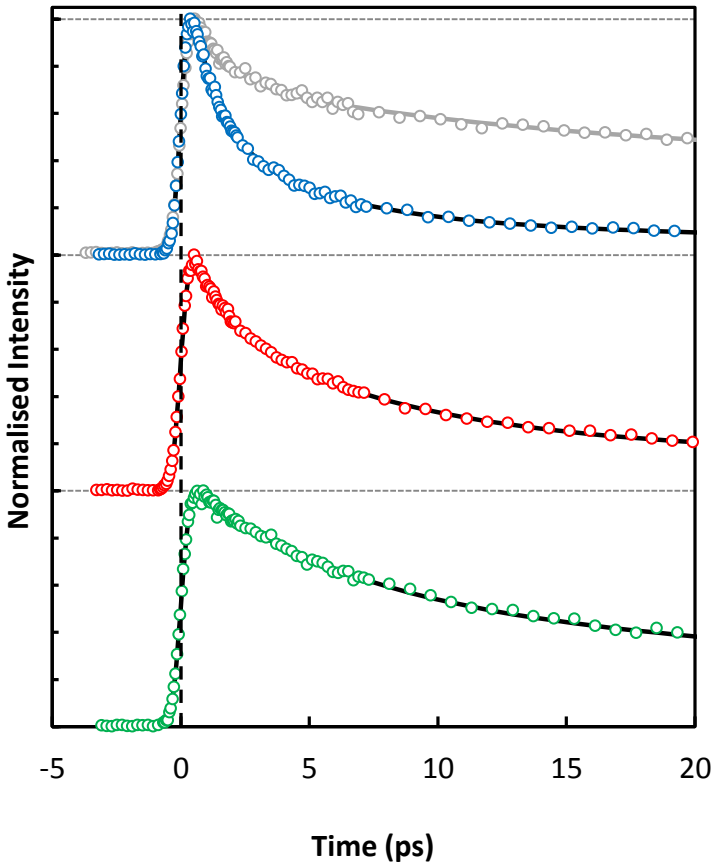


**Figure 4.3:** Isotropic time-resolved fluorescence decay of MEH-PPV nanoparticles in water at emission wavelengths: 530 nm (top), 550 nm (middle) and 620 nm (bottom). The emission of MEH-PPV in THF at 500 nm is shown in the top panel (grey) for comparison.

The fitting parameters for the time-resolved emission of the nanoparticles at 530 nm, 550 nm and 660 nm are listed in Table 4.2. Again, these represent the populations of high, intermediate and low energy chromophores; however, the emission was monitored at longer wavelengths owing to the red-shift of the fluorescence spectrum. At 530 nm, the decay is described by three exponential decay components. The two fastest decay components are 1 ps ($\tau_1$) and 4.2 ps ($\tau_2$), which are not dissimilar to the highest energy emission observed for the polymer sample. The third component ($\tau_3$) has a 40 ps time constant, considerably shorter than the fluorescence lifetime of the polymer in THF. The decay of the intermediate chromophore population is described by similar time

constants; however, the relative amplitude of the first component is reduced in favour of the slower components, resulting in a longer average decay than the highest energy chromophores. Interestingly, the 1 ps component is not observed in the 660 nm decay, which was fit with two similarly weighted time constants of 8.7 ps and 63 ps. The growth in fluorescence intensity observed for the polymer at low emission energies was not present in the nanoparticle sample due to the significantly shorter fluorescence lifetime. Instead, energy transfer from high to low energy chromophores appears as a decrease in the rate of fluorescence decay with decreasing emission energy at short delay times. This is clearly demonstrated by the decrease in the contribution from the fastest decay component in favour of the fluorescence lifetime component.

**Table 4.2:** Fitted parameters for isotropic emission of MEH-PPV nanoparticles. The errors in $\boldsymbol{\tau_2}$ and $\boldsymbol{\tau_3}$ are less than 25%, while the errors in $\boldsymbol{\tau_1}$ are up to 0.5 ps as this time constant is close to the instrument response function.

| **Wavelength (nm)** | $\mathbf{a_1}$ | $\boldsymbol{\tau_1}$ **(ps)** | $\mathbf{a_2}$ | $\boldsymbol{\tau_2}$ **(ps)** | $\mathbf{a_3}$ | $\boldsymbol{\tau_3}$ **(ps)** |
|---|---|---|---|---|---|---|
| 530 | 0.56 | 1.0 | 0.33 | 4.2 | 0.11 | 38 |
| 550 | 0.29 | 1.1 | 0.47 | 5.8 | 0.25 | 45 |
| 660 | - | - | 0.38 | 8.7 | 0.62 | 63 |

The rate of energy transfer in polymer and nanoparticle samples was measured directly by time-resolved fluorescence anisotropy experiments at 560 nm and 580 nm, respectively. These data are shown in Figure 4.4 with corresponding fitting parameters listed in Table 4.3. Due to the short fluorescence lifetime of the nanoparticles, after ~20 ps the fluorescence intensity is too low to accurately determine the anisotropy. The polymer sample has a much longer fluorescence lifetime, which allows the anisotropy to be measured for up to 500 ps, although only the first 50 ps are shown for comparison.

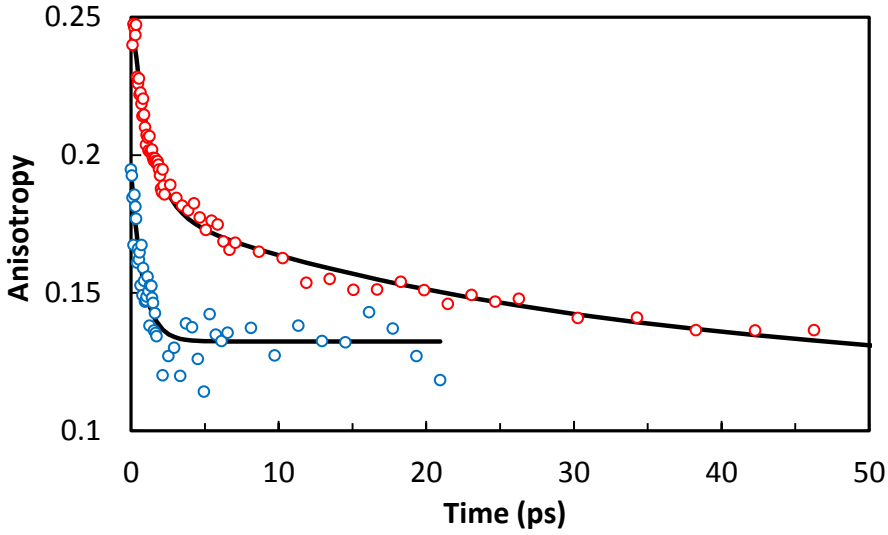


**Figure 4.4:** Fluorescence anisotropy decay for MEH-PPV in THF (red) and MEH-PPV nanoparticles (blue).

Before the anisotropy decay can be discussed solely in terms of energy transfer, it is important to consider other potential causes of anisotropy decay such as the Brownian motion of the chromophore. This can be estimated using a prolate ellipsoid to represent the chromophore, and Perrin's equations [145,146]. The ellipsoid has a principle axis of 4.69 nm and two equal minor axes of 1.05 nm corresponding to the dimensions of the average chromophore length in MEH-PPV of seven monomer units. The calculated rotational time constant about the short axis is 8 ns, given the viscosity of THF is 0.48 mPa.s at 20°C. This shows the required time scale for rotation of the chromophore in solution is exceedingly long and therefore the contribution to the anisotropy decay through Brownian motion is negligible. For a nanoparticle chromophore in water this decay time constant is longer still as the viscosity of water is greater than THF and the compact conformation is likely to considerably hinder any torsional motions.

The theoretical maximum anisotropy value for systems such as these is 0.4, which is significantly greater than the initial values measured here. The difference indicates there

is some reorientation of the transition dipole within the instrument response function, roughly 300 fs for the polymer in THF. This behaviour is well-known to occur in conjugated polymers, including MEH-PPV, and has been attributed to exciton localisation [139,140,147]. Specifically, initial excitations span kinks or bends that would ordinarily break conjugation, thereby incorporating several chromophores, before localising onto one of these constituent chromophores. One study has shown that the initial anisotropy is indicative of the number of kinks in the polymer chain and therefore the extent of polymer disorder [139]. The measured value for the nanoparticle sample, 0.20 ± 0.03, corresponds to a 36° rotation of the transition dipole moment. The initial anisotropy of the nanoparticle is less than 0.25 ± 0.01, the initial anisotropy of the polymer, indicating greater disorder in the nanoparticles.

**Table 4.3:** Fitted parameters for time-resolved fluorescence anisotropy decays. The errors in these time constants are less than 25%.

| | $a_1$ | $\tau_1$ (ps) | $a_2$ | $\tau_2$ (ps) | $a_3$ | $\tau_3$ (ps) | $r_\infty$ |
|---|---|---|---|---|---|---|---|
| Polymer | 0.07 | 1.2 | 0.09 | 25 | 0.13 | 800 | - |
| Nanoparticles | 0.06 | 0.9 | - | - | - | - | 0.13 |

The subsequent decay of anisotropy over 500 ps for the polymer in THF occurs in three phases with time constants of 1.2 ps ($\tau_1$), 25 ps ($\tau_2$) and 800 ps ($\tau_3$). This appears to be at odds with data published previously by Nguyen *et al.* [148,149], where the first 50 ps of the anisotropy decay were fitted with time constants of ~1 ps and ~100 ps. However, fitting the first 50 ps of the data presented here yields the same time constants as those reported by Nguyen, which were assigned to intermolecular and intramolecular energy transfer, respectively. Intermolecular energy transfer concerns energy transfer

between different polymer molecules; however, it also includes energy transfer between two distant chromophores of the same polymer chain that are in close proximity as a result of the polymer conformation. In contrast, intramolecular energy transfer occurs between two adjacent covalently-linked chromophores. Alternatively, these can be considered as 'through space' and 'through bond' energy transfer, respectively. Interchain energy transfer is expected to be much faster as there are more potential acceptors surrounding the excited chromophore and therefore a greater probability of encountering a lower energy chromophore. There are only two possible acceptors for intramolecular energy transfer events, one on either side of the excited donor chromophore, and they are not necessarily of lower energy than the donor. It is important to note that an intramolecular energy transfer event may be followed by subsequent intermolecular energy transfer events, given the newly available acceptors. Therefore, the longer anisotropy decay component is assigned to energy transfer rate-limited by intramolecular energy transfer. The anisotropy decay data presented here suggests intramolecular rate-limited energy transfer is more rapid than previously reported for MEH-PPV, but is in reasonable agreement with the timescales reported for other conjugated polymers [19,136,140].

The nanoparticle anisotropy decay has only a single decay component corresponding to intermolecular energy transfer. This is to be expected given the compact nanoparticle structure with many potential acceptors surrounding the excited donor. Alternatively, the single phase decay of the nanoparticle anisotropy may be a result of the inhibition of torsional motions caused by the film-like packing of polymer chains within the nanoparticle. This can be further understood by performing simulations of energy transfer, detailed in the following section. Finally, the anisotropy decay of the

nanoparticles has a limiting anisotropy of 0.13 clearly visible after 5 ps, which suggests excitons are trapped before complete depolarisation occurs [150].

## 4.3 Energy Transfer Simulations

The MEH-PPV coarse-grained model, parameterised by Chiu *et al.* [151], was used to generate the polymer structures used in the energy transfer simulations. Briefly, there are three coarse-grained sites for each monomer unit corresponding to the centres of mass for the methoxy substituent (A), the phenylene vinylene moiety (B) and the ethylhexyloxy side chain (C), as shown in Figure 4.5. Similarly, there are corresponding coarse-grained sites D, E and F for monomers adjacent to a tetrahedral chemical defect. The radial distribution functions for bond lengths, bond angles, torsional angles and non-bonded interactions between these coarse-grained sites were parameterised using the iterative Boltzmann inversion method to match the equivalent interactions from atomistic simulations.

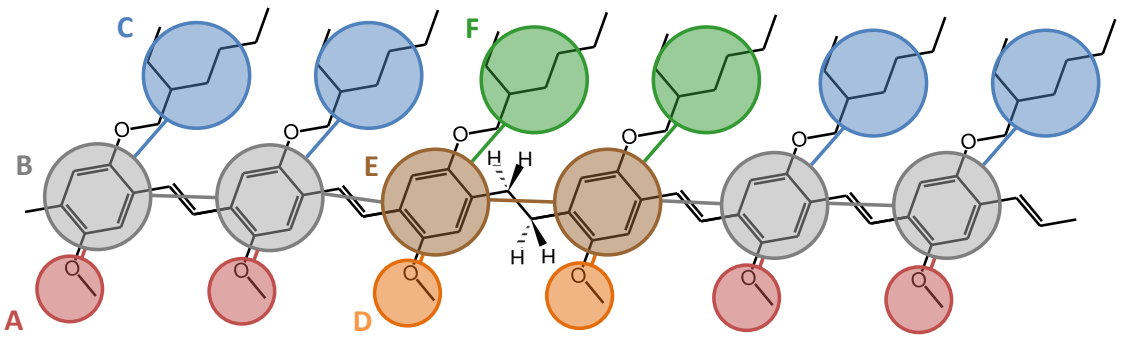


**Figure 4.5:** Coarse-grain scheme for a MEH-PPV segment containing a saturation defect.

All interactions, except the torsional angle distribution, were parameterised by 'optimised potentials for liquid simulation all atoms' force field calculations of MEH-

PPV monomers. Further consideration was given to the torsional angle distributions as these are expected to have the greatest influence on the polymer structure and are not well described by the same type of atomistic simulations. Therefore, only the bond rotation energy profile, determined by density functional theory at the B3LYP/6-31G* level, of the central bond of a MEH-PPV decamer was used to parameterise the torsional angle distribution. The resulting dihedral angle probability distributions between pristine (A-B-B-A) and defect adjacent monomers (D-E-E-D) are shown in Figure 4.6. The dihedral angle probability distribution of the pristine polymer shows the *syn* conformation, where the alkoxy side chains of adjacent monomers exist on the same side of the backbone, is preferred. The defect site has a similar probability of occupying a dihedral angle from 0° through 130° as a result of the greater flexibility compared to the pristine polymer. In both cases, the *anti* conformation is impeded by unfavourable steric interactions between the alkoxy side chain and the hydrogen atoms of the vinyl group [152].

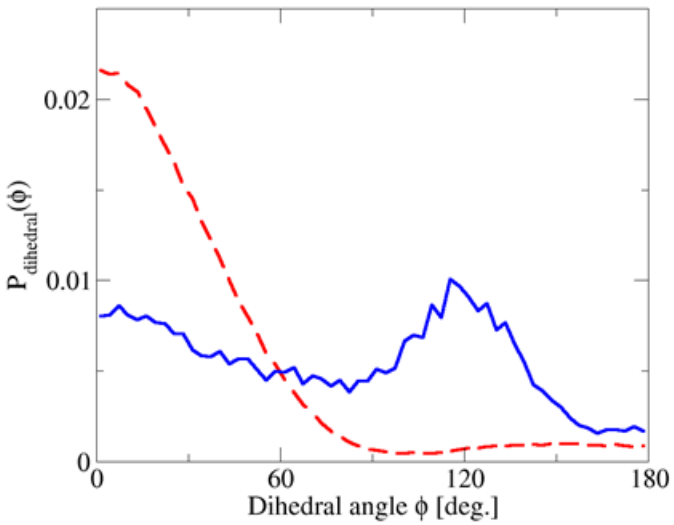


**Figure 4.6:** Dihedral angle probability distribution for the A-B-B-A (red) and D-E-E-D (blue) dihedral angles. From Ref. [151].

Molecular dynamics simulations were performed on single MEH-PPV chains containing 1000 monomers and a 10% defect concentration over several microseconds. This defect concentration was selected as it provided structures with a 41 nm radius of gyration, which is in good agreement with the experimentally determined 38.5 nm for MEH-PPV chains of this length in THF [153], assuming the ratio of the radius of gyration to hydrodynamic radius is ~1.3. Initially, the temperature of these simulations was set to 500 K to rapidly achieve equilibrium, then after 200 ns the temperature was reduced to 294 K. Snapshots of the molecular dynamics simulation trajectories were taken at equally spaced intervals once equilibrium had been established and were used as the polymer configurations for the energy transfer simulations. For atomistic simulations containing a few hundred monomers performed during the parameterisation steps, it is feasible to include solvent molecules; however, simulations on experimentally relevant polymer chain lengths of at least 1000 monomer units are not. Consequently, the solvent was treated implicitly using Langevin dynamics and tuning the nonbonded interactions to mimic the atomistic simulations in a good solvent. The

non-bonded interaction was then increased by a factor of 1.5, effectively reducing the solvent quality to replicate the conformation of the nanoparticle in aqueous suspension.

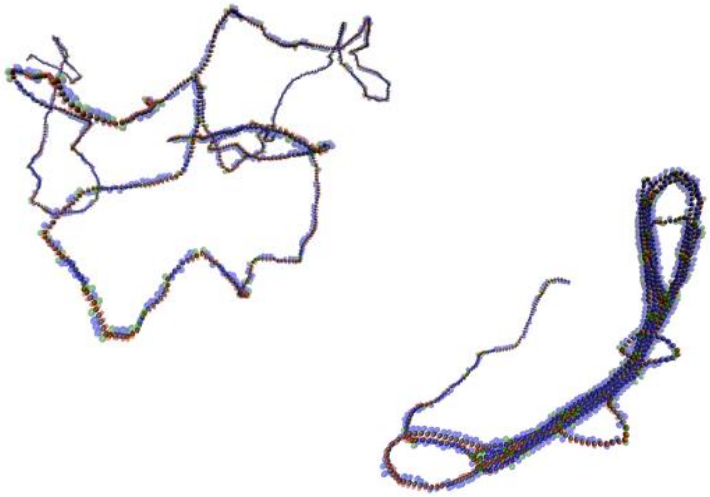

**Figure 4.7:** Snapshots of molecular dynamics simulations representative of a MEH-PPV chain in THF (left) and a MEH-PPV nanoparticle (right).

For the energy transfer simulations it was necessary to divide the polymer chain into chromophores. Chromophores were defined by the randomly positioned defect sites or by an inter-monomer dihedral angle of greater than 50°, which is considered to be the approximate angle at which conjugation is broken [154]. The resulting chromophores, shown in Figure 4.8, were then assigned an energy based on how many monomer units it contains. Both exponential [155,156] and hyperbolic [157,158] relationships between chromophore lengths and energies have been used previously. The hyperbolic function gave simulated anisotropies in better agreement with the experimental anisotropy decay despite the deviation from this relationship observed at longer chromophore lengths. Here, the chromophore energy ($E_i(n)$) is related to its length in monomer units ($n$) by

$$E_i(n) = \left(\frac{E_{i,1} - E_{i,\infty}}{n}\right) + E_{i,\infty} \qquad (4.1)$$

where $E_{i,\infty}$ is the energy of a chromophore containing more monomer units than the effective conjugation length and $E_{i,1}$ is the energy of the monomer [157]. The energy of the monomer was taken to be 3.5 eV, being the same as that reported for BEH-PPV [155]. Additionally, using the energies of MEH-PPV oligomers containing 3, 4 and 5 monomer units [159], $E_{i,\infty}$ was determined to be 2.30 eV, which agrees with the red-edge of the absorption spectrum.

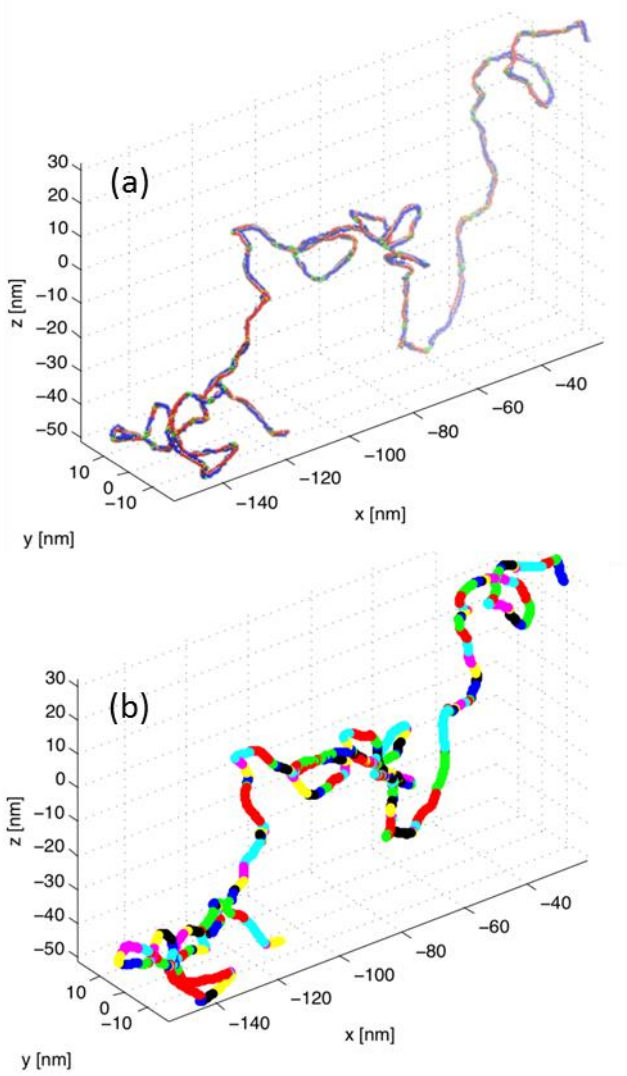


**Figure 4.8:** (a) A molecular dynamics simulation snapshot of a typical extended MEH-PPV configuration and (b) the same configuration segmented into chromophores. Each colour change indicates a break in conjugation and therefore the boundary of each chromophore.

The spectral overlap of the extinction coefficient and the area-normalised fluorescence spectra was determined for the polymer and nanoparticles. Homogenously broadened spectra were used as the inhomogenous broadening was already accounted for by the assignment of the chromophore energies according to Eq. (4.1). The distance and orientation of all possible energy transfer donor-acceptor pairs of the polymer configuration were used to calculate the corresponding energy transfer rates by Eq. (1.2). The orientation factor was determined using the line-dipole approximation, in

which the transition dipole moment is divided into sub-segments corresponding to each monomer unit. The angular displacement between all dipole moment sub-segments of the donor and acceptor were then calculated, the average of which was used to calculate the overall orientation factor for that donor-acceptor pair according to Eq. (1.3).

The initial exciton of the Monte Carlo energy transfer simulations was randomly positioned on a chromophore with energy equivalent to the excitation energy used for collecting the experimental data. The occupied chromophore lifetime, $t_0$, was given by

$$t_0 = -\frac{1}{w_i}\ln(1-x) \tag{4.2}$$

where $w_i$ is the overall depopulation rate of the chromophore and $x$ is a random number between 0 and 1. If the lifetime of the chromophore exceeds the rate of energy transfer, the exciton relaxes radiatively. Otherwise, energy transfer occurs and the process is repeated with another random number and a new set of possible energy transfer rates for the newly accessible acceptor chromophores.

This approach to energy transfer simulations differs from the reports summarised in the introduction to this chapter. Here, the simulations are performed on structures from molecular dynamics simulations of a physically accurate coarse-grained polymer model independent of the experimental data, whereas the earlier reports determine structural parameters from fitting the experimental data with the simulated anisotropy decay. The simulated anisotropy decays for the nanoparticles and the polymer in THF are shown in Figure 4.9. Each of the anisotropy decays was averaged from 1000 exciton hopping simulations on each of 200 polymer snapshots of the corresponding molecular dynamics simulation. These energy transfer simulations concerned only incoherent energy transfer events in the weak chromophore coupling regime and therefore the

initial anisotropy, which is a result of fast exciton localisation, was not considered. Thus, the simulated anisotropy decays were scaled to the same initial anisotropy value as the experimental data for direct comparison.

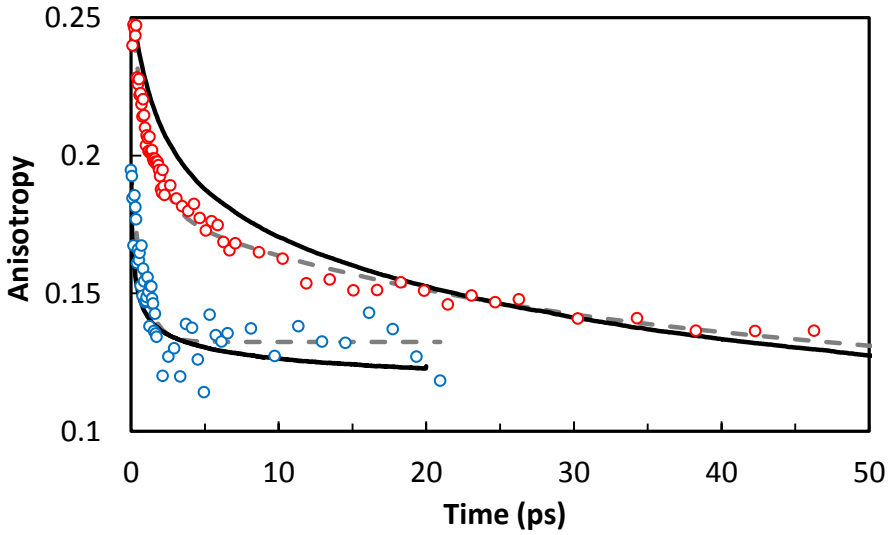


**Figure 4.9:** Comparison of simulated (solid lines) and experimental (circles) fluorescence anisotropy decays of the polymer (red) and nanoparticles (blue). The best fit of the experimental anisotropy decays are also shown (dashed lines).

The simulated anisotropy decay of the polymer in THF was fit with an exponential decay function with three time constants of 1.5 ps, 10 ps and 330 ps. These time constants are in good agreement with the experimentally determined time constants listed in Table 4.3. It is important to note that the values reported here for the longest time constants of the experimental and simulated data are not reliable as both well exceed the duration of their respective data sets. The simulated nanoparticle anisotropy decay was well described by a 0.6 ps major decay component and another minor 8 ps time constant. Other than this minor component, which is absent from the experimental data, there is good agreement between the experimental and simulated data indicating these polymer structures are representative of the true polymer conformations in each solvent environment. Furthermore, as the polymer configurations used here were static,

the effects of molecular motions including torsional relaxation are absent. Therefore, the second decay component of the experimental anisotropy decay of polymer in THF can be attributed to the energy transfer process.

Other parameters related to energy transfer were also determined using this model. For example, the exciton diffusion length calculated from the averaged mean squared displacement after the first 2 ps was $4 \pm 1$ nm in the polymer and $9 \pm 2$ nm in the nanoparticles, which are reasonable given the reported values for MEH-PPV solutions [8], films [160] and aqueous nanoparticle suspensions [161]. During these first 2 ps the extent of exciton diffusion is two orders of magnitude larger than expected. Without accounting for the localisation processes immediately following excitation, accurate estimates of the exciton diffusion length are not possible. Therefore, it is necessary to develop this model further. The approach of Barford *et al.* using the Frenkel-Holstein model, where the exciton is treated quantum mechanically and the polymer structure is treated classically, is one possible method [16,162]. The initial localisation of the quasi-extended exciton states immediately following excitation is also well captured by this model, which may resolve the discrepancy in the initial simulated and experimental anisotropy values. However, it has been suggested that a lack of interchain interactions in the polymer model may be problematic [162]. Therefore, the Frenkel exciton model combined with the physically realistic polymer structures from the coarse-grained molecular dynamics simulations described here should provide a more complete description of energy transfer. Although, despite our preliminary simulations using the Frenkel exciton model being unsuccessful in accurately reproducing the experimental anisotropy decay for MEH-PPV nanoparticles, it remains a focus of our group.

## 4.4 Conclusions

This chapter has shown the difference in energy transfer dynamics of MEH-PPV in well-solvated and compact nanoparticle environments. Isotropic fluorescence data for MEH-PPV in THF exhibited a ~1 ps decay component at higher emission energies indicating the corresponding chromophores are depopulated in favour of lower energy chromophores, which showed an initial growth in population. A similar trend was observed in MEH-PPV nanoparticles; however, this manifests a decrease in the rate of the initial decay component due to the shortened fluorescence lifetime. Energy transfer measured directly by time-resolved anisotropy experiments was found to occur on two time scales for the polymer solution corresponding to intermolecular and intramolecular energy transfer, while only the intermolecular type of energy transfer was observed in the nanoparticles. The anisotropy decay was simulated using the polymer structures from molecular dynamics simulations combined with other experimentally determined parameters and a Monte Carlo energy transfer algorithm. The reasonable agreement between the simulated and experimental anisotropy decays indicated these structures resemble the true polymer conformations. Additionally, the exciton diffusion lengths of the polymer and nanoparticles were approximately 4 nm and 9 nm, respectively.

# 5 Exciton and Hole-Polaron Dynamics in Composite P3HT/PCBM Nanoparticles

## 5.1 Introduction

Further to the applications in biological imaging [58-62], fluorescence sensing [68-70], organic photovoltaics [126-128] and electroluminescent devices [129,130] discussed in earlier chapters, conjugated polymer nanoparticles are also of interest as they provide an intermediate system between bulk films and single molecules. Therefore, studying these nanoparticles allows links between the bulk material functionality and molecular level properties to be understood. Recently, composite nanoparticles of regioregular poly(3-hexylthiophene-2,5-diyl) (rr-P3HT) containing the electron acceptor [6,6]-phenyl-C61 butyric acid methyl ester (PCBM), the structures of which are shown in Figure 5.1, have been prepared [74,77,78,85].

The P3HT/PCBM blend is the most extensively studied donor/acceptor combination. Device efficiencies of around 4% are routinely reported for this blend and efficiencies as high as 6.5% have been measured [163-165]. Other desirable properties of organic

donor/acceptor blends such as P3HT/PCBM include solution processability for fast and inexpensive device production using conventional printing techniques; however, this approach currently requires the use of hazardous organic solvents. Recently, there has been a trend toward using nonhazardous solvents including water for device preparation. Most of the work thus far involves using water soluble analogues of electron donor and acceptor materials [166,167]. An alternative and more straightforward route to achieving solution processability with water is to use aqueous suspensions of existing photovoltaic materials. Therefore, it is important to understand charge transfer and morphology in aqueous suspensions of these materials.

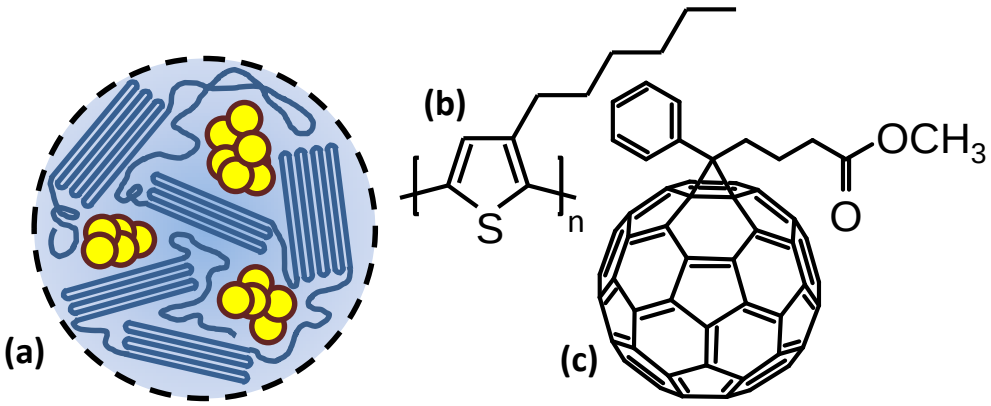


**Figure 5.1**: Illustration of a rr-P3HT nanoparticle containing PCBM aggregates (a) and the chemical structures of P3HT (b) and PCBM (c).

Although charge transfer has been demonstrated in aqueous suspensions of polymer/fullerene nanoparticles [73,75,78], the ultrafast dynamics of excited-state and charge-separated species have not been investigated. Such studies have been performed extensively on thin-film devices covering a wide range of film properties that influence the efficiency of charge separation [168-176]. In particular, the effects of polymer morphology and the influence of P3HT/PCBM doping ratios have been key areas of study. Transient absorption spectra of highly ordered rr-P3HT and amorphous

regiorandom P3HT (rra-P3HT) films both indicate formation of singlet excitons, polymer polarons, and charge-separated species [169,177], albeit in varying spectral regions. Charge separation, which is of particular interest, is found to follow a two-step mechanism in both film morphologies [169]. Initially, polarons are generated through charge separation of excitons at the P3HT/PCBM interface. Subsequently, a relatively slow formation of polarons occurs and this process is limited by exciton migration. The rate of the second phase of polaron formation is slow in rr-P3HT because excitons must migrate through extended semi-crystalline domains to undergo charge separation. Increasing electron acceptor concentration provides a greater interfacial area, which promotes charge separation immediately after excitation and enhances the probability for excitons to migrate to the PCBM interface successfully. Although these processes have been extensively studied in films, the excited state species and their associated dynamics have not been identified for aqueous dispersions of P3HT/PCBM nanoparticles. Additionally, a recent study of exciton-hole polaron interactions showed P3HT/PCBM composite nanoparticles have the ability to store photogenerated charges due to the presence of deep electron traps [85]. Studies of dynamics of P3HT excitons and other excited state species are important for an understanding of charge separation dynamics to offer insight into charge storage.

In this chapter, two key factors that influence the charge separation dynamics in aqueous suspensions of P3HT/PCBM nanoparticles are investigated, namely the regioregularity of P3HT and the concentration of PCBM. Steady-state fluorescence quenching studies show the relative charge transfer efficiency of nanoparticles with amorphous (rra-P3HT) and semi-crystalline (rr-P3HT) morphologies. Femtosecond transient absorption spectroscopy was then employed to identify various excited-state and charge-separated species in the visible and near-infrared spectral regions.

Formation and recombination dynamics of these species were also monitored to determine their dependence on electron acceptor concentration. By comparing the excited-state behaviour of P3HT/PCBM nanoparticles with studies of thin films, the performance of nanoparticles in a device-like environment was evaluated. The average size of semi-crystalline domains of rr-P3HT nanoparticles was then quantified using an exciton diffusion model for analysing transient absorption signals of P3HT/PCBM films [172]. The evolution of the transient absorption signals shows an excellent agreement with the exciton diffusion model for P3HT nanoparticles containing 5–50 wt% PCBM.

## 5.2 Fluorescence Quenching by Charge Transfer

Composite P3HT/PCBM nanoparticles were prepared using a slightly modified version of the method outlined in Chapter 2. A solution of PCBM was prepared in THF at a concentration of 1 mg/mL with the aid of sonication, a portion of which was then added to the polymer precursor solution to achieve the desired weight ratio. The absorption spectra of rr-P3HT nanoparticles doped with 0–50 wt% PCBM are shown in Figure 5.2. These spectra consist of three major bands, which include two UV absorption bands at 260 nm and 340 nm due to PCBM and the visible absorption at 500 nm due to the $\pi$-$\pi^*$ transition of the polymer. Aggregates of rr-P3HT with a high degree of order are known to form readily, which is evidenced by the vibronic structure present on the red side of the rr-P3HT nanoparticle absorption spectrum [178]. To better understand how the formation of semi-crystalline domains influences the structure within P3HT/PCBM nanoparticles, samples of PCBM-doped and undoped nanoparticles of rra-P3HT were also prepared. The vibronic structure in the undoped rr-P3HT nanoparticle spectrum is absent in the rra-P3HT nanoparticle absorption

spectrum. The absorption maximum of rra-P3HT is slightly red shifted compared to the absorption maximum of the polymer dissolved in THF, shown in Figure 5.2, where it adopts an extended conformation. In contrast, the absorption maximum for rr-P3HT is 30 nm to the red of the rra-P3HT absorption peak, which indicates a significant increase in the average chromophore length despite being subject to the same constraints of the nanoparticle structure [179]. This chromophore elongation is associated with the formation of H-aggregates, which exhibit significant interchain coupling of excitons, similar to that observed in thin films of rr-P3HT [180].

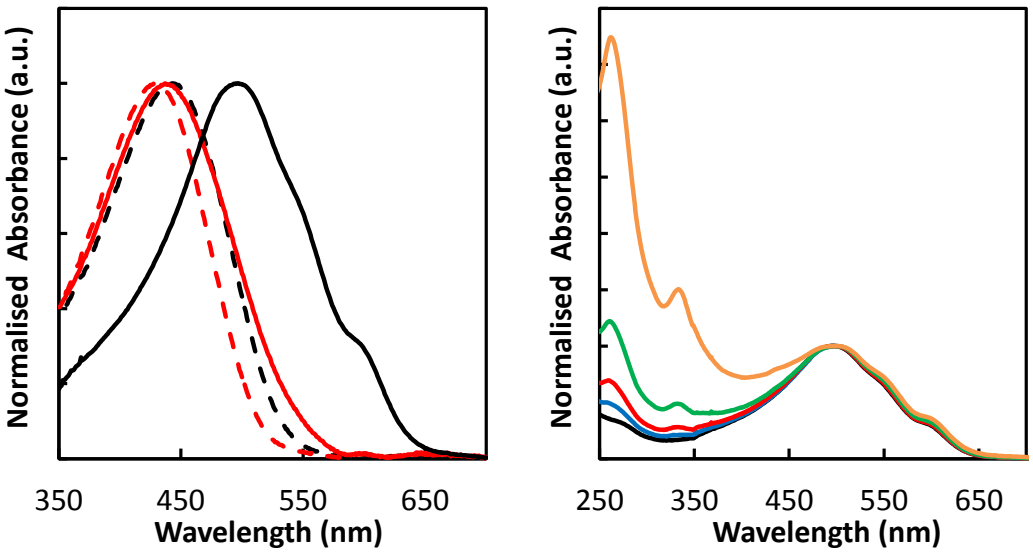


**Figure 5.2:** Left: Absorption spectra of rr-P3HT (black) and rra-P3HT (red) solution in THF (dashed) and nanoparticle suspensions in water (solid). Right: Normalised absorption spectra of rr-P3HT nanoparticles with 0 (black), 5 (blue), 10 (red), 20 (green) and 50 (orange) wt% PCBM.

Figure 5.3 shows the fluorescence maximum of rr-P3HT at 650 nm is substantially red shifted (55 nm) relative to rra-P3HT nanoparticles, which is a further indication that a longer average conjugation length is supported by the highly ordered structure within rr-P3HT nanoparticles. The amplitudes of the vibronic progressions in the fluorescence spectrum of rr-P3HT nanoparticles also reflect the presence of H-aggregates, as

observed in the absorption spectrum. The fluorescence intensity of rr-P3HT nanoparticles is quenched by the addition of PCBM but the shape of the fluorescence spectrum remains unchanged. These results are consistent with efficient charge transfer, as quenching of P3HT fluorescence by PCBM requires charge transfer to occur considerably faster than the exciton recombination lifetime [181]. Even at a high PCBM doping level of 50 wt%, a sizeable level fluorescence of rr-P3HT remains unquenched and it can be attributed to rr-P3HT excitons that are isolated from the PCBM interface. This result suggests that the formation of P3HT domains within rr-P3HT nanoparticles allows exciton recombination to occur before the exciton encounters any electron acceptor. Figure 5.3 also shows the fluorescence of rr-P3HT and rra-P3HT as a function of PCBM doping level. Quenching of fluorescence is significantly more efficient for rra-P3HT than rr-P3HT, which suggests that rra-P3HT nanoparticles possess a more homogeneous PCBM distribution and therefore a shorter average distance from excitation to P3HT/PCBM interface. While these data have not been corrected for any differences in the absorption cross-section at the excitation wavelength, each data set has been normalised to their respective undoped nanoparticle intensities. The measured fluorescence intensity of the undoped rra-P3HT nanoparticles is actually four times greater than the undoped rr-P3HT nanoparticles. As the quenching of rra-P3HT fluorescence with the addition of PCBM is much greater than that of rr-P3HT, the presence of crystalline domains with lengths comparable to the range of exciton diffusion is supported. Additionally, the error in the fluorescence intensities is less than ±5% for all samples.

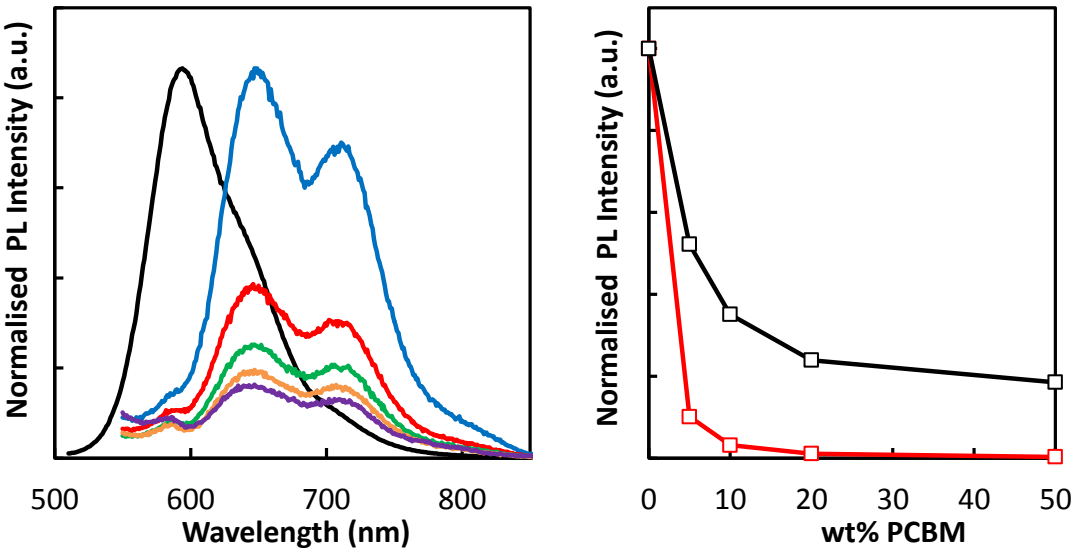


**Figure 5.3:** Left: Fluorescence spectra of undoped rra-P3HT nanoparticles (black) and rr-P3HT nanoparticles with 0 (blue), 5 (red), 10 (green), 20 (orange) and 50 (purple) wt% PCBM. Right: Normalised fluorescence intensity at the respective fluorescence maxima for rr-P3HT (black) and rra-P3HT (red) nanoparticles with the same PCBM concentrations.

The propensity for rr-P3HT to form large ordered semi-crystalline domains has a considerable effect on the efficiency of charge transfer in P3HT/PCBM nanoparticles. Formation of these domains constrains the regions available to PCBM within a nanoparticle, causing aggregation of PCBM within the nanoparticle. As a result, the available surface area of the P3HT/PCBM interface is limited relative to nanoparticles prepared with rra-P3HT, which is reflected by the fluorescence quenching data.

## 5.3 Charged and Excited State Species

Femtosecond transient absorption has been used routinely for investigating the formation of excited-state and charge-separated species in P3HT/PCBM films [169,172,173,177,182]. However, transient absorption has not yet been used to study

aqueous rr-P3HT nanoparticle suspensions containing PCBM. The transient absorption spectra of 0% and 50% PCBM doped rr-P3HT nanoparticles at various delay times are shown in Figure 5.4. The pump wavelength of 500 nm is known to excite both the amorphous and semi-crystalline domains of rr-P3HT aggregates. Immediately to the red of the pump wavelength, around 550 nm, the negative ΔA signal is assigned mainly to bleaching of the ground state as it occurs in the same spectral region as the ground state absorption spectrum. Although the ground state bleach gives information regarding the repopulation of the ground state after excitation, the ΔA signal in this wavelength region corresponds to a combination of processes including fluorescence, polaron recombination, and charge separation, making these data difficult to interpret. Instead, the excited-state absorption signals are used. For the undoped rr-P3HT nanoparticles there is an excited-state absorption band at 650 nm and another, much broader, absorption centred at 1250 nm. Previous studies on rr-P3HT films have shown that the two absorption signals at 650 nm and 1250 nm are attributable to polymer polaron pairs and singlet excitons, respectively [177].

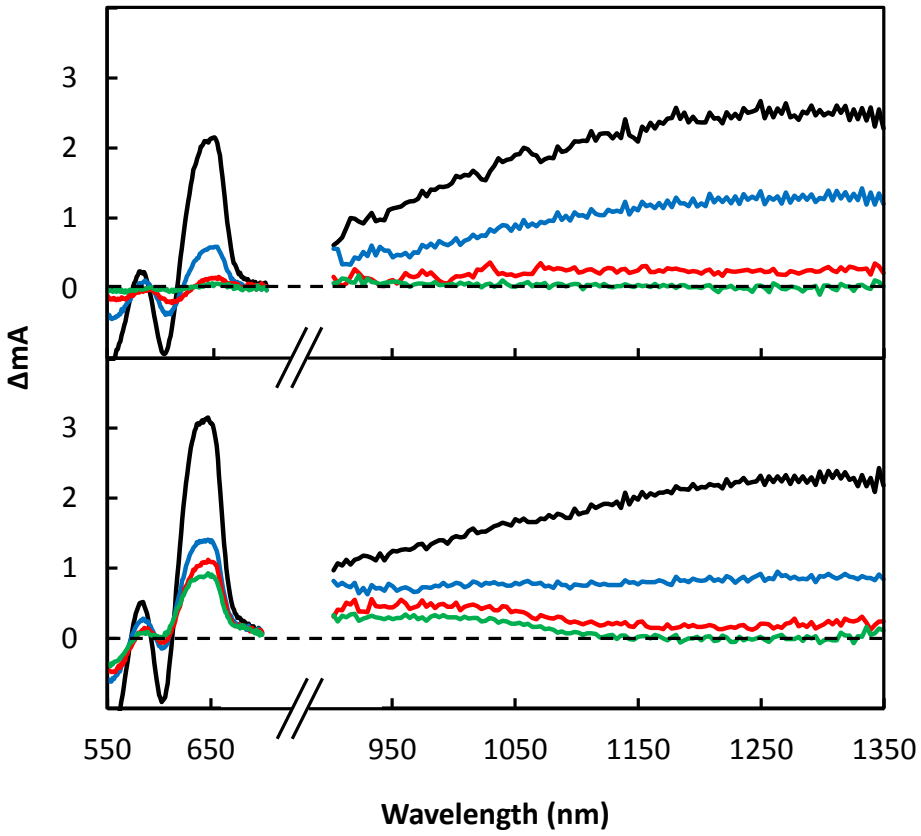


**Figure 5.4:** Transient absorption spectra of pure rr-P3HT nanoparticles (top) and rr-P3HT nanoparticles with 50-wt% PCBM (bottom) at 1 ps (black), 10 ps (blue), 100 ps (red) and 1000 ps (green) after excitation.

With the incorporation of PCBM into these nanoparticles, there are clearly fewer singlet excitons produced immediately following excitation, as shown in Figure 5.4. As the singlet exciton signal of the PCBM-doped nanoparticles diminishes, another excited-state absorption band within the singlet exciton band emerges around 1000 nm and persists for the entire measureable duration of these experiments. The long-lived absorption band at 1000 nm has been observed previously in film studies of rr-P3HT at higher pump intensities and has been assigned to the formation of hole-polarons [177]. The results presented here are consistent with this assignment. First, as this absorption band is absent in undoped P3HT nanoparticles at the excitation intensities used in these experiments, it must be promoted by inclusion of the electron acceptor. Additionally,

this excited-state absorption exhibits much slower decay, on the order of microseconds, compared to that observed for polymer polaron pairs [173,183,184]. Similarly, the excited-state absorption signal at 650 nm also becomes very long lived with the addition of PCBM. Both of these excited state absorption signals that remain after 1 ns are attributable to the formation of free charges. It is important to note that the 1000 nm signal contains the dynamics of both singlet exciton decay and free charge formation, which is discussed in more detail below.

Assignment of these various excited-state absorption signals can be further understood by examining the dynamics of each absorption band. Figure 5.5 shows the kinetic data for the excited-state absorptions at 1000 nm, and 1250 nm for rr-P3HT nanoparticles doped with 0–50 wt% PCBM. All data were fitted with the minimum number of exponential decay terms required to adequately represent the data. As the limit of the delay stage used for these experiments was 2.5 ns, full recombination dynamics were not captured. As a result, processes with lifetimes overly long to be accurately determined were fitted as constant value offsets.

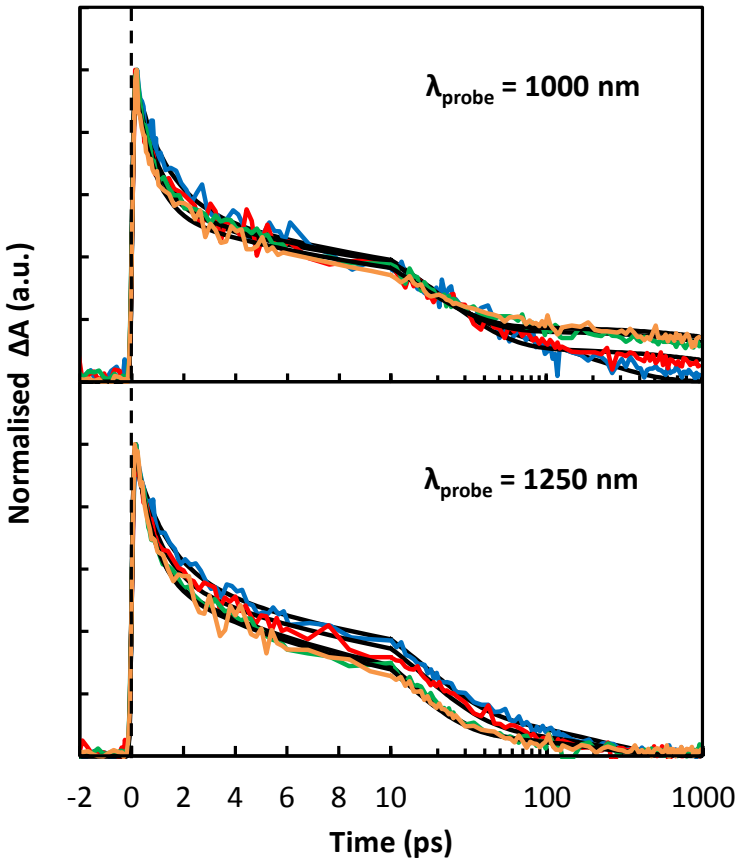


**Figure 5.5:** Kinetic traces at 1000 nm (top), and 1250 nm (bottom) for rr-P3HT nanoparticles doped with 0 (blue), 5 (red), 20 (green), and 50 (orange) wt% PCBM. The fitted curve for each sample is indicated by the corresponding solid black line. Note the change between linear and log scale at 10 ps.

A decrease in the time constant of the first ($\tau_1$) and second ($\tau_2$) fitting components of the 1000 nm excited-state absorption, listed in Table 5.1, as a function of PCBM doping level is due to the influence of the singlet exciton decay on the dynamics at this wavelength. The relative contribution of the third decay component increases with higher PCBM doping levels. The greater interfacial surface area at higher PCBM concentrations results in generation of more free charges that exhibit slow recombination dynamics.

**Table 5.1:** Fitted parameters for rr-P3HT/PCBM nanoparticles at 1000 nm

| PCBM (wt%) | $a_1$ | $\tau_1$ (ps) | $a_2$ | $\tau_2$ (ps) | $a_3$ | $\tau_3$ (ps) | $\langle\tau\rangle$ (ps) |
|---|---|---|---|---|---|---|---|
| 0 | 0.42 | 1.2 | 0.38 | 16 | 0.20 | 200 | 46 |
| 5 | 0.45 | 1.1 | 0.44 | 23 | 0.11 | 2300 | 260 |
| 20 | 0.46 | 0.7 | 0.39 | 16 | 0.15 | 4000 | 630 |
| 50 | 0.47 | 0.8 | 0.36 | 15 | 0.17 | 5000 | 860 |

Assignment of the 1250 nm photoinduced absorption to singlet excitons is supported by the fitting parameters shown in Table 5.2. The fraction of the fastest ~1 ps decay component ($\tau_1$) increases with increasing PCBM concentration, indicating quenching of singlet excitons through charge transfer. As mentioned earlier, this singlet exciton signal undergoes a substantial level of decay within 100 ps due to recombination, which confirms that no formation of free charges is observed at this wavelength. Furthermore, the power dependence on the singlet exciton recombination dynamics shown in Figure 5.6 indicates faster decay at higher excitation power, as would be expected for an increase in exciton–exciton annihilation.

**Table 5.2:** Fitted parameters for rr-P3HT/PCBM nanoparticles at 1250 nm

| PCBM (wt%) | $a_1$ | $\tau_1$ (ps) | $a_2$ | $\tau_2$ (ps) | $a_3$ | $\tau_3$ (ps) | $\langle\tau\rangle$ (ps) |
|---|---|---|---|---|---|---|---|
| 0 | 0.40 | 1.3 | 0.46 | 16 | 0.14 | 200 | 36 |
| 5 | 0.43 | 1 | 0.47 | 15 | 0.10 | 200 | 27 |
| 20 | 0.46 | 0.7 | 0.47 | 12 | 0.07 | 200 | 19 |
| 50 | 0.47 | 0.7 | 0.46 | 11 | 0.07 | 200 | 19 |

The decay of the pure P3HT nanoparticle singlet exciton band is significantly faster than the reported decay for annealed P3HT films. Similar to the dynamics of MEH-PPV nanoparticles in Chapter 4, the singlet exciton decay of rr-P3HT is described by three time constants of 1.3 ps, 16 ps and 200 ps, as shown in Table 5.2. The third component ($\tau_3$) was fixed at 200 ps corresponding to the fluorescence lifetime of P3HT [172]. The first component is assigned to energy transfer, while the second time constant is comparable to torsional relaxation, approximately 15 ps in P3HT films [185,186]. In contrast, the reported singlet exciton decay for annealed P3HT films is described by a single decay component corresponding to the fluorescence lifetime. Additionally, the crystallinity of these annealed films appears to suppress any torsional motion.

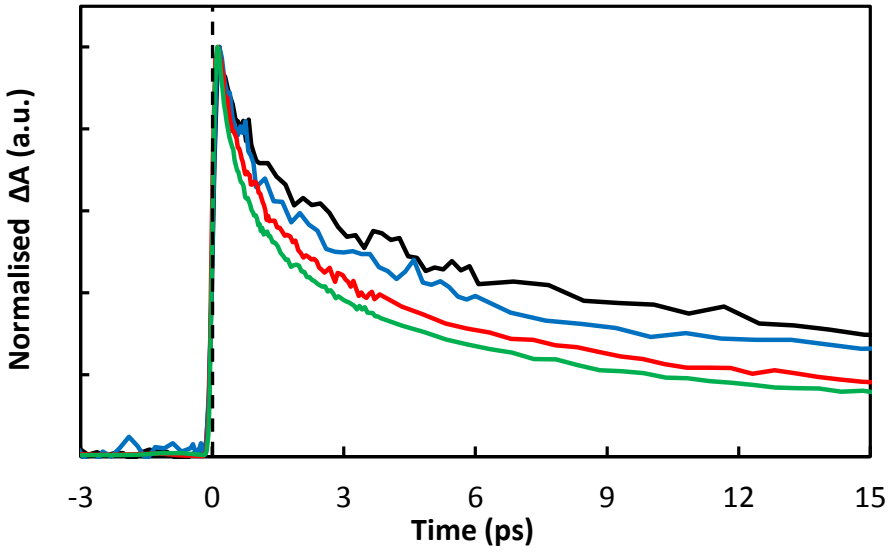


**Figure 5.6:** Decay of transient absorption signal at 1250 nm for rr-P3HT nanoparticles at 50 (black), 150 (blue), 260 (red) and 460 (green) nJ/pulse.

## 5.4 Diffusion Model

The one-dimensional diffusion model of Kirkpatrick *et al.* [172], was used to analyse the 1000 nm transient absorption signal, shown in Figure 5.7. Briefly, the model describes the competition between charge transfer and exciton decay for a P3HT domain bounded by PCBM. Excitons within P3HT decay according to the excited state lifetime ($\tau_r$). If excitons reach the P3HT/PCBM interface during this time, they form a charge transfer state. In this model, the exciton population $\xi(t)$ per absorbed photon varies with time according to

$$\xi(t) = \sum_{n_{\text{odd}}} \frac{8}{\pi^2 n^2} \exp\left[-\left(\frac{\pi^2 n^2 D}{L^2} + \frac{1}{\tau_{\text{r}}}\right) t\right], \tag{5.1}$$

where $L$ is the P3HT domain size and $D$ is the exciton diffusion constant in P3HT, which is related to the exciton diffusion length $L_{\text{ex}}$ by $L_{\text{ex}} = \sqrt{D\tau_{\text{r}}}$. To account for the multiexponential and considerably faster exciton decay in nanoparticles compared with films, the model was altered to include two exciton recombination time constants, $\tau_{r_1}$ and $\tau_{r_2}$, giving the following modified equation for the exciton population

$$\begin{aligned} \xi(t) = a_1 \sum_{n_{\text{odd}}} \frac{8}{\pi^2 n^2} \exp\left[-\left(\frac{\pi^2 n^2 D}{L^2} + \frac{1}{\tau_{r_1}}\right) t\right] \\ + a_2 \sum_{n_{\text{odd}}} \frac{8}{\pi^2 n^2} \exp\left[-\left(\frac{\pi^2 n^2 D}{L^2} + \frac{1}{\tau_{r_2}}\right) t\right] \end{aligned} \tag{5.2}$$

where the relative amplitudes $a_1$ and $a_2$ were determined from the pure P3HT nanoparticle decay and were held constant for all concentrations of PCBM. The equations in the model for the polaron population and transient absorbance were modified accordingly to account for the additional relaxation time. The instantaneous rate of charge generation depends on the exciton population that can migrate

successfully to the interface. Once the charge transfer state is formed it can undergo either geminate or bimolecular recombination. It has been proposed that geminate recombination can potentially follow either exponential or power-law decay at short times depending on the level of disorder in P3HT and the concentration of the electron acceptor [172]. In both cases, geminate recombination is followed by bimolecular recombination, which is represented by a power-law decay. For exponential geminate recombination the polaron population $p(t)$ at time $t$ per exciton dissociated at time zero in the model is given by

$$p(t) = exp\left(\frac{-\tau_{\mathrm{b}}}{\tau_{\mathrm{g}}}\right) exp\left(\frac{{\tau_{\mathrm{b}}}^2}{t\tau_{\mathrm{g}} + \tau_{\mathrm{b}}\tau_{\mathrm{g}}}\right)\left(1 + \frac{t}{\tau_b}\right)^{-\alpha}. \qquad (5.3)$$

This geminate recombination model gave the best description of the data and was used to fit all transient absorption decays presented here. In this case, the proportion of charges that undergo bimolecular recombination, which is given by the first term in Eq. (5.3), depends on the time constant of geminate recombination ($\tau_{\mathrm{g}}$) and charge separation ($\tau_b$). Charges that overcome the Coulombic binding energy successfully to form free charges will recombine according to the power-law decay term with an exponent, $\alpha$. Convolving the rate of charge generation with the temporal evolution of the generated charge pairs gives the total charge population. Finally, the transient absorption signal can be calculated as the sum of exciton and charge populations while considering the relative extinction coefficient ($\varepsilon_{rel}$) of excitons and hole-polarons at 1000 nm.

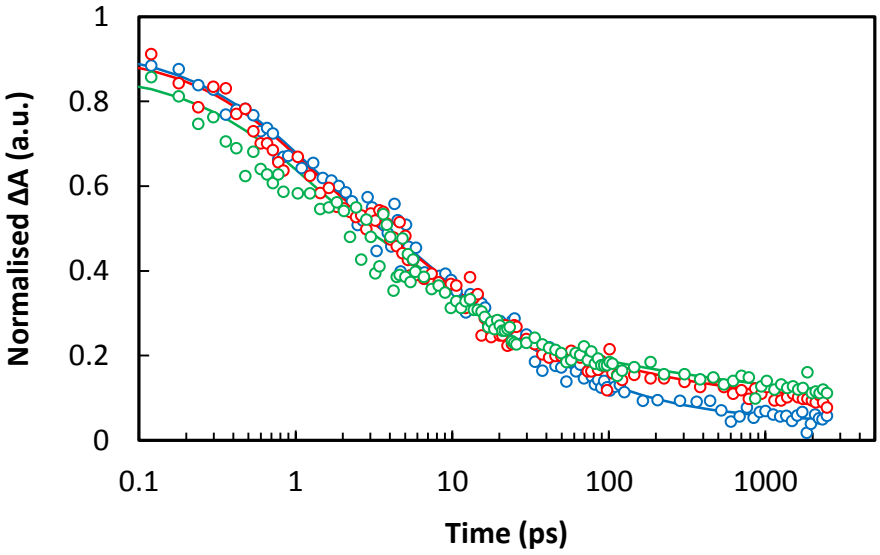


**Figure 5.7:** Decay of transient absorption signal at 1000 nm for 5 (blue), 20 (red) and 50 (green), wt% PCBM. The corresponding fits from the exciton diffusion model are shown as solid lines.

The transient absorption data at 1000 nm, shown in Figure 5.7, were fitted with this model. In the analysis, the values of $\tau_{r_1}$ and $\tau_{r_2}$ were fixed at 1 ps and 15 ps, respectively, for all PCBM concentrations. These values are consistent with the first two decay time constants of the exciton dynamics, which are inferred from the transient absorption signal at 1250 nm. The values of $\tau_b$ and $\alpha$ were fixed at 100 ps and 0.11, respectively, since these parameters are properties mainly of the bulk phases and should therefore not be substantially affected by variations in the PCBM concentration [172]. The magnitude of the power-law decay exponent $\alpha$ indicates the quantity of deep trap states in P3HT films, with higher exponents indicating fewer trap states [168]. The power-law decay observed in composite P3HT/PCBM nanoparticles occurs more rapidly than that observed for films, indicating that fewer trap states form during nanoparticle preparation. The relative extinction coefficient of exciton and free charges at 1000 nm were taken to be unity and 0.8, respectively, and were held constant across

all PCBM concentrations [172]. The average P3HT domain length and geminate recombination time constant were obtained by fitting each transient absorption decay with the model. The best fit parameters are shown in Table 5.3.

**Table 5.3:** Fitted parameters from diffusion model for 1000 nm transient absorption decay data

| **PCBM wt%** | ***L* (nm)** | **$\tau_g$ (ps)** |
|---|---|---|
| 5 | 4.8 ± 2.0 | 67 ± 25 |
| 20 | 5.6 ± 1.5 | 170 ± 80 |
| 50 | 5.6 ± 1.5 | 260 ± 190 |

The average P3HT domain length is consistent across the range of PCBM concentrations studied here given the degree of uncertainty present in the data. These results are comparable to the length of P3HT domains in films and show good agreement with annealed films of high PCBM concentration.[172] Such agreement is interesting as it suggests the vastly different preparation conditions yield similarly ordered polymer domains. Additionally, from the AFM data shown in Figure 5.8, the nanoparticles are only 6–11 times larger than the P3HT domain length, depending on PCBM concentration, but behave similarly to the bulk materials despite the high surface-to-volume ratio.

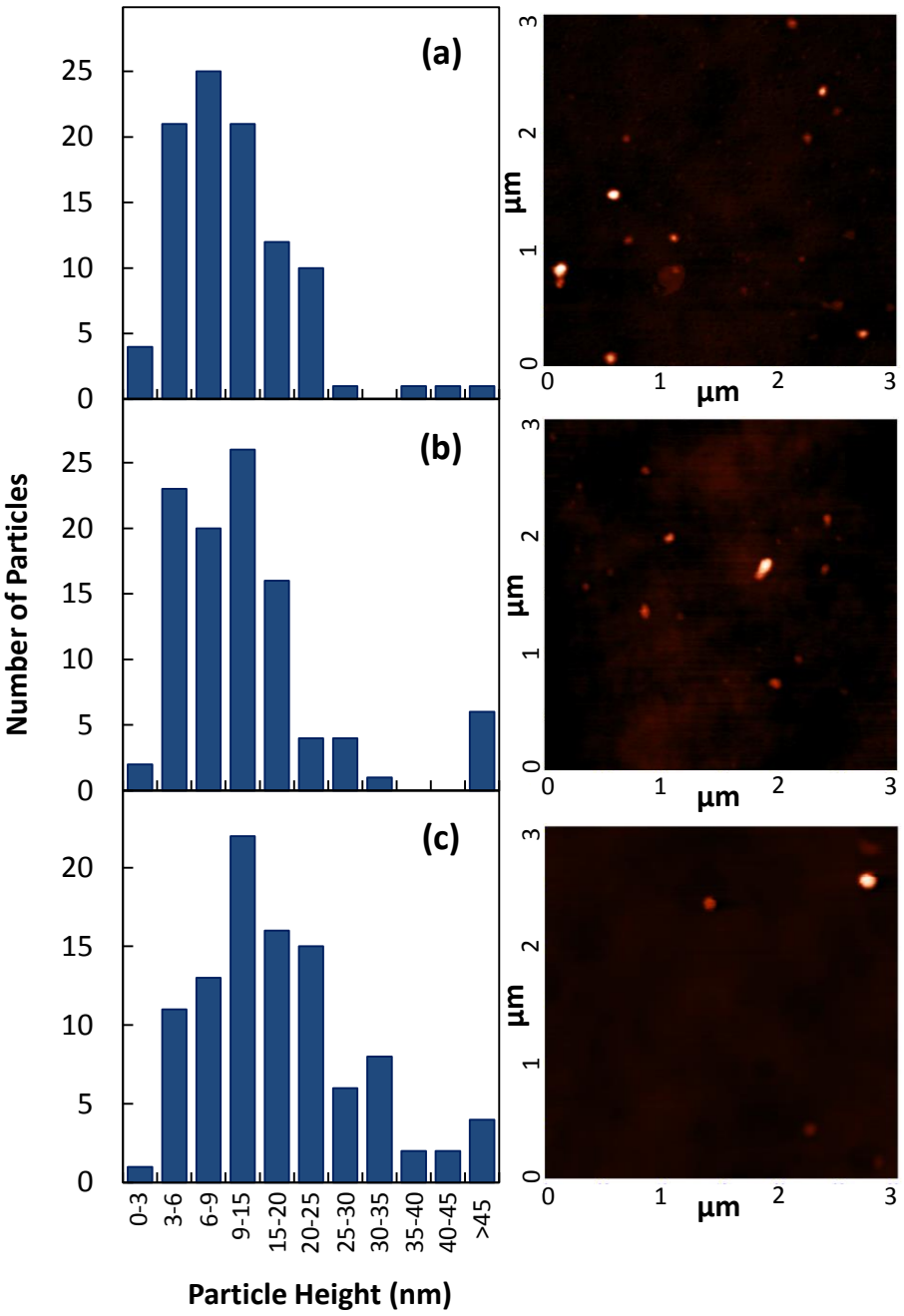


**Figure 5.8:** AFM particle height distributions and example images for rr-P3HT nanoparticles containing (a) 0wt%, (b) 5 wt% and (c) 50 wt% PCBM.

The size of PCBM aggregates for each PCBM concentration was calculated by assuming a homogeneous distribution of spherical and equally sized PCBM aggregates. As several reports have shown PCBM forms needle-like aggregates in annealed films [175,187], it is necessary to make this assumption given this model only yields one

length dimension. Therefore no information regarding the shape of these PCBM aggregates can be deduced from this model. For this calculation, the volume fractions of PCBM were determined from the PCBM doping ratio and the densities of crystalline P3HT and crystalline PCBM, which were 1.12 g/cm$^3$ and 1.67 g/cm$^3$, respectively [188,189]. The resulting diameters were found to be 3.2 nm, 10.4 nm, and 60.5 nm for 5, 20, and 50 wt% PCBM, respectively. The diameter of PCBM aggregates in the 50-wt% PCBM sample is unreliable as the assumption of equally sized and homogeneously distributed PCBM aggregates is inadequate when the PCBM content becomes a large fraction of the total nanoparticle mass.

As mentioned above, the power-law decay observed in composite P3HT/PCBM nanoparticles has an $\alpha$ value of 0.11 and occurs more rapidly than that observed for films where $\alpha$ = 0.05. This result suggests fewer trap states are formed in the nanoparticles than in rr-P3HT films. It is well known that deep traps are facilitated by large highly crystalline domains with the grain boundaries surrounding the domains capable of trapping charges [190]. Therefore, the presence of fewer deep trap states in these nanoparticles suggests there are fewer grain boundaries surrounding the crystalline domains compared to films.

From the exciton diffusion model, it is also possible to determine the geminate recombination time constant and the proportion of charges that recombine through geminate and bimolecular recombination [172]. The geminate recombination time constant increases from 67 ps to 260 ps as the PCBM concentration increases from 5–50wt% PCBM. These $\tau_g$ values indicate that the proportion of charges that undergo bimolecular recombination are 22%, 56% and 68% for 5, 20 and 50 wt% PCBM, respectively, for a fixed $\tau_b$ value of 100 ps. At PCBM concentrations of 10 wt% and

below, charges recombine predominantly by geminate recombination, whereas at higher concentrations bimolecular recombination is the primary mechanism. The likely cause for the increase in the geminate recombination time constant as a function of PCBM concentration is the formation of larger PCBM aggregates as demonstrated by the estimates mentioned earlier. Larger aggregates of PCBM allow effective migration of charge pairs, thereby reducing the probability of geminate recombination. Considering the observed trend in the geminate recombination time constant it is likely that increasing the PCBM concentration causes the aggregates of PCBM in the nanoparticle to become larger rather than forming a greater number of relatively small aggregates, which is in agreement with the PCBM aggregate sizes calculated from the model.

## 5.5 Conclusions

This chapter presented steady-state and transient optical spectroscopic data concerning charge transfer in P3HT/PCBM composite nanoparticles. Steady-state absorption and fluorescence quenching data show vastly contrasting behaviour between nanoparticles prepared with rr-P3HT and rra-P3HT. The rr-P3HT/PCBM nanoparticles contain extended semi-crystalline domains of P3HT that confine PCBM to aggregates, while amorphous nanoparticles of rra-P3HT exhibit a more homogenous distribution of PCBM. Excited-state and charge-transfer species in rr-P3HT/PCBM composite nanoparticles were identified using visible pump and visible/near-infrared probe femtosecond transient absorption spectroscopy. The signals at 650 nm, 1000 nm, and 1250 nm were assigned to polymer polarons, hole-polarons, and singlet excitons, respectively, which show good agreement with previous studies on films. The 1000 nm signal, which includes contributions from both singlet exciton decay and free charge

formation, was fitted to a one-dimensional diffusion model to determine the size of the P3HT domains and the rate of geminate recombination. The size of P3HT domains does not show any significant variation across the range of PCBM concentration studied here. Geminate recombination is the dominant mechanism at low electron acceptor concentrations, while at high PCBM concentrations bimolecular recombination is favoured. The increase in bimolecular recombination with PCBM concentration is likely to be caused by the formation of larger PCBM aggregates rather than a greater number of small aggregates, as in that case charges are less likely to be confined by the size or shape of the PCBM aggregates. The results presented here are in good agreement with studies on rr-P3HT/PCBM films, which confirm that these composite nanoparticles are suitable model systems for polymer bulk heterojunction devices.

# 6 Transient Absorption Spectroscopy of P3HT Nanowires

## 6.1 Introduction

As discussed earlier, the crucial role of polymer nanostructure in device performance is well known [191-193]. Highly efficient devices containing a P3HT/PCBM blend are often prepared by thermal annealing, which enhances the hole mobility by three orders of magnitude to ~$2\times10^{-8}$ $m^2V^{-1}s^{-1}$ due to the greater crystallinity of the P3HT regions [40]. However, when cast in blend films the growth of the crystalline regions within the film can be restricted. Recently, there has been a shift towards production of ordered nanowire structures prior to film casting [45,46,194-196]. These nanowires are conveniently prepared by the whisker method, originally reported by Ihn *et al.* for alkyl-substituted polythiophenes [44], whereby the polymer is dissolved in a marginal solvent at elevated temperatures followed by gentle cooling, which induces crystallisation of the polymer. Unlike thermally annealed blend films, the crystallisation

of the polymer is not hindered by the presence of an electron acceptor and can therefore extend over greater distances.

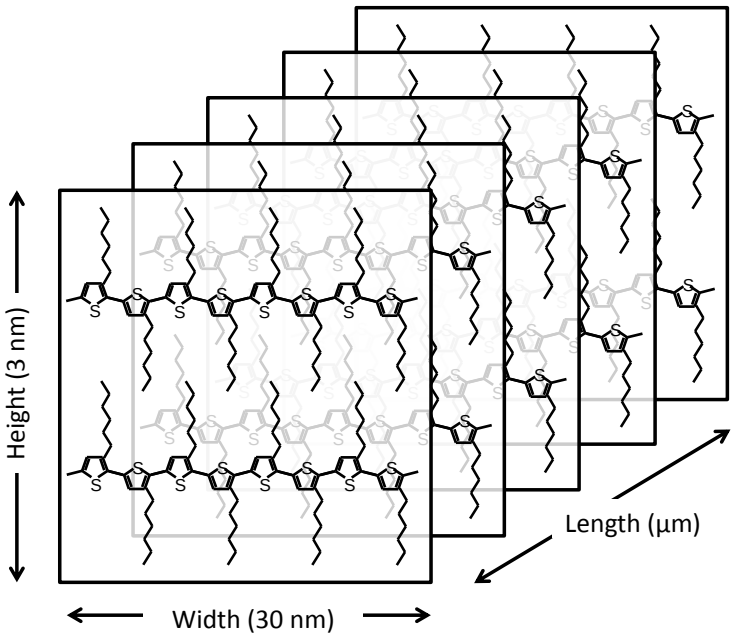


**Figure 6.1:** Structure of rr-P3HT nanowires in anisole with approximate dimensions. Adapted from Ref. [197].

The degree of crystallinity in polythiophene nanowires is governed by several related factors including the cooling rate and choice of solvent [87,198]. These parameters are selected to crystallise the polymer as gently as possible allowing the polymer chains to sample many configurations before becoming fixed. Therefore, slow cooling rates (~20°C/hr) and reasonably good solvents, such as toluene and *p*-xylene, are often used to produce highly ordered nanowires. Anisole has also been used, with the added benefit of relatively few amorphous impurities compared to nanowires prepared in other solvents [199,200]. Typically, nanowires of P3HT prepared in anisole have cross sections of 3 nm × 30 nm and extend to several microns in length [87,196,198], as shown in Figure 6.1. The shortest axis of the nanowire is defined by two or three polymer backbones separated by the alkyl side chains, while the intermediate axis

indicates direction of the polymer repeat units. The longest dimension corresponds to the π-stacking of thousands of segments with a spacing of 3.8 Å between adjacent polymer backbones [198]. This length dimension has been shown to depend on the rate of cooling with shorter nanowires, on the order of 100 nm, produced in rapidly cooled solutions [87]. Additionally, high regioregularity and large molecular weights are necessary to form structures with long range order [87,201,202].

Several studies have investigated the photovoltaic performance of devices containing nanowires with reported efficiencies around 3% without further treatment [194-196]. This can be enhanced beyond 4% by thermal annealing, achieving a greater efficiency than comparable thermally annealed devices without pre-formed nanowires [45,46]. The improvement is attributed to the division of polymer crystallisation and donor-acceptor phase separation into two distinct steps, traditionally achieved simultaneously by thermal annealing. Furthermore, the influence of nanowire ageing time and annealing temperature on these two steps has been reported [194]. The optimal temperature for annealing these devices is lower than the annealing temperature used for traditional bulk heterojunction devices, as annealing is only necessary for phase separation.

More recently, a study by Martin *et al.* [203] examined the effect of polymer order on the generation and recombination of polarons in nanowires by femtosecond transient absorption spectroscopy. This study demonstrated the greater order of J-type nanowires results in slower recombination of delocalised polarons, indicating greater intrachain coupling. The greater order also decreases the yield of delocalised polarons. This was attributed to the reduced interfacial surface area between amorphous and crystalline domains, which is the site of polaron formation [204]. Another study by Kurniawan *et*

*al.* [47], which investigated a broader time window, concluded that there is an increase in bimolecular recombination in nanowire devices compared to conventional thermally annealed devices. This was attributed to directional charge transfer along the long nanowire axis, which is typically oriented parallel to the electrodes. Charge transport between adjacent nanowires is relatively poor, reducing the charge transport in the direction of the electrode; a finding which has since been supported by a time-resolved fluorescence study of isolated nanowires at the single molecule level [205].

In this chapter, the relationship between polymer nanostructure and exciton diffusion length is explored. The degree of crystallinity in nanoparticles and nanowires was quantified by the excitonic coupling from steady state absorption spectra. Pump-probe and pump- push -probe femtosecond transient absorption spectroscopies were then used to examine the excited state behaviour of these nanowires. The excitation power dependence of the pump-probe singlet exciton signal was then used to estimate the exciton diffusion length using two published models for the nanoparticles and nanowires. The data presented here provide further insights into to the development of nanoparticles and nanowires for incorporation into bulk heterojunction devices.

## 6.2 Preparation of Nanoparticles and Nanowires

The methods for nanoparticle and nanowire preparation are described in Chapter 2. The nanowire dimensions reported previously by our group [206] were approximately 50 nm in width and greater than a micron in length, showing good agreement with earlier reports [87,198]. The absorption spectrum of nanowires prepared in anisole, shown in Figure 6.2, exhibits vibronic bands with greater amplitudes than rr-P3HT

nanoparticles. The excitonic coupling ($J_0$) is a convenient measure of the order in each nanostructure. It is calculated from the relative absorbance of the 0–0 and 0–1 vibronic transitions ($A_{0-0}$) and ($A_{0-1}$), respectively, according to

$$\frac{A_{0-0}}{A_{0-1}} = \left( \frac{1 - \frac{0.48 J_0}{E_p}}{1 + \frac{0.146 J_0}{E_p}} \right)^2 \tag{6.1}$$

where $E_p$ is the energetic separation of the vibronic transitions, which is 0.18 eV [24,200]. The absorbance at 610 nm and 560 nm, corresponding to the 0–0 and 0–1 vibronic transitions were 0.77 and 0.43, respectively. Therefore, the excitonic coupling is 78 meV; this is comparable to that previously reported for nanowires prepared in anisole and annealed films. Centrifuging the nanowires provides only a modest improvement in the overall crystallinity of the samples due to the relatively small fraction of amorphous aggregates produced by the whisker method in anisole [198]. The absorption spectrum of the rr-P3HT nanoparticles also shows this vibronic structure, albeit much weaker than the nanowires. This is reflected by an excitonic coupling of 106 meV, indicating less order compared to the nanowire structure.

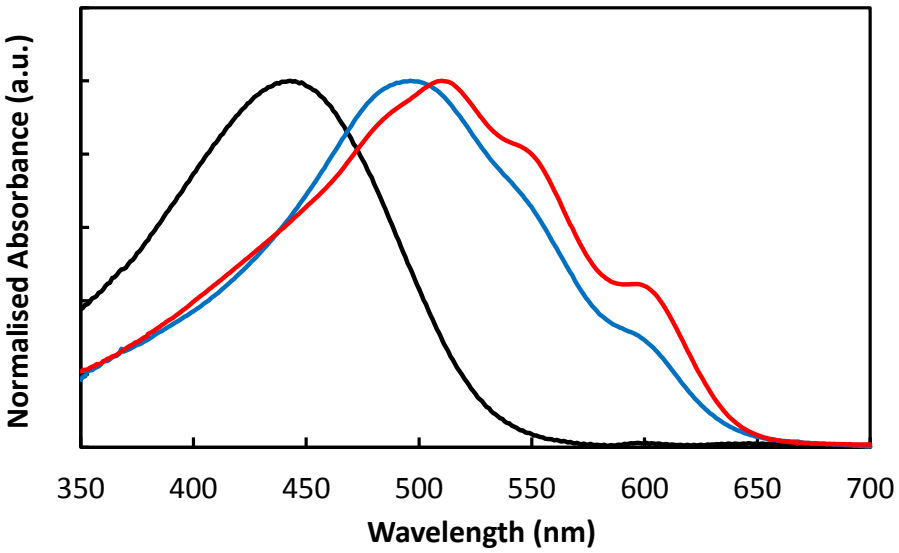


**Figure 6.2:** Absorption spectra of rr-P3HT in THF (black), rr-P3HT nanoparticles (blue) and rr-P3HT nanowires in anisole (red).

## 6.3 Two and Three Pulse Transient Absorption Spectroscopy of Nanowires

The transient absorption spectra of nanowires and nanoparticles pumped at 400 nm with low excitation densities, shown in Figure 6.3, have features similar to those described in Chapter 5. The nanowire ground state bleach shows two peaks at 560 nm and 610 nm corresponding to the 0–1 and 0–0 vibronic transitions, respectively. The third peak at 510 nm, with a shoulder at 480 nm, contains contributions from both the amorphous and crystalline regions of the nanowire [31,207]. The photoinduced absorption at 650 nm is assigned to polymer polarons, as reported in Chapter 5 and in the literature [84,177]. The main differences between the nanowire and nanoparticle spectra are the amplitudes of the vibronic transitions in the ground state bleach, which are a reflection of the steady state absorption spectra. Additionally, the polaron decay

appears to be much more rapid for the nanowires indicating fewer trap states or grain boundaries between the amorphous and crystalline regions [203,204]. Although this result seemingly disagrees with comparisons between nanoparticles and annealed films in the previous chapter, it is to be expected given the greater overall order of the nanowires.

Also shown in Figure 6.3 is the rise of the singlet exciton absorption signal at 1200 nm for pump wavelengths of 400 nm and 600 nm, respectively, corresponding to the amorphous and crystalline regions of the nanowire sample. The slower rise (~1 ps) is also observed following excitation with the 400 nm pump; however, when pumped at 600 nm this singlet exciton absorption exhibits an instrument response limited rise (~270 fs), indicating the crystalline domains are excited directly. Interestingly, the nanoparticle data showed an instrument response limited rise for all pump and probe wavelength combinations, which can be attributed to the reduced solubility of P3HT in water compared to anisole. Molecular dynamics simulations of nanowire aggregation have shown sections of the polymer chain are not incorporated into the nanowire structure but rather exposed to the solvent, resulting in well-solvated polymer segments [208]. For these segments, the rate of energy transfer to the lower energy crystalline regions would be limited by the greater average distance between the solvated segments and aggregates. Whereas for the nanoparticles dispersed in water, an exceedingly poor solvent, the amorphous polymer segments would be forced to collapse onto the particle surface, rather than extending away from it. Therefore, energy transfer from the amorphous to crystalline regions is expected to be faster in the nanoparticle sample compared to the nanowires.

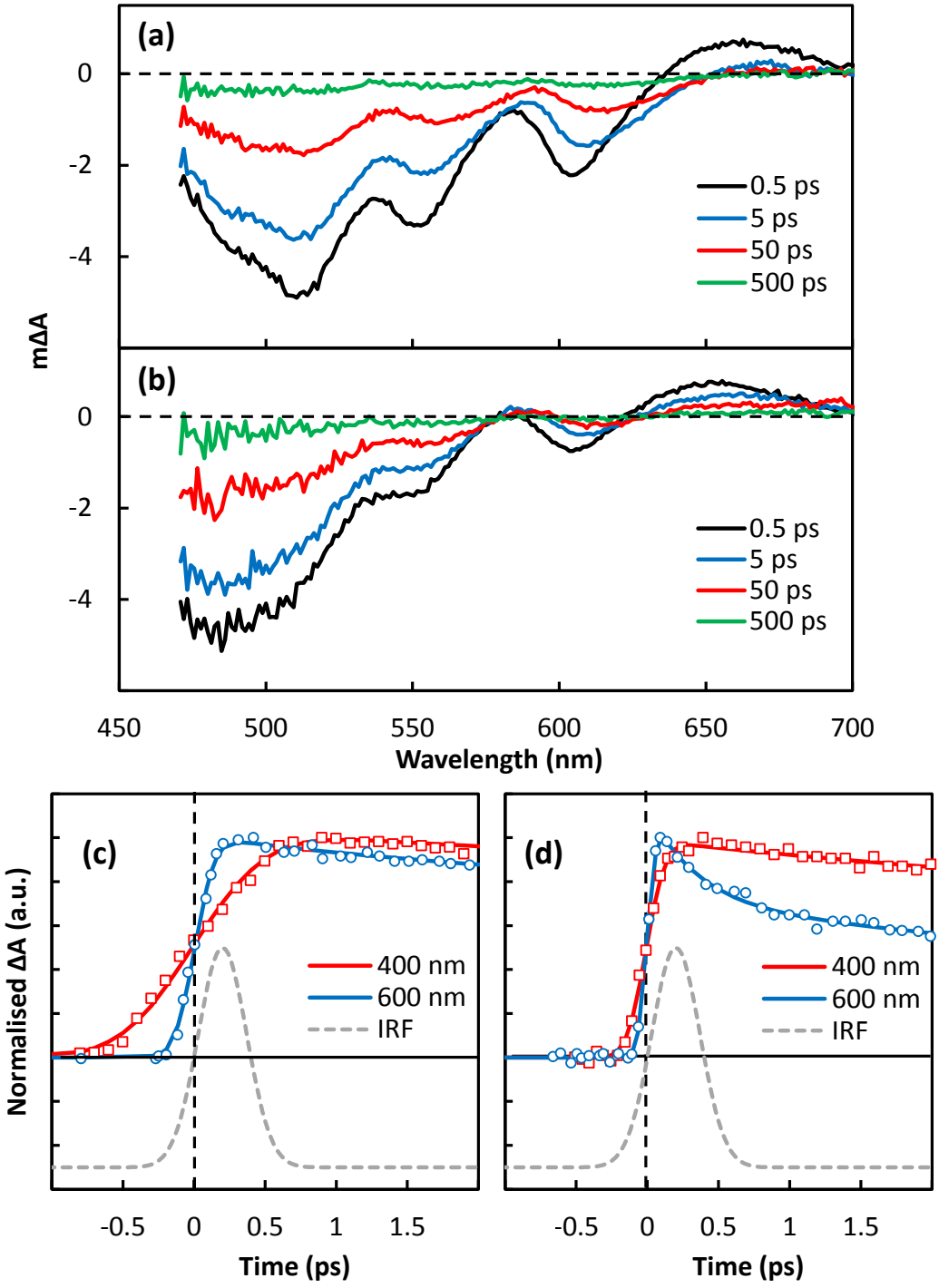


**Figure 6.3:** Transient absorption spectra of rr-P3HT nanowires (a) and nanoparticles (b) at 0.5 ps (black), 5 ps (blue), 50 ps (red) and 500 ps (green) after excitation. Dynamics of the singlet exciton absorption probed at 1200 nm with pump wavelengths of 400 nm (red) and 600 nm (blue) for P3HT nanowires (c) and P3HT nanoparticles (d). The instrument response function of the 400 nm pump pulse (~270 fs) is shown for comparison (grey).

The transient absorption spectra at 3 ps after excitation for the nanowires pumped at 400 nm and 600 nm with comparatively low excitation densities are shown in the top panel of Figure 6.4. Excitation at 400 nm shows an increased absorption at the higher energy side of the absorption band, which can be at least partially attributed to the generation of polarons known to occur for above band-gap excitation of P3HT films [169]. Alternatively, the absorption of excitons trapped in well-solvated amorphous segments isolated from crystalline domains could contribute to this absorption.

Increasing the excitation density of the pump light shows a shift to higher energy for the exciton absorption; this is observed for both pump wavelengths. The data for 400 nm excitation is shown in the bottom panel of Figure 6.4. Above an excitation density of $3.8\times10^{18}$ $cm^{-3}$ for the above-gap excitation, the peak position remains at ~1050 nm, which corresponds to the absorption of excitons in THF solutions of P3HT. This suggests exciton annihilation occurs more readily in the crystalline phase leaving the majority of excitons in the amorphous regions of the polymer. Verification of the singlet exciton contribution to this 1050 nm photoinduced absorption at high excitation densities from excitons in the amorphous regions is possible using ‘three-pulse’ or ‘pump-push-probe’ transient absorption experiments.

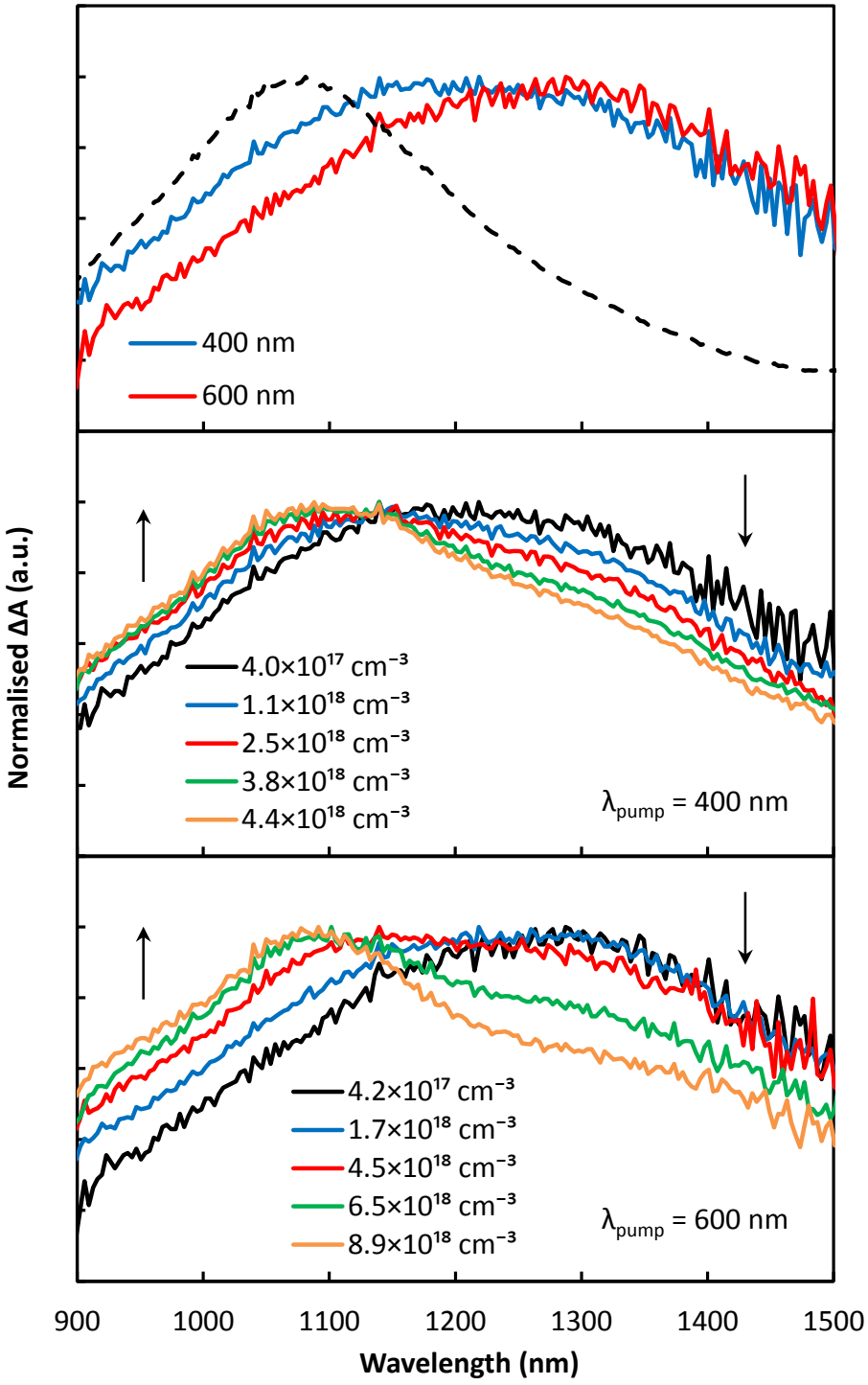


**Figure 6.4:** Transient absorption spectra of nanowires excited at 400 nm (blue) and 600 nm (red) for an excitation density of $4\times10^{17}$ $cm^{-3}$ (top). The exciton absorption of P3HT in THF (dashed) is shown for comparison. Transient absorption spectra of nanowires at increasing excitation densities for the 400 nm pump (middle) and 600 nm pump (bottom). All spectra were taken at 3 ps delay after which there is no change in the peak position.

In this experiment, an exciton is generated by the initial 400-nm pump pulse, which is re-excited by the 900-nm push pulse. The relaxation of the re-excited exciton, shown in Figure 6.5, is monitored by the 1050-nm probe pulse. Although spectral or kinetic dependence on the pump-push delay ($\Delta t$) was not observed for $\Delta t$ >2 ps, a delay of ~20 ps was chosen allowing the completion of fast relaxation processes such as energy transfer, before the arrival of the push pulse. The arrival of the push pulse manifests as a bleach of the singlet exciton absorption. As excitons are promoted to a higher electronic state, fewer excitons remain in the first singlet excited state to absorb the probe light. Alternatively, this observation can be explained by stimulated emission returning excitons to the ground state. However, the singlet exciton absorption bleached by the push pulse eventually returns to the same level as the decay measured in the absence of the push pulse. As the singlet exciton population is fully recovered, the extent of stimulated emission to the ground state is negligible. This is to be expected given the significant separation between the repump wavelength and the emission range of P3HT.

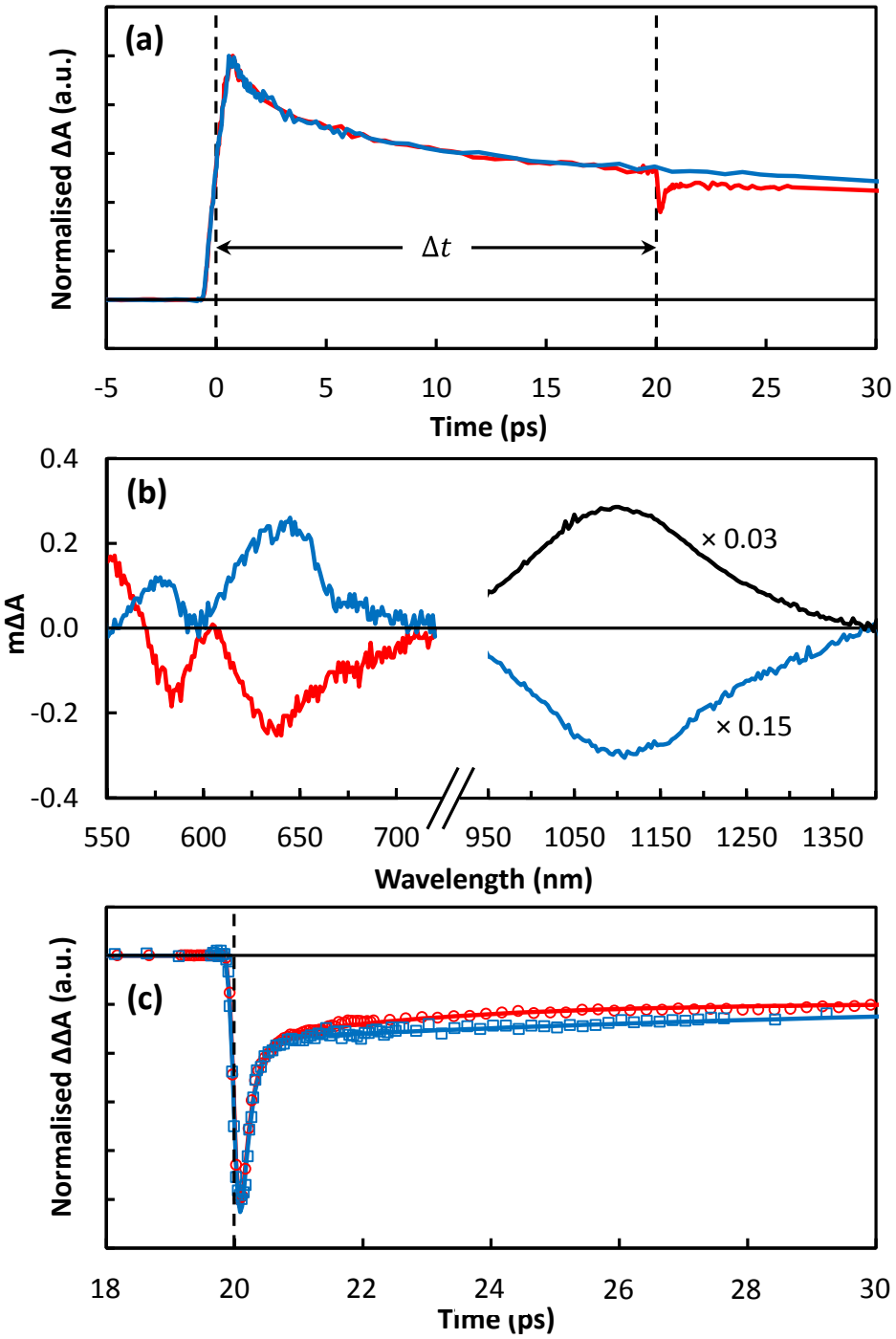


**Figure 6.5:** (a) Pump-probe (blue) and pump-push probe (red) singlet exciton decay in nanowires. (b) Comparison of spectral response to 900 nm push pulse (blue), a linear combination of ground state bleach and spontaneous emission spectra (red) and the singlet exciton absorption (black). (c) Kinetics of the excited state bleach recovery induced by the push pulse in nanowires (blue) and solutions of P3HT in THF (red).

The alternative configuration, in which the push beam is modulated, allows the push-probe experiment to interrogate the sample in the excited state. Figure 6.5b shows the spectral response of the nanowires to the push pulse. In the visible region this response mirrors a linear combination of the ground state bleach and spontaneous emission spectra. Furthermore, in the infrared region the push induced spectrum is a reflection of the singlet exciton absorption produced by the 400 nm pump with high excitation density. Therefore, the push pulse appears to only influence the singlet exciton, which is to be expected given the push wavelength of 900 nm is within the photoinduced absorption of the singlet exciton. Interestingly, the promotion of excitons to a higher excited state does not result in generation of any additional long-lived polarons. This is shown by the lack of repump response at a probe wavelength of 700 nm where the photoinduced absorption of the hole-polaron is known to occur. This would appear to be at odds with a study by Gadermaier *et al.*, in which increased polaron generation was observed for a substituted poly(*p*-phenylene) following re-excitation by the push pulse [209]. This study also showed the lifetime of the higher electronic state in this polymer was 45–55 fs, which is much shorter than the temporal resolution of our transient absorption system.

**Table 6.1:** Fitting parameters for the excited state bleach recovery in nanowires and solution of P3HT in THF at push wavelengths of 900 nm and 1200 nm. The large uncertainties for the nanowire time constants reflect the reduced signal to noise ratio for the nanowire sample.

| **Push = 900 nm** | $a_1$ | $\tau_1$ **(ps)** | $a_2$ | $\tau_2$ **(ps)** | $a_3$ | $\tau_3$ **(ps)** | $a_4$ | $\tau_4$ **(ps)** |
|---|---|---|---|---|---|---|---|---|
| Nanowires | -0.82 | 0.16 ± 0.06 | -0.07 | 7.7 ± 6.2 | -0.08 | 130 | -0.03 | 530 |
| THF Solution | -0.80 | 0.16 ± 0.10 | -0.09 | 2.6 ± 1.3 | -0.07 | 130 | -0.04 | 530 |
| **Push = 1200 nm** | $a_1$ | $\tau_1$ **(ps)** | $a_2$ | $\tau_2$ **(ps)** | $a_3$ | $\tau_3$ **(ps)** | $a_4$ | $\tau_4$ **(ps)** |
| Nanowires | -0.88 | 0.15 ± 0.19 | -0.07 | 4.3 ± 5.6 | -0.02 | 130 | -0.03 | 530 |
| THF Solution | -0.76 | 0.29 ± 0.17 | -0.11 | 4.3 ± 2.6 | -0.11 | 130 | -0.03 | 530 |

The kinetics of the excited state bleach recovery for nanowires and P3HT dissolved in THF are shown in Figure 6.5, with the corresponding fitting parameters listed in Table 6.1. The first component of the recovery for P3HT in THF is instrument response limited, followed by a minor recovery component with a time constant of 3 ps. The decay at longer delay times was fitted with two time constants, 135 ps and 530 ps, according to the decay of the pump-probe signal, which are in good agreement with values reported in the literature [139,141]. The major recovery component is attributed to the rapid relaxation (< 160 fs) from the higher excited state back to the first excited state (i.e. the excited state lifetime). Similarly, the first recovery component for the nanowires is instrument response limited and accounts for around 80% of the recovery, while the time constants and relative weightings of the other components are also comparable to that of the P3HT in THF data. The excited state bleach recovery data were also collected for a push wavelength of 1200 nm. These kinetic data show similar excited state lifetimes to the 900 nm data indicating there is little dependence on the

push wavelength within the excited state absorption band. The similarity between the excited state lifetime for nanowires and solutions of P3HT in THF suggests the excitons exist in the amorphous segments of the nanowires.

This three-pulse transient absorption system can be modified to probe the excited state recovery of excitons in crystalline domains of the nanowires, which is of significant interest [92,209,210] and will be investigated by our group in the future. However, given the low signal level of the three pulse response and the limited excitation density required to study excitons in the crystalline domains, this may prove challenging. An improvement in the temporal resolution is also necessary to properly capture the excited state lifetime.

## 6.4 Measurement of Exciton Diffusion Length

The exciton diffusion length in P3HT films has been extensively studied by time resolved spectroscopic methods with reported values ranging from 4 nm to 27 nm [211-216]. When the internal nanostructures of a bulk heterojunction device greatly exceed this diffusion length, loss pathways such as fluorescence and bimolecular recombination are introduced [47]. For this reason the 30-nm widths of these nanowires are well suited for bulk heterojunction devices. Several studies have demonstrated the precise control over the nanowire dimensions [198,217-219]; however, these reports assume the exciton diffusion length is the same as annealed P3HT films. Therefore, it is necessary to determine the exciton diffusion length in P3HT nanowires to provide insight for the optimal dimensions for maximising device performance. The exciton diffusion length can be determined by transient absorption using the approach described

in Chapter 5, where the singlet exciton decay is measured in the presence of an electron acceptor. Alternatively, samples without an electron acceptor subjected to increased pump intensities can generate multiple excitons within the range of energy transfer. In this case, singlet excitons decay through exciton annihilation rather than charge transfer but the process is still dependent on the range of energy transfer. Therefore, the decay of the singlet exciton population ($n(t)$) can be described by

$$\frac{dn(t)}{dt} = -\kappa n - \gamma n^2 \tag{6.2}$$

where $\kappa$ is the fluorescence decay rate constant and $\gamma$ is the annihilation rate constant. The exciton diffusion coefficient ($D$) can then be calculated by

$$\gamma = 4\pi R_a D \tag{6.3}$$

where $R_a$ is the reaction distance at which annihilation occurs. This reaction distance, while difficult to determine experimentally [212], is generally within 0.5–2.5 nm for P3HT [211-213,220], with a recent study by Heiber *et al.* reporting a value of 1.8 nm [221]. The diffusion coefficient is then used to calculate the one dimensional exciton diffusion length ($L_{ex}$) according to

$$L_{ex} = \sqrt{D\tau_r} \tag{6.4}$$

where $\tau_r$ is the lifetime of the excited state.

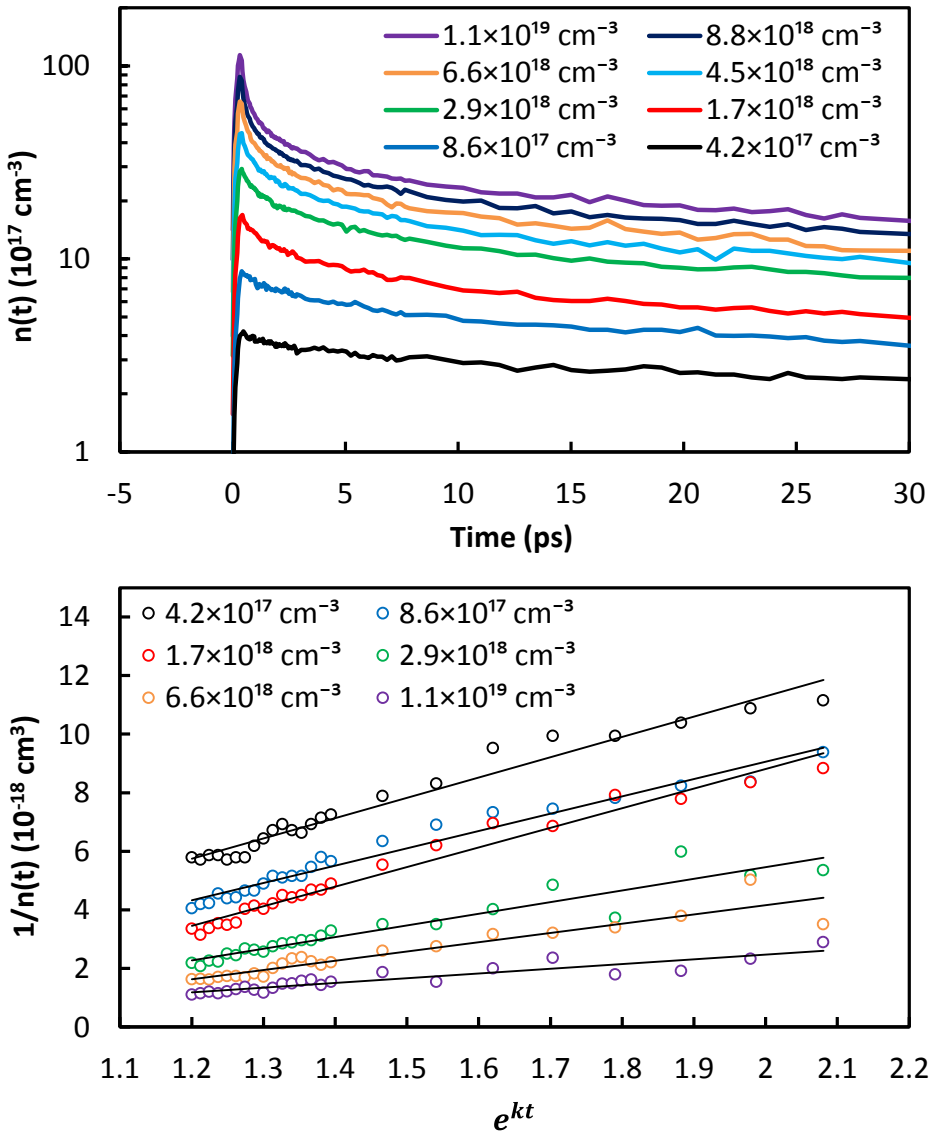


**Figure 6.6:** Power dependence of the nanowire singlet exciton absorption at 1250 nm (top) and the linearised data for calculation of the annihilation rate constant (bottom). The excitation densities are listed in each panel. Note: data for $4.4\times10^{18}$ $cm^{-3}$ and $8.8\times10^{18}$ $cm^{-3}$ are not shown in the bottom panel for clarity.

The exciton diffusion length for P3HT nanowires was calculated from the measured annihilation rate constant by applying two published methods to the transient absorption data shown in the top panel of Figure 6.6 [211,212]. In both approaches the annihilation rate constant ($\gamma$) was determined from the power dependence of the exciton decay data according to Eq. (6.2). The first method, reported by Shaw *et al.*, used the solution of

this equation to determine the time-independent annihilation rate constant [212,213]. This solution is given by

$$n(t) = \frac{n(0)e^{-\kappa t}}{1 + \frac{\gamma}{\kappa} n(0)[1 - e^{-\kappa t}]} \tag{6.5}$$

where $\kappa$ is the fluorescence decay rate constant and $n(0)$ is the initial exciton population. This equation can also be expressed in the linear form

$$\frac{1}{n(t)} = \left(\frac{1}{n(0)} + \frac{\gamma}{\kappa}\right) e^{\kappa t} - \frac{\gamma}{\kappa}, \tag{6.6}$$

which allows the annihilation rate constant to be calculated from the slope or intercept of the data shown in the bottom panel of Figure 6.6.

At the lowest excitation density of $4.2 \times 10^{17}$ cm$^{-3}$ at 600 nm, the decay of the singlet exciton population, shown in the top panel of Figure 6.6, is not mono-exponential. Furthermore, there is a noticeable difference in the singlet exciton decay kinetics even at the two lowest excitation densities measured here. Therefore, it is possible that exciton annihilation is present even at the lowest excitation density used here. The sensitivity of our transient absorption system prohibits measurements of kinetics with satisfactory signal to noise ratios below this excitation density. For this reason, fluorescence based techniques, with greater sensitivity are often used [211-215]. However, the low fluorescence quantum yields of these aggregates, particularly the nanoparticles, would make this approach similarly challenging. The time dependence of exciton annihilation rate constant has been demonstrated to occur over the first 100 ps [31], and therefore only data between 100 ps and 300 ps was considered for this analysis, which is in accordance with a previous study [214]. Furthermore, the fast initial decay makes $n(0)$ difficult to determine accurately; however, the average of

annihilation rate constants calculated from the slopes and intercepts, $6.2 \times 10^{-9}$ $cm^3s^{-1}$ and $6.4 \times 10^{-9}$ $cm^3s^{-1}$, respectively, are in excellent agreement. The errors in these annihilation rate constants, $2.6 \times 10^{-9}$ $cm^3s^{-1}$ and $2.4 \times 10^{-9}$ $cm^3s^{-1}$ for the slope and intercept, respectively, are taken as the standard deviation of the values over the range of excitation densities.

**Table 6.2:** Excitation densities and the corresponding annihilation rate constants calculated from the intercepts of data shown in Figure 6.6.

| **Excitation Density ($10^{17}$ $cm^{-3}$)** | **$\gamma$–Intercept ($10^{-9}$ $cm^3s^{-1}$)** |
|---|---|
| 4.2 | 5.3 |
| 8.6 | 6.2 |
| 17 | 7.9 |
| 29 | 11.1 |
| 45 | 5.5 |
| 66 | 7.0 |
| 88 | 6.0 |
| 114 | 2.6 |
| **Average** | **6.4 ± 2.4** |

From the average annihilation rate constant, $6.4 \times 10^{-9}$ $cm^3s^{-1}$, the exciton diffusion length was calculated using Eq. (6.3) and (6.4). For the commonly used reaction distance of 1 nm the diffusion length is 14 ± 3 nm, which is shortened to 11 ± 3 nm for a reaction distance of 1.8 nm. This 11 nm diffusion length is significantly longer than the 4.7 nm measured by Shaw *et al.* for annealed P3HT films assuming the 1 nm reaction distance. Luer *et al.* earlier reported a similar diffusion length of 4 nm for excitons in P3HT films quenched by molecular oxygen [216]. A very recent study by Masri *et al.* reported exciton diffusion lengths between 5.7 nm and 11 nm in films cast

from P3HT with molecular weights ranging from 4 kDa to 76 kDa [214]. The excitonic coupling for the 13.8 kDa film that exhibited the maximum diffusion length of 11 nm was ~80 meV. These studies show the exciton diffusion length in the nanowires measured here is on the upper limit of diffusion lengths observed in P3HT films, as a result of the more gentle crystallisation of P3HT in forming nanowires, which is expected to produce greater long range order.

Cook *et al.*, have reported two alternative methods for determining the annihilation rate constant from the power dependence of singlet exciton decay data [211]. The first method in this study shows the annihilation rate constant is actually time dependent. However, only their second method, that gives an average annihilation rate constant, is suitably applied here. Briefly, this average annihilation rate constant ($\gamma$) is calculated from the relative emission efficiency ($\Phi(I)/\Phi(I_0)$) at each excitation density ($I$) by

$$\frac{\Phi(I)}{\Phi(I_0)} = \frac{2\kappa}{\gamma\alpha I}\ln\left(1 + \frac{\gamma\alpha I}{2\kappa}\right) \qquad (6.7)$$

where $\kappa$ is the fluorescence decay rate constant, $\alpha$ is the absorption coefficient and $I_0$ is the lowest excitation density, which gives the maximum emission intensity due to the absence of exciton annihilation. At the pump wavelength of 600 nm, $\alpha$ = 45,000 $cm^{-1}$ and the nanowire solutions used here have an absorbance equivalent to a ~60 nm thick film, similar to that used in Cook's study.

Figure 6.7 shows the relative emission efficiency at different excitation densities for the nanowires. The data were fitted using Eq. (6.7), with the fluorescence lifetime of 400 ps, yielding an average annihilation rate constant of 1.0 × $10^{-9}$ $cm^3s^{-1}$. The fitting error in this value is 1 × $10^{-10}$ $cm^3s^{-1}$. However, this method requires the exciton decay at the lowest excitation density to be devoid of any exciton annihilation, which may not

be the case for these nanowire samples, as discussed earlier. Therefore, the exciton diffusion length of 5.7 nm calculated for the measured annihilation rate constant with a reaction distance of 1 nm is likely to be an underestimation of the true value. Again, for the increased reaction distance (1.8 nm) the diffusion length is reduced to 4.2 nm. Cook *et al.* reported a diffusion length of 27 ± 12 nm. For a reaction distance of 1 nm this uncertainty is reduced below 10 nm. This is considerably longer than any other reported diffusion length in P3HT including that measured here for nanowires and has been attributed to the longer fluorescence lifetime of 600 ps. The large uncertainties for this reported diffusion length and the diffusion length measured by Shaw's method show some agreement. However, the diffusion length measured for P3HT nanowires using this method is considerably shorter, as would be expected when the exciton decay at the lowest excitation density contains exciton annihilation.

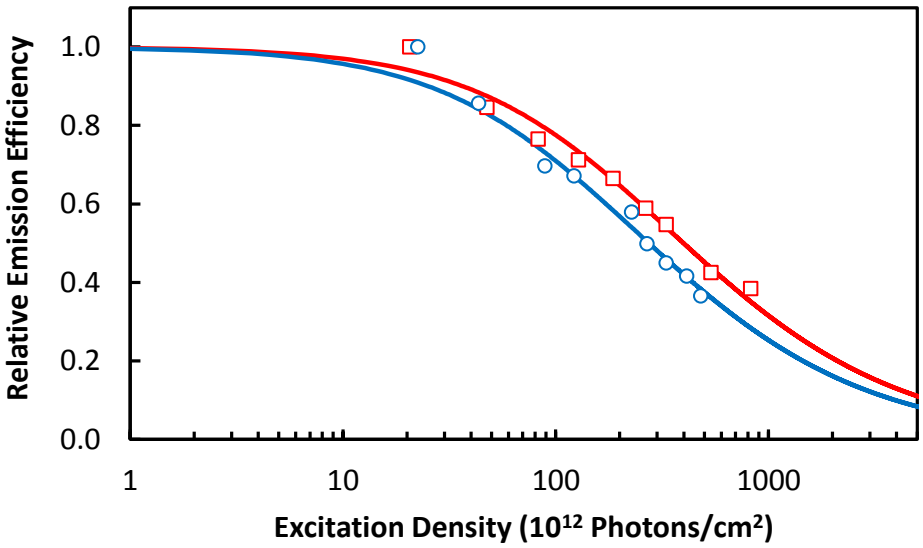


**Figure 6.7:** The relative emission efficiency of the singlet exciton absorption at increasing photon flux for the nanowires (blue) and nanoparticles (red) pumped at 600 nm. The best fits for annihilation constants of $1.0 \times 10^{-9}$ $cm^3s^{-1}$ and $9.6 \times 10^{-10}$ $cm^3s^{-1}$ for the nanowires and nanoparticles, respectively, are also shown.

It is also possible to apply this analysis to nanoparticle samples in which the exciton decays much more rapidly. For fitting this nanoparticle data, also shown in Figure 6.7, $\alpha$ was scaled to 32,600 $cm^{-1}$ due to the reduced absorptivity at 600 nm relative to the nanowire sample. The fitted annihilation rate constant of $9.6\times10^{-10}$ $cm^3s^{-1}$ reflects the similarity in the power dependence of the relative emission efficiency for these samples. This equates to a diffusion length of $5.5 \pm 2.4$ nm for the nanoparticles considering the uncertainty in the reaction distance, which shows good agreement with results presented in Chapter 5. Similarly, a study by Labastide *et al.*, reported crystalline domain sizes of 5–10 nm in nanoparticles using high-resolution transmission electron microscopy [83]. Interestingly, this diffusion length is not significantly different to that of the nanowires, which is somewhat surprising given the considerably greater crystallinity of the nanowire sample.

## 6.5 Conclusions

In this chapter, the effect of polymer order on the exciton diffusion length in two P3HT nanostructures has been presented. The nanoparticles have an excitonic coupling of 106 meV, which was greater than the nanowires due to the more rapid crystallisation in nanoparticle preparation. Pump-probe and pump-push-probe transient absorption experiments showed excitons annihilate much more efficiently in the crystalline domains than the amorphous regions of the polymer for increasing excitation densities. This power dependence of the singlet exciton absorption was also used to determine the annihilation rate constant by two published methods. The more reliable exciton diffusion length of 11 ± 3 nm is on the longer end of the range of diffusion lengths reported for annealed P3HT films. The second method yielded diffusion lengths of ~5.5 nm for nanowire and nanoparticle samples. These measurements of the exciton diffusion length and exciton behaviour observed in these nanostructures are further contributions to the optimisation of bulk heterojunction devices.

# 7 Conclusions and Outlook

In this work, the colloidal stability and photophysical processes in aqueous suspensions of conjugated polymer nanoparticles have been investigated. Such properties are of significance to fluorescence imaging and sensing applications as well as conventional applications of conjugated polymers. Many promising studies using these nanoparticles have been published without a full understanding of their energy transfer behaviour [78,222]. This work has aimed to address these unknowns and present further information regarding their performance in key processes for photovoltaics and PLEDs.

The source colloidal stability of these nanoparticles, investigated in Chapter 3, was found to be the negatively charged surface. Through zeta potential and particle size measurements by AFM, the surface charge density of 14.3 $mC/m^2$ for MEH-PPV nanoparticles at pH 7 was calculated. Surface charge density of this magnitude is sufficient to stabilise the suspension for several weeks; however, aggregation was only observed at surface charge densities below 6.5 $mC/m^2$. Changes in the chemical composition of the polymer were observed after nanoparticle preparation using a combination of FT-IR, XPS and elemental analysis. The emergence of three absorption peaks in the carbonyl region of the infrared spectrum at 1730 $cm^{-1}$, 1670 $cm^{-1}$ and

1600 $cm^{-1}$, shows oxidation of the polymer and potentially the formation of carboxylate groups. This was confirmed by XPS, where two extra spectral components at 287.9 eV and 289.4 eV were present and assigned to carbon atoms of carbonyl and carboxylate groups, respectively. Elemental analysis was used to quantify the oxygen content of the polymer and nanoparticle, rather than XPS which may be biased towards the composition of the sample surface. Considering only the polyfluorenes studied here, which in their pristine form contain no oxygen, the measured oxygen concentration was 7-13% in the nanoparticle sample. Other sources of negative surface charge, such as the physisorption of hydroxide anions to hydrophobic surfaces, have been reported but remain controversial. Therefore, it is possible the polymer oxidation is not the only source of negative surface charge, but rather a contributing factor. Furthermore, the absorption and fluorescence spectra of polymer and nanoparticle films gave early indications regarding the internal structure of the nanoparticle.

In Chapter 4, energy transfer in two polymer conformations was examined. Isotropic time-resolved fluorescence upconversion data of MEH-PPV in THF at several emission energies showed the population of lower energy chromophores at the expense of higher energy chromophores by energy transfer. The nanoparticles showed a similar trend; however, this was partially obstructed by the shorter fluorescence lifetime in the aqueous suspension. The rate of energy transfer in each sample was then measured directly through time-resolved fluorescence anisotropy experiments, in which energy transfer of the polymer in THF occurred through both intermolecular and intramolecular channels, while the nanoparticles were found to exclusively undergo intermolecular energy transfer. These anisotropy decays were also simulated using coarse-grained molecular dynamics simulations to produce physically realistic polymer conformations, which were then used as the input structures for the Monte Carlo based

energy transfer algorithm. The resulting simulated anisotropy decays were in reasonable agreement with the measured values indicating these structures are consistent with true polymer conformations. The exciton diffusion lengths of 4 ± 1 nm and 9 ± 2 nm for the polymer and nanoparticles, respectively, were also determined by the model. However, the rate constant for energy transfer in the nanoparticle simulations shortly after excitation was unreasonably large. Therefore, it is necessary to extend this line-dipole FRET-based model used here by incorporating the exciton localisation described by the Frenkel exciton model [16]. This model is likely to provide a better estimate of the exciton hopping rate and initial anisotropy values, particularly for polymer structures with strongly coupled chromophores.

The internal structure and the dynamics of photoinduced charge separation in rr-P3HT/PCBM composite nanoparticles was presented in Chapter 5. Absorption spectra of these nanoparticles were vastly red-shifted and contained considerable vibronic structure, indicating the formation of semicrystalline domains. The fluorescence of rr-P3HT nanoparticles was not entirely quenched by charge transfer associated with the incorporation of PCBM, which suggests the size of these polymer domains must be comparable or greater than the exciton diffusion length. Interestingly, the rra-P3HT fluorescence was completely quenched at 20 wt% PCBM showing the absence of these ordered domains allows a much more homogeneous distribution of the acceptor. Excited state and charged species were identified using visible pump and visible/near-infrared probe femtosecond transient absorption spectroscopy. Undoped rr-P3HT nanoparticles exhibited photoinduced absorption bands at 650 nm and 1250 nm, which were assigned to hole-polarons and singlet excitons, respectively. Nanoparticles containing 50 wt% PCBM showed another photoinduced absorption band at 1000 nm that emerges from within the singlet exciton band, which is also assigned to hole-

polarons in P3HT. The incorporation of PCBM quenches the singlet exciton lifetime, which is consistent with charge transfer. The characteristic length of rr-P3HT domains and the rate of geminate recombination were extracted from the transient absorption signal at 1000 nm using a one dimensional diffusion model. The concentration of PCBM did not significantly influence this domain length over the range of acceptor concentrations studied here. Bimolecular recombination was found to be the primary charge recombination mechanism at high acceptor concentrations owing to the more effective charge separation associated with larger PCBM aggregates. These results show good agreement with previous film studies confirming these composite nanoparticles are a suitable model system for polymer bulk heterojunction devices.

In Chapter 6, the influence of the polymer nanostructure on energy transfer was explored. The degree of crystallinity in the nanowires and nanoparticles was quantified by the excitonic couplings of 78 meV and 106 meV, respectively, indicating a greater order in the nanowire structures. Femtosecond transient absorption spectra of the nanowires and nanoparticles contain several common features. The primary difference in these data arises from the rate of polaron recombination, which is considerably faster in the nanowires; a result that is consistent with relative crystallinities of these samples. Furthermore, the power dependence of the singlet exciton band position along with the generation of polarons, show that excitons are found predominantly in the amorphous segments of the polymer as a result of efficient exciton annihilation in the crystalline domains at higher excitation densities. This was confirmed by pump-push-probe transient absorption spectroscopy experiments, which also showed the lifetime of the higher excited state generated by the push pulse was less than 160 fs. Interestingly, no appreciable long-lived polaron population was generated following re-excitation by the 900 nm push pulse. Finally, the power dependence on the decay of the singlet exciton

population was used to measure the exciton diffusion length through exciton annihilation. The diffusion length in nanowires was measured to be $11 \pm 3$ nm by Shaw's method [212], which is greater than the majority of reported diffusion lengths for annealed films. Using Cook's method [211], the diffusion length was found to be $5.7 \pm 1.5$ nm. This is likely to be an underestimate of the true diffusion length as exciton annihilation occurring at even the lowest excitation density used here is probable. The diffusion length of the nanoparticles, also measured by Cook's method, showed similar power dependence and a diffusion length close to that of the nanowires.

In this thesis, two main areas have been identified for further investigation. Firstly, energy transfer simulations require the incorporation of the Frenkel exciton model to properly define the boundaries and energies of chromophores and better describe the exciton localisation process immediately following excitation and the energy transfer events that then immediately follow. Currently, this is a focus of our group, which should yield a comprehensive model capable of simulating energy transfer in MEH-PPV for a range of chromophore coupling strengths. We have also performed some preliminary investigations of energy transfer in P3HT, for which the coarse-grained model has already been parameterised and used to produce nanowire-like aggregates. Secondly, the shortened fluorescence lifetime and poor charge transport in P3HT nanoparticles compared to annealed films also suggests the future of these nanoparticles is limited to emission-based applications, such as fluorescent imaging probes and PLEDs, rather than photovoltaics. Conversely, nanowires of P3HT appear to be more promising given the exciton diffusion length exceeding 10 nm reported here and several device studies claiming efficiencies upwards of 4%. Further investigation of the higher excited state dynamics, with improved temporal resolution, is also warranted to probe exciton delocalisation in the amorphous and crystalline phases of these nanowires.

# References


[1] Shirakawa, H., Louis, E.J., MacDiarmid, A.G., Chiang, C.K. and Heeger, A.J., *Journal of the Chemical Society, Chemical Communications*, **1977**, 578-580.

[2] Chiang, C.K., Fincher, C.R., Jr., Park, Y.W., Heeger, A.J., Shirakawa, H., Louis, E.J., Gau, S.C. and MacDiarmid, A.G., *Physical Review Letters*, **1977**, 39, 1098-1101.

[3] Sariciftci, N.S., Smilowitz, L., Heeger, A.J. and Wudl, F., *Science*, **1992**, 258, 1474-1476.

[4] Burroughes, J.H., Bradley, D.D.C., Brown, A.R., Marks, R.N., Mackay, K., Friend, R.H., Burns, P.L. and Holmes, A.B., *Nature*, **1990**, 347, 539-541.

[5] Hu, D., Yu, J., Wong, K., Bagchi, B., Rossky, P.J. and Barbara, P.F., *Nature*, **2000**, 405, 1030-1033.

[6] Hagler, T.W., Pakbaz, K. and Heeger, A.J., *Physical Review B*, **1994**, 49, 10968-10975.

[7] Grage, M.M.L., Pullerits, T., Ruseckas, A., Theander, M., Inganäs, O. and Sundström, V., *Chemical Physics Letters*, **2001**, 339, 96-102.

[8] Grage, M.M.L., Wood, P.W., Ruseckas, A., Pullerits, T., Mitchell, W., Burn, P.L., Samuel, I.D.W. and Sundstrom, V., *The Journal of Chemical Physics*, **2003**, 118, 7644-7650.

[9] Nguyen, T.-Q., Doan, V. and Schwartz, B.J., *The Journal of Chemical Physics*, **1999**, 110, 4068-4078.

[10] Daoust, G. and Leclerc, M., *Macromolecules*, **1991**, 24, 455-459.

[11] Mei, J. and Bao, Z., *Chemistry of Materials*, **2013**.

[12] Yang, L., Zhou, H. and You, W., *The Journal of Physical Chemistry C*, **2010**, 114, 16793-16800.

[13] Matsumi, N., Miyata, M. and Chujo, Y., *Macromolecules*, **1999**, 32, 4467-4469.

[14] Jin, Z. and Lucht, B.L., *Journal of Organometallic Chemistry*, **2002**, 653, 167-176.

[15] Patra, A. and Bendikov, M., *Journal of Materials Chemistry*, **2010**, 20, 422-433.

[16] Barford, W., Bittner, E.R. and Ward, A., *The Journal of Physical Chemistry A*, **2012**, 116, 10319-10327.

[17] Valeur, B., *Molecular Fluorescence: Effects of Intermolecular Photophysical Processes on Fluorescence Emission*, **2001**, Wiley-VCH Verlag GmbH, 72-124.

[18] Lakowicz, J.R., *Principles of Fluorescence Spectroscopy*, 3 ed.,**2006**, Springer.

[19] Westenhoff, S., Daniel, C., Friend, R.H., Silva, C., Sundstrom, V. and Yartsev, A., *The Journal of Chemical Physics*, **2005**, 122, 094903-094908.

[20] Kasha, M., *Radiation Research*, **1963**, 20, 55-70.

[21] McRae, E.G. and Kasha, M., *The Journal of Chemical Physics*, **1958**, 28, 721-722.

[22] Kasha, M., Rawls, H.R. and El-Bayoumi, M.A., *Pure and Applied Chemistry*, **1965**, 11, 371-392.

[23] Yamagata, H. and Spano, F.C., *The Journal of Chemical Physics*, **2012**, 136, -.

[24] Spano, F.C., *Accounts of Chemical Research*, **2009**, 43, 429-439.

[25] Bredas, J.L. and Street, G.B., *Accounts of Chemical Research*, **1985**, 18, 309-315.

[26] Miranda, P.B., Moses, D. and Heeger, A.J., *Physical Review B*, **2001**, 64, 081201.

[27] Reid, O.G. and Rumbles, G., *The Journal of Physical Chemistry Letters*, **2013**, 4, 2348-2355.

[28] Bolinger, J.C., Traub, M.C., Adachi, T. and Barbara, P.F., *Science*, **2011**, 331, 565-567.

[29] Hodgkiss, J.M., Albert-Seifried, S., Rao, A., Barker, A.J., Campbell, A.R., Marsh, R.A. and Friend, R.H., *Advanced Functional Materials*, **2012**, 22, 1567-1577.

[30] Miranda, P.B., Moses, D. and Heeger, A.J., *Physical Review B*, **2004**, 70, 085212.

[31] Cook, S., Furube, A. and Katoh, R., *Energy & Environmental Science*, **2008**, 1, 294-299.

[32] Banerji, N., Cowan, S., Vauthey, E. and Heeger, A.J., *The Journal of Physical Chemistry C*, **2011**, 115, 9726-9739.

[33] Stranks, S.D., Eperon, G.E., Grancini, G., Menelaou, C., Alcocer, M.J.P., Leijtens, T., Herz, L.M., Petrozza, A. and Snaith, H.J., *Science*, **2013**, 342, 341-344.

[34] Macdonald, D. and Cuevas, A., *Applied Physics Letters*, **1999**, 74, 1710-1712.

[35] Tang, C.W., *Applied Physics Letters*, **1986**, 48, 183-185.

[36] Sariciftci, N.S., Braun, D., Zhang, C., Srdanov, V.I., Heeger, A.J., Stucky, G. and Wudl, F., *Applied Physics Letters*, **1993**, 62, 585-587.

[37] Günes, S., Neugebauer, H. and Sariciftci, N.S., *Chemical Reviews*, **2007**, 107, 1324-1338.

[38] Forrest, S.R., *MRS Bulletin*, **2005**, 30, 28-32.

[39] Li, G., Shrotriya, V., Huang, J., Yao, Y., Moriarty, T., Emery, K. and Yang, Y., *Nat Mater*, **2005**, 4, 864-868.

[40] Mihailetchi, V.D., Xie, H.X., de Boer, B., Koster, L.J.A. and Blom, P.W.M., *Advanced Functional Materials*, **2006**, 16, 699-708.

[41] Zhao, J., Swinnen, A., Van Assche, G., Manca, J., Vanderzande, D. and Mele, B.V., *The Journal of Physical Chemistry B*, **2009**, 113, 1587-1591.

[42] Erb, T., Zhokhavets, U., Gobsch, G., Raleva, S., Stühn, B., Schilinsky, P., Waldauf, C. and Brabec, C.J., *Advanced Functional Materials*, **2005**, 15, 1193-1196.

[43] Slota, J.E., He, X. and Huck, W.T.S., *Nano Today*, **2010**, 5, 231-242.

[44] Ihn, K.J., Moulton, J. and Smith, P., *Journal of Polymer Science Part B: Polymer Physics*, **1993**, 31, 735-742.

[45] Kim, J.-H., Park, J.H., Lee, J.H., Kim, J.S., Sim, M., Shim, C. and Cho, K., *Journal of Materials Chemistry*, **2010**, 20, 7398-7405.

[46] Kim, B.-G., Kim, M.-S. and Kim, J., *ACS Nano*, **2010**, 4, 2160-2166.

[47] Kurniawan, M., Salim, T., Tai, K.F., Sun, S., Sie, E.J., Wu, X., Yeow, E.K.L., Huan, C.H.A., Lam, Y.M. and Sum, T.C., *The Journal of Physical Chemistry C*, **2012**, 116, 18015-18022.

[48] Kietzke, T., Neher, D., Landfester, K., Montenegro, R., Guntner, R. and Scherf, U., *Nat Mater*, **2003**, 2, 408-412.

[49] Kietzke, T., Neher, D., Kumke, M., Montenegro, R., Landfester, K. and Scherf, U., *Macromolecules*, **2004**, 37, 4882-4890.

[50] Andersen, T.R., Larsen-Olsen, T.T., Andreasen, B., Böttiger, A.P.L., Carlé, J.E., Helgesen, M., Bundgaard, E., Norrman, K., Andreasen, J.W., Jørgensen, M. and Krebs, F.C., *ACS Nano*, **2011**, 5, 4188-4196.

[51] Sarrazin, P., Chaussy, D., Vurth, L., Stephan, O. and Beneventi, D., *Langmuir*, **2009**, 25, 6745-6752.

[52] Tuncel, D. and Demir, H.V., *Nanoscale*, **2010**, 2, 484-494.

[53] Boulas, C., Davidovits, J.V., Rondelez, F. and Vuillaume, D., *Physical Review Letters*, **1996**, 76, 4797-4800.

[54] Stapleton, A., Vaughan, B., Xue, B., Sesa, E., Burke, K., Zhou, X., Bryant, G., Werzer, O., Nelson, A., David Kilcoyne, A.L., Thomsen, L., Wanless, E., Belcher, W. and Dastoor, P., *Solar Energy Materials and Solar Cells*, **2012**, 102, 114-124.

[55] Darwis, D., Elkington, D., Sesa, E., Cooling, N., Bryant, G., Zhou, X., Belcher, W. and Dastoor, P., *AIP Conference Proceedings*, **2011**, 1415, 120-123.

[56] Wu, C.F., Szymanski, C. and McNeill, J., *Langmuir*, **2006**, 22, 2956-2960.

[57] Wu, C., Zheng, Y., Szymanski, C. and McNeill, J., *Journal of Physical Chemistry C*, **2008**, 112, 1772-1781.

[58] Wu, C., Szymanski, C., Cain, Z. and McNeill, J., *Journal of the American Chemical Society*, **2007**, 129, 12904-+.

[59] Wu, C., Schneider, T., Zeigler, M., Yu, J., Schiro, P.G., Burnham, D.R., McNeill, J.D. and Chiu, D.T., *Journal of the American Chemical Society*, **2010**, 132, 15410-15417.

[60] Wu, C., Peng, H., Jiang, Y. and McNeill, J., *Journal of Physical Chemistry B*, **2006**, 110, 14148-14154.

[61] Tian, Z., Yu, J., Wu, C., Szymanski, C. and McNeill, J., *Nanoscale*, **2010**, 2, 1999-2011.

[62] Jin, Y., Ye, F., Wu, C., Chan, Y.-H. and Chiu, D.T., *Chemical Communications*, **2012**, 48, 3161-3163.

[63] Tian, Z., Yu, J., Wang, X., Groff, L.C., Grimland, J.L. and McNeill, J.D., *The Journal of Physical Chemistry B*, **2012**, 117, 4517-4520.

[64] Wu, C., Bull, B., Christensen, K. and McNeill, J., *Angew. Chem., Int. Ed.*, **2009**, 48, 2741-2745.

[65] Wu, C., Bull, B., Szymanski, C., Christensen, K. and McNeill, J., *ACS Nano*, **2008**, 2, 2415-2423.

[66] Yu, J., Wu, C., Sahu, S.P., Fernando, L.P., Szymanski, C. and McNeill, J., *Journal of the American Chemical Society*, **2009**, 131, 18410-18414.

[67] MacNeill, C.M., Coffin, R.C., Carroll, D.L. and Levi-Polyachenko, N.H., *Macromolecular Bioscience*, **2013**, 13, 28-34.

[68] Chan, Y.-H., Wu, C., Ye, F., Jin, Y., Smith, P.B. and Chiu, D.T., *Analytical Chemistry*, **2011**, 83, 1448-1455.

[69] Ye, F., Wu, C., Jin, Y., Chan, Y.-H., Zhang, X. and Chiu, D.T., *Journal of the American Chemical Society*, **2011**, 133, 8146-8149.

[70] Childress, E.S., Roberts, C.A., Sherwood, D.Y., LeGuyader, C.L.M. and Harbron, E.J., *Analytical Chemistry*, **2012**, 84, 1235-1239.

[71] Yang, H., Duan, C., Wu, Y., Lv, Y., Liu, H., Lv, Y., Xiao, D., Huang, F., Fu, H. and Tian, Z., *Particle & Particle Systems Characterization*, **2013**, 30, 972-980.

[72] Ma, C., Zeng, F., Huang, L. and Wu, S., *The Journal of Physical Chemistry B*, **2011**, 115, 874-882.

[73] Tenery, D. and Gesquiere, A.J., *Chemical Physics*, **2009**, 365, 138-143.

[74] Tenery, D. and Gesquiere, A.J., *ChemPhysChem*, **2009**, 10, 2449-2457.

[75] Tenery, D., Worden, J.G., Hu, Z. and Gesquiere, A.J., *Journal of Luminescence*, **2009**, 129, 423-429.

[76] Wu, C. and McNeill, J., *Langmuir*, **2008**, 24, 5855-5861.

[77] Hu, Z., Tenery, D., Bonner, M.S. and Gesquiere, A.J., *Journal of Luminescence*, **2010**, 130, 771-780.

[78] Hu, Z. and Gesquiere, A.J., *Chemical Physics Letters*, **2009**, 476, 51-55.

[79] Gesquiere, A.J., Tenery, D. and Hu, Z., *Spectroscopy*, **2008**, 23, 32-44.

[80] Huyal, I.O., Ozel, T., Tuncel, D. and Demir, H.V., *Optics Express*, **2008**, 16, 13391-13397.

[81] Grey, J.K., Kim, D.Y., Norris, B.C., Miller, W.L. and Barbara, P.F., *The Journal of Physical Chemistry B*, **2006**, 110, 25568-25572.

[82] Clafton, S.N., Beattie, D.A., Mierczynska-Vasilev, A., Acres, R.G., Morgan, A.C. and Kee, T.W., *Langmuir*, **2010**, 26, 17785-17789.

[83] Labastide, J.A., Baghgar, M., Dujovne, I., Venkatraman, B.H., Ramsdell, D.C., Venkataraman, D. and Barnes, M.D., *The Journal of Physical Chemistry Letters*, **2011**, 2, 2089-2093.

[84] Clafton, S.N., Huang, D.M., Massey, W.R. and Kee, T.W., *The Journal of Physical Chemistry B*, **2013**.

[85] Hu, Z. and Gesquiere, A.J., *Journal of the American Chemical Society*, **2011**, 133, 20850-20856.

[86] Davis, C.M., Childress, E.S. and Harbron, E.J., *J. Phys. Chem. C*, **2011**, 115, 19065-19073.

[87] Samitsu, S., Shimomura, T., Heike, S., Hashizume, T. and Ito, K., *Macromolecules*, **2008**, 41, 8000-8010.

[88] Maiman, T.H., *Nature*, **1960**, 187, 493-494.

[89] Keller, U., *Nature*, **2003**, 424, 831-838.

[90] Morgner, U., Kärtner, F.X., Cho, S.H., Chen, Y., Haus, H.A., Fujimoto, J.G., Ippen, E.P., Scheuer, V., Angelow, G. and Tschudi, T., *Optics Letters*, **1999**, 24, 411-413.

[91] Spectra-Physics, *Spitfire Pro User Manual*, 2008, Newport Corporation: Mountain View, CA.

[92] Bakulin, A.A., Rao, A., Pavelyev, V.G., van Loosdrecht, P.H.M., Pshenichnikov, M.S., Niedzialek, D., Cornil, J., Beljonne, D. and Friend, R.H., *Science*, **2012**, 335, 1340-1344.

[93] Busby, E., Carroll, E.C., Chinn, E.M., Chang, L., Moulé, A.J. and Larsen, D.S., *The Journal of Physical Chemistry Letters*, **2011**, 2, 2764-2769.

[94] Eastman, J., *Colloid Science: Colloid Stability*, **2009**, Blackwell Publishing Ltd., 36-49.

[95] IUPAC, *Compendium of Chemical Terminology*, 2 ed.,**1997**, Blackwell Scientific Publications Oxford.

[96] Vincent, B., *Colloid Science: Introduction to Colloidal Dispersions*, **2009**, Blackwell Publishing Ltd., 1-13.

[97] Napper, D.H., *Journal of Colloid and Interface Science*, **1977**, 58, 390-407.

[98] Li, I.T.S. and Walker, G.C., *Proceedings of the National Academy of Sciences*, **2011**, 108, 16527-16532.

[99] Wu, C., Jin, Y., Schneider, T., Burnham, D.R., Smith, P.B. and Chiu, D.T., *Angewandte Chemie International Edition*, **2010**, 49, 9436-9440.

[100] Baier, M.C., Huber, J. and Mecking, S., *Journal of the American Chemical Society*, **2009**, 131, 14267-14273.

[101] Hashim, Z., Howes, P. and Green, M., *Journal of Materials Chemistry*, **2011**, 21, 1797-1803.

[102] Feng, L., Zhu, C., Yuan, H., Liu, L., Lv, F. and Wang, S., *Chemical Society Reviews*, **2013**, 42, 6620-6633.

[103] Xing, C., Xu, Q., Tang, H., Liu, L. and Wang, S., *Journal of the American Chemical Society*, **2009**, 131, 13117-13124.

[104] Wang, S. and Bazan, G.C., *Chemical Communications*, **2004**, 2508-2509.

[105] Feng, X., Yang, G., Liu, L., Lv, F., Yang, Q., Wang, S. and Zhu, D., *Advanced Materials*, **2012**, 24, 637-641.

[106] Kim, Y., Cook, S., Tuladhar, S.M., Choulis, S.A., Nelson, J., Durrant, J.R., Bradley, D.D.C., Giles, M., McCulloch, I., Ha, C.-S. and Ree, M., *Nat Mater*, **2006**, 5, 197-203.

[107] Bright, D.W., Dias, F.B., Galbrecht, F., Scherf, U. and Monkman, A.P., *Advanced Functional Materials*, **2009**, 19, 67-73.

[108] Vogelsang, J., Adachi, T., Brazard, J., Vanden Bout, D.A. and Barbara, P.F., *Nat Mater*, **2011**, 10, 942-946.

[109] Elimelech, M., Gregory, J., Jia, X., Williams, R.A., Gregory, J., Jia, X. and Williams, R.A., *Particle Deposition & Aggregation: Electrical Properties of Interfaces*, **1995**, Butterworth-Heinemann: Woburn, 9-32.

[110] Sussman, E.M., Clarke, M.B. and Shastri, V.P., *Langmuir*, **2007**, 23, 12275-12279.

[111] Goldys, E.M. and Sobhan, M.A., *Advanced Functional Materials*, **2012**, 22, 1906-1913.

[112] Atreya, M., Li, S., Kang, E.T., Neoh, K.G., Ma, Z.H., Tan, K.L. and Huang, W., *Polymer Degradation and Stability*, **1999**, 65, 287-296.

[113] Stuart, B.H., *Infrared Spectroscopy: Fundamentals and Applications*, **2004**, John Wiley & Sons Chichester, U.K.

[114] Geng, H., Guo, Y., Peng, R., Han, S. and Wang, M., *Solar Energy Materials and Solar Cells*, **2010**, 94, 1293-1299.

[115] Briggs, D., *Surface Analysis of Polymers by XPS and Static SIMS***1998**, Cambridge University Press.

[116] Hawker, C.J. and Wooley, K.L., *Science*, **2005**, 309, 1200-1205.

[117] Zhang, Q., Remsen, E.E. and Wooley, K.L., *Journal of the American Chemical Society*, **2000**, 122, 3642-3651.

[118] Nikishin, G.I., Glukhovtsev, V.G., Peikova, M.A. and Ignatenko, A.V., *Bulletin of the Academy of Sciences of the USSR, Division of chemical science*, **1971**, 20, 2202-2204.

[119] Gotchev, G., Kolarov, T., Khristov, K. and Exerowa, D., *Colloids and Surfaces A: Physicochemical and Engineering Aspects*, **2010**, 354, 56-60.

[120] Zangi, R. and Engberts, J.B.F.N., *Journal of the American Chemical Society*, **2005**, 127, 2272-2276.

[121] Tian, C.S. and Shen, Y.R., *Proceedings of the National Academy of Sciences*, **2009**, 106, 15148-15153.

[122] Kudin, K.N. and Car, R., *Journal of the American Chemical Society*, **2008**, 130, 3915-3919.

[123] Vacha, R., Horinek, D., Berkowitz, M.L. and Jungwirth, P., *Physical Chemistry Chemical Physics*, **2008**, 10, 4975-4980.

[124] Roger, K. and Cabane, B., *Angewandte Chemie International Edition*, **2012**, 51, 5625-5628.

[125] Zimmermann, R., Freudenberg, U., Schweiß, R., Küttner, D. and Werner, C., *Current Opinion in Colloid & Interface Science*, **2010**, 15, 196-202.

[126] Dou, L., You, J., Yang, J., Chen, C.-C., He, Y., Murase, S., Moriarty, T., Emery, K., Li, G. and Yang, Y., *Nat Photon*, **2012**, 6, 180-185.

[127] Facchetti, A., *Materials Today*, **2013**, 16, 123-132.

[128] Sista, S., Hong, Z., Chen, L.-M. and Yang, Y., *Energy & Environmental Science*, **2011**, 4, 1606-1620.

[129] Peet, J., Brocker, E., Xu, Y. and Bazan, G.C., *Advanced Materials*, **2008**, 20, 1882-1885.

[130] Kabra, D., Lu, L.P., Song, M.H., Snaith, H.J. and Friend, R.H., *Advanced Materials*, **2010**, 22, 3194-3198.

[131] Chu, C.-W., Yang, H., Hou, W.-J., Huang, J., Li, G. and Yang, Y., *Applied Physics Letters*, **2008**, 92, 103306-103303.

[132] Ma, W., Yang, C., Gong, X., Lee, K. and Heeger, A.J., *Advanced Functional Materials*, **2005**, 15, 1617-1622.

[133] Woo, C.H., Thompson, B.C., Kim, B.J., Toney, M.F. and Fréchet, J.M.J., *Journal of the American Chemical Society*, **2008**, 130, 16324-16329.

[134] van Bavel, S.S., Bärenklau, M., de With, G., Hoppe, H. and Loos, J., *Advanced Functional Materials*, **2010**, 20, 1458-1463.

[135] Grage, M.M.L., Zaushitsyn, Y., Yartsev, A., Chachisvilis, M., Sundström, V. and Pullerits, T., *Physical Review B*, **2003**, 67, 205207.

[136] Westenhoff, S., Beenken, W.J.D., Yartsev, A. and Greenham, N.C., *The Journal of Chemical Physics*, **2006**, 125, 154903-154907.

[137] Daniel, C., Westenhoff, S., Makereel, F., Friend, R.H., Beljonne, D., Herz, L.M. and Silva, C., *The Journal of Physical Chemistry C*, **2007**, 111, 19111-19119.

[138] Schwartz, B.J., *Annual Review of Physical Chemistry*, **2003**, 54, 141-172.

[139] Wells, N.P., Boudouris, B.W., Hillmyer, M.A. and Blank, D.A., *The Journal of Physical Chemistry C*, **2007**, 111, 15404-15414.

[140] Dykstra, T.E., Hennebicq, E., Beljonne, D., Gierschner, J., Claudio, G., Bittner, E.R., Knoester, J. and Scholes, G.D., *The Journal of Physical Chemistry B*, **2008**, 113, 656-667.

[141] Banerji, N., Cowan, S., Vauthey, E. and Heeger, A.J., *Journal of Physical Chemistry C*, **2011**, 115, 9726-9739.

[142] Westenhoff, S., Beenken, W.J.D., Friend, R.H., Greenham, N.C., Yartsev, A. and Sundström, V., *Physical Review Letters*, **2006**, 97, 166804.

[143] Jakubiak, R., Rothberg, L.J., Wan, W. and Hsieh, B.R., *Synthetic Metals*, **1999**, 101, 230-233.

[144] Samuel, I.D.W., Rumbles, G. and Collison, C.J., *Physical Review B*, **1995**, 52, R11573-R11576.

[145] Perrin, F., *Journal de Physique et le Radium*, **1934**, 5, 497-511.

[146] Koenig, S.H., *Biopolymers*, **1975**, 14, 2421-2423.

[147] Schmid, S.A., Yim, K.H., Chang, M.H., Zheng, Z., Huck, W.T.S., Friend, R.H., Kim, J.S. and Herz, L.M., *Physical Review B*, **2008**, 77, 115338.

[148] Nguyen, T.-Q., Wu, J., Doan, V., Schwartz, B.J. and Tolbert, S.H., *Science*, **2000**, 288, 652-656.

[149] Schwartz, B.J., Nguyen, T.-Q., Wu, J. and Tolbert, S.H., *Synthetic Metals*, **2001**, 116, 35-40.

[150] Gaab, K.M. and Bardeen, C.J., *The Journal of Physical Chemistry B*, **2004**, 108, 4619-4626.

[151] Chiu, M., Kee, T.W. and Huang, D.M., *Australian Journal of Chemistry*, **2012**, 65, 463-471.

[152] De Leener, C., Hennebicq, E., Sancho-Garcia, J.-C. and Beljonne, D., *The Journal of Physical Chemistry B*, **2009**, 113, 1311-1322.

[153] Kumar, P., Mehta, A., Mahurin, S.M., Dai, S., Dadmun, M.D., Sumpter, B.G. and Barnes, M.D., *Macromolecules*, **2004**, 37, 6132-6140.

[154] DuBay, K.H., Hall, M.L., Hughes, T.F., Wu, C., Reichman, D.R. and Friesner, R.A., *Journal of Chemical Theory and Computation*, **2012**, 8, 4556-4569.

[155] Meier, H., Stalmach, U. and Kolshorn, H., *Acta Polymerica*, **1997**, 48, 379-384.

[156] Klaerner, G. and Miller, R.D., *Macromolecules*, **1998**, 31, 2007-2009.

[157] Setayesh, S., Marsitzky, D. and Müllen, K., *Macromolecules*, **2000**, 33, 2016-2020.

[158] Gierschner, J., Cornil, J. and Egelhaaf, H.J., *Advanced Materials*, **2007**, 19, 173-191.

[159] Tilley, A.J., Danczak, S.M., Browne, C., Young, T., Tan, T., Ghiggino, K.P., Smith, T.A. and White, J., *The Journal of Organic Chemistry*, **2011**, 76, 3372-3380.

[160] Lewis, A.J., Ruseckas, A., Gaudin, O.P.M., Webster, G.R., Burn, P.L. and Samuel, I.D.W., *Organic Electronics*, **2006**, 7, 452-456.

[161] Bjorgaard, J.A. and Köse, M.E., *Journal of Applied Physics*, **2013**, 113, -.

[162] Tozer, O.R. and Barford, W., *The Journal of Physical Chemistry A*, **2012**, 116, 10310-10318.

[163] Minh Trung, D., Hirsch, L. and Wantz, G., *Advanced Materials*, **2011**, 23, 3597-3602.

[164] Lee, S.-H., Kim, D.-H., Kim, J.-H., Lee, G.-S. and Park, J.-G., *J. Phys. Chem. C*, **2009**, 113, 21915-21920.

[165] Lee, S.-H., Kim, J.-H., Shim, T.-H. and Park, J.-G., *Electron. Mater. Lett.*, **2009**, 5, 47-50.

[166] Sondergaard, R., Helgesen, M., Jorgensen, M. and Krebs, F.C., *Adv. Energy Mater.*, **2011**, 1, 68-71.

[167] Stapleton, A., Vaughan, B., Xue, B., Sesa, E., Burke, K., Zhou, X., Bryant, G., Werzer, O., Nelson, A., Kilcoyne, A.L.D., Thomsen, L., Wanless, E., Belcher, W. and Dastoor, P., *Solar Energy Materials and Solar Cells*, **2012**, 102, 114-124.

[168] Clarke, T.M., Ballantyne, A.M., Nelson, J., Bradley, D.D.C. and Durrant, J.R., *Advanced Functional Materials*, **2008**, 18, 4029-4035.

[169] Guo, J., Ohkita, H., Benten, H. and Ito, S., *Journal of the American Chemical Society*, **2010**, 132, 6154-6164.

[170] Honda, S., Yokoya, S., Ohkita, H., Benten, H. and Ito, S., *J. Phys. Chem. C*, **2011**, 115, 11306-11317.

[171] Howard, I.A., Mauer, R., Meister, M. and Laquai, F., *Journal of the American Chemical Society*, **2010**, 132, 14866-14876.

[172] Kirkpatrick, J., Keivanidis, P.E., Bruno, A., Ma, F., Haque, S.A., Yarstev, A., Sundstrom, V. and Nelson, J., *Journal of Physical Chemistry B*, **2011**, 115, 15174-15180.

[173] Ohkita, H., Cook, S., Astuti, Y., Duffy, W., Tierney, S., Zhang, W., Heeney, M., McCulloch, I., Nelson, J., Bradley, D.D.C. and Durrant, J.R., *Journal of the American Chemical Society*, **2008**, 130, 3030-3042.

[174] Singh, S., Pandit, B., Basel, T.P., Li, S., Laird, D. and Vardeny, Z.V., *Phys. Rev. B: Condens. Matter Mater. Phys.*, **2012**, 85, 205206/205201-205206/205207.

[175] Wong, C.T.O., Lo, S.S. and Huang, L., *The Journal of Physical Chemistry Letters*, **2012**, 3, 879-884.

[176] Zhang, W., Hu, R., Li, D., Huo, M.-M., Ai, X.-C. and Zhang, J.-P., *J. Phys. Chem. C*, **2012**, 116, 4298-4310.

[177] Guo, J., Ohkita, H., Benten, H. and Ito, S., *Journal of the American Chemical Society*, **2009**, 131, 16869-16880.

[178] Mihailetchi, V.D., Xie, H., de, B.B., Koster, L.J.A. and Blom, P.W.M., *Advanced Functional Materials*, **2006**, 16, 699-708.

[179] Scharsich, C., Lohwasser, R.H., Sommer, M., Asawapirom, U., Scherf, U., Thelakkat, M., Neher, D. and Koehler, A., *Journal of Polymer Science Part B: Polymer Physics*, **2012**, 50, 442-453.

[180] Spano, F.C., *Accounts of Chemical Research*, **2010**, 43, 429-439.

[181] Piris, J., Dykstra, T.E., Bakulin, A.A., van Loosdrecht, P.H.M., Knulst, W., Trinh, M.T., Schins, J.M. and Siebbeles, L.D.A., *J. Phys. Chem. C*, **2009**, 113, 14500-14506.

[182] Hwang, I.-W., Moses, D. and Heeger, A.J., *J. Phys. Chem. C*, **2008**, 112, 4350-4354.

[183] Nogueira, A.F., Montanari, I., Nelson, J., Durrant, J.R., Winder, C. and Sariciftci, N.S., *Journal of Physical Chemistry B*, **2003**, 107, 1567-1573.

[184] Nelson, J., *Phys. Rev. B*, **2003**, 67.

[185] Xie, Y., Li, Y., Xiao, L., Qiao, Q., Dhakal, R., Zhang, Z., Gong, Q., Galipeau, D. and Yan, X., *The Journal of Physical Chemistry C*, **2010**, 114, 14590-14600.

[186] Parkinson, P., Müller, C., Stingelin, N., Johnston, M.B. and Herz, L.M., *The Journal of Physical Chemistry Letters*, **2010**, 1, 2788-2792.

[187] Swinnen, A., Haeldermans, I., vande Ven, M., D'Haen, J., Vanhoyland, G., Aresu, S., D'Olieslaeger, M. and Manca, J., *Advanced Functional Materials*, **2006**, 16, 760-765.

[188] Prosa, T.J., Winokur, M.J., Moulton, J., Smith, P. and Heeger, A.J., *Macromolecules*, **1992**, 25, 4364-4372.

[189] Rispens, M.T., Meetsma, A., Rittberger, R., Brabec, C.J., Sariciftci, N.S. and Hummelen, J.C., *Chemical Communications*, **2003**, 2116-2118.

[190] Kaake, L.G., Barbara, P.F. and Zhu, X.Y., *The Journal of Physical Chemistry Letters*, **2010**, 1, 628-635.

[191] Chen, J.-T. and Hsu, C.-S., *Polymer Chemistry*, **2011**, 2, 2707-2722.

[192] Weickert, J., Dunbar, R.B., Hesse, H.C., Wiedemann, W. and Schmidt-Mende, L., *Advanced Materials*, **2011**, 23, 1810-1828.

[193] Yang, Y., Mielczarek, K., Zakhidov, A. and Hu, W. *Effects of nanostructure geometry on polymer chain alignment and device performance in nanoimprinted polymer solar cell*. 2013.

[194] Kim, J.S., Lee, J.H., Park, J.H., Shim, C., Sim, M. and Cho, K., *Advanced Functional Materials*, **2011**, 21, 480-486.

[195] Berson, S., De Bettignies, R., Bailly, S. and Guillerez, S., *Advanced Functional Materials*, **2007**, 17, 1377-1384.

[196] Sun, S., Salim, T., Wong, L.H., Foo, Y.L., Boey, F. and Lam, Y.M., *Journal of Materials Chemistry*, **2011**, 21, 377-386.

[197] Merlo, J.A. and Frisbie, C.D., *The Journal of Physical Chemistry B*, **2004**, 108, 19169-19179.

[198] Oosterbaan, W.D., Vrindts, V., Berson, S., Guillerez, S., Douheret, O., Ruttens, B., D'Haen, J., Adriaensens, P., Manca, J., Lutsen, L. and Vanderzande, D., *Journal of Materials Chemistry*, **2009**, 19, 5424-5435.

[199] Shimomura, T., Takahashi, T., Ichimura, Y., Nakagawa, S., Noguchi, K., Heike, S. and Hashizume, T., *Physical Review B*, **2011**, 83, 115314.

[200] Roehling, J.D., Arslan, I. and Moule, A.J., *Journal of Materials Chemistry*, **2012**, 22, 2498-2506.

[201] Baghgar, M., Labastide, J., Bokel, F., Dujovne, I., McKenna, A., Barnes, A.M., Pentzer, E., Emrick, T., Hayward, R. and Barnes, M.D., *The Journal of Physical Chemistry Letters*, **2012**, 3, 1674-1679.

[202] Niles, E.T., Roehling, J.D., Yamagata, H., Wise, A.J., Spano, F.C., Moulé, A.J. and Grey, J.K., *The Journal of Physical Chemistry Letters*, **2012**, 3, 259-263.

[203] Martin, T.P., Wise, A.J., Busby, E., Gao, J., Roehling, J.D., Ford, M.J., Larsen, D.S., Moulé, A.J. and Grey, J.K., *The Journal of Physical Chemistry B*, **2012**, 117, 4478-4487.

[204] Paquin, F., Latini, G., Sakowicz, M., Karsenti, P.-L., Wang, L., Beljonne, D., Stingelin, N. and Silva, C., *Physical Review Letters*, **2011**, 106, 197401.

[205] Labastide, J.A., Baghgar, M., McKenna, A. and Barnes, M.D., *The Journal of Physical Chemistry C*, **2012**, 116, 23803-23811.

[206] Schwarz, K.N., Kee, T.W. and Huang, D.M., *Nanoscale*, **2013**, 5, 2017-2027.

[207] Zhang, W., Zhao, N.-J., Huo, M.-M., Fu, L.-M., Ai, X.-C. and Zhang, J.-P., *Molecules*, **2012**, 17, 13923-13936.

[208] Schwarz, K.N., Kee, T.W. and Huang, D.M., *Nanoscale*, **2013**.

[209] Gadermaier, C., Cerullo, G., Manzoni, C., Scherf, U., List, E.J.W. and Lanzani, G., *Chemical Physics Letters*, **2004**, 384, 251-255.

[210] Clark, J., Nelson, T., Tretiak, S., Cirmi, G. and Lanzani, G., *Nat Phys*, **2012**, 8, 225-231.

[211] Cook, S., Liyuan, H., Furube, A. and Katoh, R., *The Journal of Physical Chemistry C*, **2010**, 114, 10962-10968.

[212] Shaw, P.E., Ruseckas, A. and Samuel, I.D.W., *Advanced Materials*, **2008**, 20, 3516-3520.

[213] Shaw, P.E., Lewis, A.J., Ruseckas, A. and Samuel, I.D.W. *Exciton annihilation and diffusion in semiconducting polymers*. 2006.

[214] Masri, Z., Ruseckas, A., Emelianova, E.V., Wang, L., Bansal, A.K., Matheson, A., Lemke, H.T., Nielsen, M.M., Nguyen, H., Coulembier, O., Dubois, P., Beljonne, D. and Samuel, I.D.W., *Advanced Energy Materials*, **2013**, 3, 1445-1453.

[215] Mikhnenko, O.V., Azimi, H., Scharber, M., Morana, M., Blom, P.W.M. and Loi, M.A., *Energy & Environmental Science*, **2012**, 5, 6960-6965.

[216] Lüer, L., Egelhaaf, H.J., Oelkrug, D., Cerullo, G., Lanzani, G., Huisman, B.H. and de Leeuw, D., *Organic Electronics*, **2004**, 5, 83-89.

[217] Zhao, Y., Sugunan, A., Rihtnesberg, D.B., Wang, Q., Toprak, M.S. and Muhammed, M., *physica status solidi (c)*, **2012**, 9, 1546-1550.

[218] Scharsich, C., Lohwasser, R.H., Sommer, M., Asawapirom, U., Scherf, U., Thelakkat, M., Neher, D. and Köhler, A., *Journal of Polymer Science Part B: Polymer Physics*, **2012**, 50, 442-453.

[219] Liu, J., Arif, M., Zou, J., Khondaker, S.I. and Zhai, L., *Macromolecules*, **2009**, 42, 9390-9393.

[220] Wang, H., Wang, H.-Y., Gao, B.-R., Wang, L., Yang, Z.-Y., Du, X.-B., Chen, Q.-D., Song, J.-F. and Sun, H.-B., *Nanoscale*, **2011**, 3, 2280-2285.

[221] Heiber, M.C. and Dhinojwala, A., *The Journal of Physical Chemistry C*, **2013**, 117, 21627-21634.

[222] Ozel, I.O., Ozel, T., Demir, H.V. and Tuncel, D., *Optics Express*, **2010**, 18, 670-684.